Finite Element-based Stress Intensity Factor Estimation for Fatigue Crack Growth Simulation and Stochastic Filtering-based Fatigue Crack Growth Prediction of Pipelines

by

Durlabh Bartaula

A thesis submitted in partial fulfillment of the requirements for the degree of

Master of Science

in

STRUCTURAL ENGINEERING

Department of Civil and Environmental Engineering

University of Alberta

© Durlabh Bartaula, 2022

ABSTRACT

Fatigue cracking is one of the major integrity threats to oil and gas pipelines. Having a reliable trajectory of fatigue crack growth once detected is very crucial for decision making regarding integrity threat management. In-line Inspection (ILI) tools, and other non-destructive methods are used to assess different damage levels, such as measuring fatigue crack sizes in pipelines. Furthermore, fracture mechanics-based models, such as linear elastic fracture mechanics (LEFM) based Paris' law, is used for prediction of future crack growth trajectory for fatigue crack integrity management in oil and gas pipelines.

Neither fracture mechanics-based models nor crack measurements can be solely used to make a perfect fatigue crack growth (FCG) related integrity threats management decisions. However, the information contained in both sources can be fused to make better FCG predictions to support integrity management decisions. As such stochastic filtering specifically Particle Filter (PF), an iterative Bayesian approach, can be used for extraction of information about unknown model parameters like the material properties and crack sizes at certain time of interest by using data measured up to and including that point of time. Afterwards, Paris' law can be used to predict future trajectory based on the updated information from the PF-based estimation process. As such, a methodology to couple the Particle Filter and Paris' law, stochastic filtering-based FCG prediction, is developed in this study as a tool for pipelines with a fatigue crack.

In the Paris law, the range of Stress Intensity Factor (SIF), the other important parameter besides the material fatigue crack resistance properties, are usually estimated using industry standard codes such as API 579 or BS 7910. In this study, the fatigue crack driving parameter SIF calculation using extended finite element method (XFEM), as well as conventional finite element method

(FEM) implemented in Abaqus®, was dealt in detail along with various factors, like mesh size, mesh/element type, number of contour request and enrichment radius at the crack tip/front. The SIF estimation results were compared with the aforementioned industry models for cracked pipelines and analytical solutions for compact tension (CT) specimens. This aims to explore the capability of XFEM for SIF estimation in cracked pipelines, and also to assess the accuracy of the industry models (e.g., API 579). An indirect method of estimating fatigue crack growth (FCG) trajectory incorporating the SIF estimated using XFEM is then demonstrated for both a CT specimen and pipeline section tested in the literature. FCG trajectory, which is very sensitive to the fatigue parameters and the SIF, was successfully estimated reasonably well.

Instead of using the API 579 model, directly for stochastic filtering-based FCG prediction process, a single surrogate model using Gaussian Process Regression (GPR) was developed and used. The GPR model, trained using validated SIF data points based on the various numerical and analytical models, was built for quick, reliable and computationally less expensive SIF estimation.

To this end, a PF-based fatigue crack growth prediction methodology for pipelines was developed to leverage measurement data and known physics-based model, e.g., Paris law. This methodology was implemented as a python tool, to (1) jointly estimate fatigue model parameters and crack sizes, and (2) predict future trajectory of the fatigue crack growth in pipelines. This tool was applied to case studies using synthetic data of noisy crack size measurements in a pipeline for the purpose of demonstration.

ACKNOWLEDGEMENTS

A very special thanks goes to Dr. Yong Li, for being a great supervisor and a friend throughout my graduate school journey. His thorough guidance, patience, and confidence motivated me to reach this stage. I highly appreciate and thank Dr. Smitha Koduru (formerly employee of C-FER) for providing me an opportunity to work in an industry-based professional environment in C-FER Technologies through the Mitacs Accelerate Program.

I would like to take this opportunity to thank my parents Mr. Bhagwan Bartaula and Mrs. Sulochana Bhattarai, my brother Mr. Sulabh Bartaula, sister-in-law Mrs. Pratibha Kadariya. My entire family and friends have been a great support for me.

TABLE OF CONTENTS

LIST OF FIGURES

LIST OF TABLES

CHAPTER 1: INTRODUCTION

1.1 Background

Pipelines are known to be the safest and efficient medium of transporting oil and gas from development areas to consumers. About 97% of the Canadian natural gas and crude oil production is transported by transmission pipelines as per Canadian Energy Pipeline Association (CEPA) [1] and similar statistics can be found for many other countries. The high percentage clearly indicates the vitality of oil and gas pipes to both the consumers and pipeline operators.

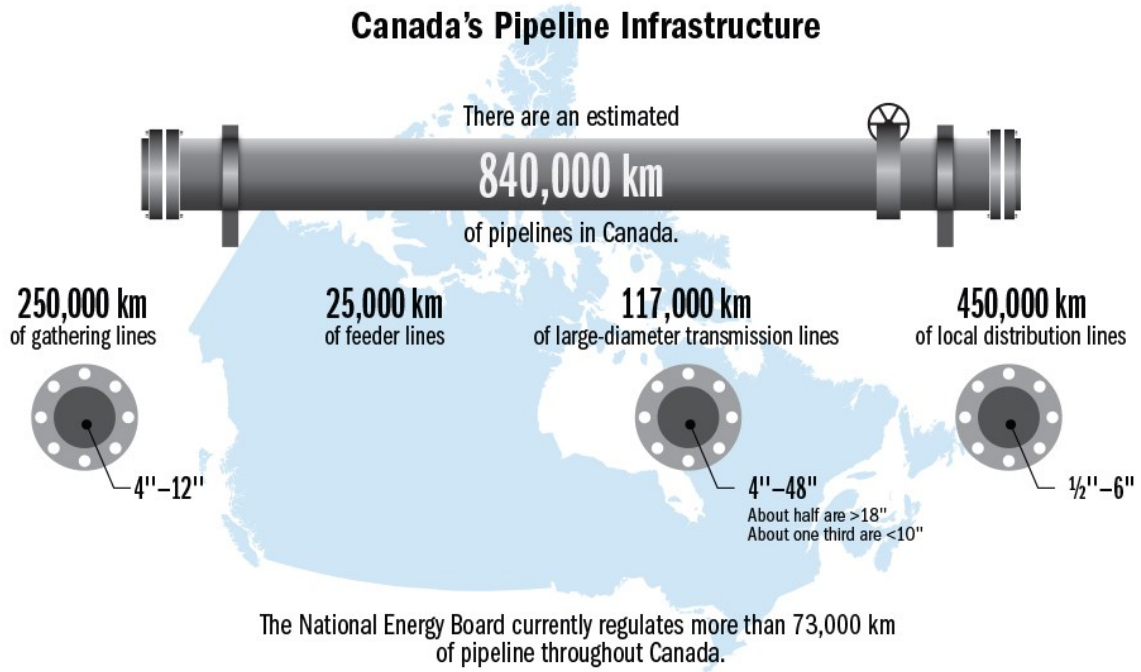

Figure 1-1: Canada's Pipeline Infrastructure [2]

As shown in Figure 1-1 the Canadian pipeline infrastructure comprises four main pipeline system viz. gathering lines (4"- 12"), feeder lines, transmission lines (4"-48"), and local distribution lines (1/2"- 6") [2]. The first Canadian pipeline was a 25 kilometer long cast-iron natural gas pipe built in 1853 and with discovery of abundant source of crude oil and natural gas the pipeline network expanded in the 1950s [3]. After years of service, pipelines can suffer from different types of defects, which poses different kinds of integrity threats like corrosion, fatigue cracking, stress

corrosion cracking (SCC), mechanical damages (e.g., dent) and others as shown in Figure 1-2. Presence of crack like defects anywhere in the pipeline body, welds, dent, and corrosion site makes the pipeline vulnerable to different kinds of threats. Pipeline operating situations like line start–stop, pigging, product injection and unexpected shut-down can cause pressure fluctuations [4]. These factors together make fatigue crack grow in oil and gas pipelines.

(a) (b)

(c) (d)

Figure 1-2: Photos of ruptured pipelines due to different type of defects: (a) fatigue cracking [5], (b) stress corrosion cracking [6], (c) mechanical damage (dent) [7], and (d) other (penetration) [8]

1.2 Problem Statement and Motivation

A defect-free pipeline usually can have fatigue life much longer than the service life of most oil and gas pipelines [9]. However, pipelines are very likely to have anomalies and consequently have significantly reduced fatigue life causing integrity threat. Presence of defects in pipelines is inevitable resulting in cracks that can eventually propagate and cause sudden failure. Once a crack is detected in a pipeline by the operator via performing inline inspection (ILI) or any other non-destructive testing, taking timely maintenance to control the crack growth or subsequent inspection scheduling can be beneficial. As such, tracking and reliably predicting the crack growth as a function of the operation time or load cycles can provide support to assist decision-making for integrity management. If the model that describes the fatigue life (e.g., S-N curve) is accurate, and no uncertainty exists in the stress cycles, fatigue life prediction is deterministic. Similarly, if an accurate facture mechanics-based model that can describe the damage evolution as a function of time exists and the initial crack measurement is accurate or free of noise, fatigue crack growth can be predicted deterministically. However, in practice, neither of these two are true. The fatigue life and the crack growth prediction is challenging due to the imperfect model or unknown model parameters and uncertainties involved in the load history. Furthermore, crack size measurements can be noisy due to the noisy inheritance of the in-line inspection (ILI) tool used.

Though neither of fracture mechanics-based models nor crack measurements can be solely used to perfectly predict fatigue crack propagation, the information contained in both sources can be fused to better predict the future. One of many approaches to deal with such problems is to use Bayesian methods. In a Bayesian method, a prior distribution of the noisy crack size is combined with the likelihood of the crack size data collected using ILI tools to build a posterior probability distribution. For example, stochastic filtering, an iterative Bayesian approach, can be used for extracting information about unknown model parameters and crack states at certain time of interest by using data measured up to and including that point of time. Essentially, it provides a ‘best estimate’ for the true value of the state for a system or process based on noisy observations available, and the updated model can be further used for better predictions. Fatigue crack growth propagation being a stochastic process is influenced by varieties of uncertainty like material properties, load, and environmental factors. Therefore, accurate estimation of current state of crack

size and fatigue model parameters, e.g., for the Paris' law as considered in this study as the fatigue crack growth model, is very crucial for reliable prediction of fatigue crack growth trajectory.

1.3 Objectives

The two main objectives of this study are as follows:

i. To develop a fatigue crack growth (FCG) simulation method in pipelines using extended finite element method (XFEM) when crack size measurement data is absent.
ii. To develop a FCG trajectory prediction tool when a sequence of crack size measurement data is available till the current state.

1.4 Methodology

The extended finite element method (XFEM) implemented in Abaqus® is used to explore the fatigue crack growth simulation, with special focus on the calculation of fatigue crack driving parameters, i.e., Stress Intensity Factor (SIF). The numerical simulation results for SIF are used to verify the well-known model in API 579, i.e., the lookup table for SIF calculation. Surrogate models for efficient calculation or interpolation of SIF are developed using Gaussian process regression. To the end, a tool based on stochastic filtering is developed using crack size measurement data and a fatigue crack growth model for joint estimation of crack size and fatigue crack growth model parameters, as well as future crack growth trajectory prediction. To demonstrate the application of the tool developed, a few case studies using synthetic data considering different measurement noise levels are presented.

To sum up, in order to achieve the aforementioned objectives the following research tasks are followed

1. Literature review on relevant works on fatigue crack growth quantification on the body of steel pipelines.
2. Investigation of numerical methods for fatigue crack growth prediction and calculation of fatigue crack driving parameters i.e., Stress Intensity Factor (SIF).

3. Verification of analytical model for calculation of SIF prescribed in API 579 [10] against Finite Element Methods (FEM) and relatively new eXtended Finite Element Methods (XFEM).
4. Development of surrogate model to mimic thus validated analytical model for estimation of SIF.
5. Development of stochastic filter-based tool for pipeline fatigue crack size estimation by integrating crack size data collected from ILI with fatigue crack growth prediction model, i.e. Paris Law.
6. Demonstration of the use of stochastic filter-based tool for joint estimation of model parameters and current fatigue crack size, and use the updated information (i.e., current crack size and updated model parameters) for prediction of future crack growth trajectory along with the reliability quantification of prediction.

1.5 Organization of the Thesis

This thesis contains six chapters as follows:

Chapter 1 introduces fatigue crack problems in oil and gas pipelines subjected to fluctuating internal pressure cyclic load, leading to the need of reliable quantification of fatigue crack growth trajectory. Followed by the objectives of this study and the methodology to achieve the proposed goals, this chapter ends with the picture of overall flow of the thesis through different chapters.

Chapter 2 comprises of a summary of relevant studies or research investigations carried out with regards to the fatigue related issues in steel pipelines.

Chapter 3 explores the fatigue crack growth simulation using existing techniques built in Abaqus®, with special emphasis on the estimation of fatigue driving parameters. It also presents a detailed discussion on various analytical models currently practised in the pipeline industry, like in API 579 and BS 7910 for estimating SIF used in fatigue crack growth analysis. The models are then compared with two different numerical methods viz. Finite Element Method (FEM) and eXtended Finite Element Method (XFEM).

Chapter 4 discusses the use of surrogate modeling technique like Gaussian Process Regression (GPR) for reliable, fast and computationally less expensive estimation of the fatigue driving parameter, SIF.

Chapter 5 introduces stochastic filtering methods for the joint estimation of fatigue crack growth model parameters and current fatigue crack sizes, when fatigue crack size measurement data is available. Furthermore, probabilistic prediction of future fatigue crack growth trajectory based on the estimated current crack size and model parameters is discussed in detail.

Chapter 6 summarizes the entire work with conclusion of the research followed by recommendation for future works.

CHAPTER 2: LITERATURE REVIEW

This chapter presents a literature review, aiming to provide the relevant research background in various aspects related to the thesis research. Firstly, different types of pipeline integrity threats are introduced and works related to management of the threats are discussed. Fatigue cracking is one of the major integrity threats to the pipelines. Various approaches for fatigue design of pipelines and fatigue crack integrity threat management once the crack is detected are discussed. Fracture mechanics-based method for fatigue crack growth assessment is widely used in pipeline industry; relevant details and works are discussed. Different methods for estimation of fatigue crack driving parameters like analytical models, and numerical models are discussed. Followed by a review on alternate approach, using surrogate models, for reliable estimation of fatigue crack driving parameters, a concise review on surrogate models is also presented. Finally, a brief review on using Bayesian approach for probabilistic estimation of fatigue crack growth model parameters and/or crack sizes to assist monitoring the fatigue crack growth in pipelines is presented.

2.1 Introduction to Pipeline Integrity Threats and Management

Pipelines are susceptible to various integrity threats due to operating condition, environment, material property changes, and third-party influence to mention a few. Pipeline integrity management remains top priority of a pipeline operator because of the factors like financial, social responsibilities, and government regulations amongst many others. Pipeline integrity threats are factors that alters the operation of pipeline resulting in occurrence of any kind of incidents. ASME-B31.8S-2018 [11] classifies pipeline integrity threats into three main categories viz. (a) time dependent, (b) resident, and (c) random or time independent. Particularly, if the operational mode in which the pipelines are subjected to significant pressure cycles, pressure differential, and rates of change of pressure fluctuations, fatigue is recommended to be considered as integrity threats.

2.1.1 Time Dependent Integrity Threats

Time dependent integrity threats are the kind of hazards or threats that grow with time and requires periodic inspection to monitor their growth. They include cracking due to fatigue or stress corrosion (SCC), and metal loss due to environmentally assisted corrosion or erosion [12].

2.1.1.1 Cracking

Cracking can be considered as one of the major integrity threats and can develop in pipeline at any stage- during manufacturing, fabrication, installation and throughout operational life [13].

Fatigue cracking can be considered as local damage accumulation due to presence of microstructural voids in the materials causing stress raisers. It will be visible when the accumulated damage is large enough. Defect-free pipelines can typically survive the threat caused by fatigue well beyond its expected life. Kiefner et al. (2004) [14] summarized that the presence of large, longitudinally oriented defects, aggressiveness of the pressure cycles at the defect site and the rate of crack growth inherent in the material in its particular environment as the three main factors influencing the fatigue in a pipeline. Many incidents in pipelines related to fatigue have been reported in the past; two incidents related to fatigue crack within shallow dents occurred in 2009 as per a report from National Energy Board, Canada [15]. Presence of pre-exiting surface or embedded defects in offshore pipelines, which are under fluctuating loadings due to waves, currents and ground motions, are very susceptible to fatigue failure [16]. Fatigue damage accumulation has been a greater concern for liquid pipelines than gas pipelines due to aggressive pressure fluctuations [17]. Semiga et al. (2016) presented a method of defining which gas pipeline segments can reasonably be considered to be at risk of fatigue damage. Various limit curves were defined based on the wall thickness, grade, initial defect size, pressure cycling severity as factors beyond which the pipelines would be at risk of fatigue damage [18]. Presence of defects such as wrinkle, which otherwise may not pose an immediate threat, can lead to fatigue crack initiation, propagation and rupture due to pressure fluctuation and stress concentration [19].

Stress corrosion cracking (SCC) refers to service failure in engineering materials occurring due to slow, environmental induced crack propagation [20]. The environment around pipe i.e., high pH or near neutral pH, coating disband, pipe surface temperature and the stresses caused due to operating pressure and various other factors, are the main cause behind SCC [21]. High pH SCC and near neutral pH SCC were first identified in 1960s and 1980s respectively [21]. Both high pH and near neutral SCC are characterized by colonies of many longitudinal surface cracks in the body of the pipeline that link up to form long shallow flaws. The main difference being inter-granular fracture mode in the high pH SCC and trans-granular in near neutral- pH SCC [22]. Also

high pH SCC is associated with very less evidence of corrosion of the crack walls or the outer pipe surface; on the contrary near neutral pH SCC is often accompanied by corrosion of the crack walls and the outer pipe surface [22]. Near neutral pH SCC, a major integrity threat and cause for several pipeline failures, was first identified in a pipeline of Canadian pipeline operator TransCanada Pipelines Ltd., subsequently by many other pipeline operators in the U.S.A., Asia, Australia, Europe [23].

2.1.1.2 Metal Loss

Metal loss are caused due to erosion and corrosion, which poses a major integrity threat to pipelines. Corrosion is the most common form of defects and affected by surrounding environment. Erosion defects can also be caused when sand particles contained in oil and gas come in contact with pipe walls [24]. Ossai et al. (2012) [25] presented a review on effects of corrosion on pipelines, risk assessment methodologies and mitigation framework. Furthermore, authors demonstrated the use of previous field data to predict the effects of corrosion in the future [25]. Equipment used in pipeline industry is a major victim of erosion; thus some numerical erosion models were based on experimental and response from existing sub-models [26]. Note that the combination of erosion and corrosion (E-C) causes excessive material loss compared to that due to individual effects [27].

2.1.2 Time Independent Integrity Threats

Time independent integrity threats are random in nature and can occur at anytime and can be controlled to some extent by surveys, communication and protective measures [24].

2.1.2.1 Mechanical Damage

Mechanical damage is defined as localized damage to the pipe resulting from contact. Dents, gouges, and combined dents-gouges are very common types of mechanical damage that can be observed in pipelines. Dents are the depressions in the pipe that causes change in the curvature and gouges are the surface damage in pipelines caused by contact with foreign objects [28]. For example, dents are caused due to impact from indenting objects like rock, excavator, etc., while gouges can be formed due to excavator tooth. Different causes of mechanical damage have varied severity: rock induced damage typically results in delayed failure whereas, those caused from

equipment are more likely to fail immediately [29]. Existing BG/EPRG model (old) and new Dent-Gouge models for assessing dents containing gouges were compared in [30]. The BG/EPRG model is a fracture mechanics based model for dent gouge assessment which is based on the relation between fracture toughness and plasticity of the pipe material. Furthermore, the new model was based on BG/EPRG model but presented using a failure assessment diagram (FAD) and takes effect of the micro-cracking and residual stress occurring around the gouge [30]. That study concluded that the old model gave best predictions of full scale test data and new model was more conservative for failure frequency estimation because of the minimal development in model research compared to inspection technologies [30] . Providing extra cover over has been reported to lower the chances of damage from digging [31]. Wang et al. (2014) [32] presented results on an enhanced approach for identification and characterization of top side dents based on unique criterions like geometry, strain and magnetic flux leakage (MFL) tool signal, whose effectiveness was verified with the field examinations.

2.1.2.2 Others

Damage caused due to third party activities, like drilling, piling, and ploughing, manufacturing defects, equipment failure can be considered as the other sources of time independent integrity threats. There are different technologies to assist the detection of such damage. Fiber optics technology is suitable for early detection of threats and acoustic sensing technology for detection, location, and classification of impact and leaks as reported in [33]. El-Hussein et al. (2015) [34] demonstrated the potential of using low frequency guided wave based on finite element and ball bearing drop field test for monitoring damage caused due to vandalism.

2.2 Approaches to Tackle Fatigue Threat for Pipeline Design and Integrity Management

Fatigue life of a component comprises of three distinct phases: crack initiation, stable crack propagation, and unstable crack propagation or fracture. The crack initiation phase makes up for majority of the fatigue life. This happens at the microstructural level and may not be visible. The stable crack growth phase is visible and more of concerns to the pipeline operators as it can eventually grow to a critical size and cause sudden fracture failure. It is at this stable crack growth phase where quantification and mitigation of the threat plays a vital role in the overall fatigue crack

integrity threat management of pipelines. Figure 2-1 shows a typical laboratory specimen subjected to fatigue testing and shows all three phases of the fatigue damage.

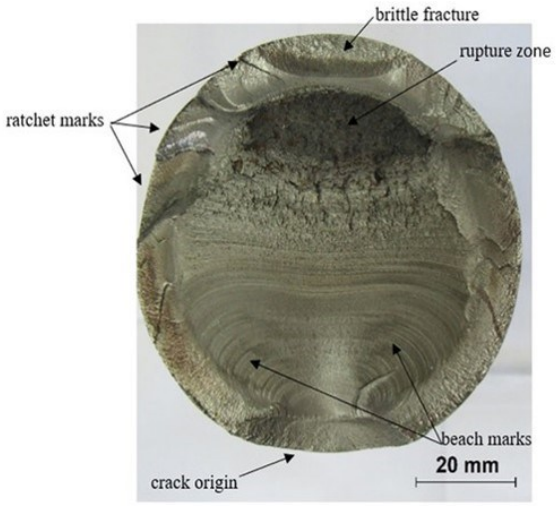

Figure 2-1: Laboratory specimen used for fatigue testing showing fatigue crack initiation, propagation and fracture [35]

2.2.1 Fatigue Design of Pipelines

Fatigue data of a material has been presented by S-N plots ever since Wohler's work on railroad axles subjected to rotating bending stress [36]. There are different design methodologies based on stress life i.e. S-N plot method, strain life i.e. ϵ-N plot method, fracture mechanics based or damage tolerant based methods [36]. The S-N plot method is used extensively and recommended by many standards like DNV RP-C203 [37] for fatigue design of steel oil and gas pipelines. For a test specimen made up of a specific material, the number of loading cycles (N) required to fracture it at a given stress range (S) is presented in the form of S-N plots, see a typical S-N plot as shown in Figure 2-2. The stress range is the difference between maximum and minimum stress in the specimen.

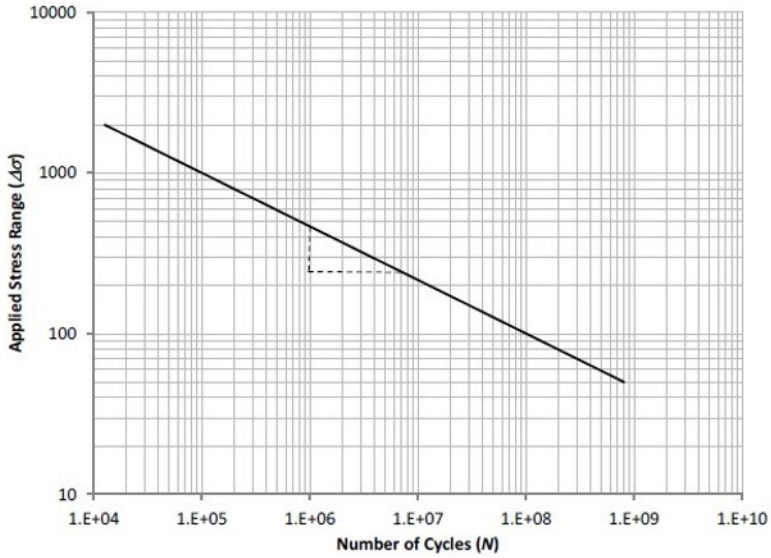

Figure 2-2: Typical S-N plot [9]

Eq. (2–1) can be used to estimate the fatigue life (N) at the applied stress range of a pipeline using S-N curve.

$$N = \frac{I}{\Delta\sigma^{s}} \tag{2–1}$$

where, $\Delta\sigma$ is the applied stress range, I and s are parameters describing the intercept and slope of the S-N curve respectively.

Semiga et al. (2016) [9] published a work entitled "Fatigue Considerations for Natural Gas Transmission Pipelines" and presented an example on estimating fatigue lives of three different pipelines with no defects. The three pipelines were assumed to be made up of X42, X52 and X80 grades, with the same diameter and wall thickness of 609.6 mm and 5.08 mm respectively as well as the same maximum allowable operating pressure (MAOP) at 72% of specified minimum yield stress (SMYS). Based on the values of I and s from DNV RP-C203 [37], the fatigue lives of the pipe body for three different grades of pipelines were estimated to be 409335, 173835 and 30979 cycles at MAOP. These values are much higher than the service life of the most gas pipelines.

Kanuf et al. (2007) [38] presented a review and a comparative study on different codes of practice for fatigue life assessment of pipes. The different standards compared were Germen code DIN

2413, English code IGE/TD/1/4, European code EN 13480, IIW, Eurocode 3, DNV RP-C203. The S-N plots from each code were compared for seamless, electric resistance welded (ERW) and submerged arc welding (SAW) pipelines. The authors emphasized the reliability of the S-N plots from DIN 2413 as these were obtained from a large number of tests of pipes representing a wide variety of dimensions, steel grades, production process and internal pressure fatigue.

Coffin et al. (1955) [39] established that plastic strain life data (ϵ-N plots) could be utilized for fatigue life prediction similar to S-N plots [36]. Gholami et al. (2020) [32] performed a strain-based fatigue life analysis of pipeline with the external defect under cyclic internal pressure. The fatigue life calculation model used there in was from Smith et al. (1970) [40] which was also based on the ϵ-N method.

The fracture mechanics-based fatigue design methodology is widely used for fatigue crack integrity threat management as it allows quantification of crack size with the loading cycles and is discussed in detail in the next section.

2.2.2 Fatigue Crack Integrity Threat Management in Pipelines

Fatigue crack integrity threat management starts with the proper identification of the cracks. Pipeline operators use different kinds of in-line inspection (ILI) tools depending upon the objective of the run. It could be for crack, metal loss, and mechanical damage detection. For instance, ILI tools based on magnetic flux leakages (MFL) are mainly used for metal loss inspection, while ultrasonic tools (UT) and electromagnetic acoustic transducers (EMAT) are used for different types of corrosion and crack detection. Each tool have their own advantages and disadvantages; a detailed discussion on this can be found in [24].

Once a crack is detected, quantifying the crack size with time can provide valuable insight in any kind of crack related integrity threat management. Paris' law introduced in [41] is one of such equations that quantifies the crack growth rate in the stable crack growth phase of fatigue life and given by Eq. (2–2):

$$\frac{da}{dN} = C(\Delta K)^m \tag{2–2}$$

where, da / dN is the rate of fatigue crack growth per loading cycle; C and m are fatigue properties of material; ΔK is the range of SIF when a structure is stressed from the minimum to the maximum load.

Paris' law is widely used in pipeline industry to quantify the fatigue cracking size with the loading cycles. Performance of Paris' law to accurately represent fatigue crack growth phenomenon depends on the factors like SIF, C, m, and load. API 579 [10] and BS 7910 [42] provides analytical solutions for estimation of SIF for various crack geometries and values of C and m. Jaske et al. (2006) [43] demonstrated that the use of fracture mechanics-based approach for estimating fatigue crack growth in pipelines based on Paris' law and recommend to include the effects of stress ratio as it could lead to excessively non-conservative predictions of fatigue life. Silva et al. (2011) [44] estimated the fatigue life of a pipeline using Paris' law, together with the analytical solution for estimation of SIF proposed using pipeline section subjected to cyclic indenting load, and C and m values estimated from the data obtained from fatigue tests on CT specimens. Tiku et al. (2020) [45] presented values of fatigue properties from a large set of full scale tests on different grade pipes and concluded that these values of fatigue properties combined with API 579 model for SIF estimation to be a less conservative and better predictor of the fatigue crack growth. There are many efforts being made to quantify the fatigue crack growth and fracture mechanics-based fatigue driving parameters such as SIF. In the next section, relevant but brief background on fracture mechanics is presented.

2.2.2.1 Fracture Mechanics Based Approach

Fracture mechanics approach for structural design adds crack size and measure of the fracture toughness for a material [36]. Fracture toughness measures the ability of a material to resist crack formation and propagation. Commonly used fracture toughness parameters are strain energy release rate (G), stress intensity factor (K), J-Integral, crack tip opening displacement (CTOD) or indirect parameters measured by the Charpy V-notch (CVN) impact test or other tests. Fracture

mechanics-based approach can be broadly classified into two categories: Linear Elastic Fracture Mechanics (LEFM) and Elastic-Plastic Fracture Mechanics (EPFM).

(1) Linear Elastic Fracture Mechanics (LEFM)

Linear elastic fracture mechanics (LEFM) is the domain of fracture mechanics with the assumption that the crack contained in a part is a flat surface in a linear elastic stress field and the energy released during this rapid crack propagation is a basic material property [36]. The strain energy released upon crack extension is the driving force for fracture in cracked material under linear elastic conditions. This loss of elastic potential energy with the crack extension of unit area is the strain energy release rate (G) [36].

The stress intensity factor (SIF) is a linear elastic fracture mechanics-based parameter that completely defines the crack tip condition. The critical value of SIF is called the fracture toughness. It is a single toughness parameter that can describe the stress and strain field in the vicinity of the crack tip and has a general form as shown in Eq. (2–3) [46]:

$$K_{(I,II,III)} = Y\sigma\sqrt{\pi a} \tag{2–3}$$

where, Y is a dimensionless constant function depending on the geometry of the structure and mode of loading as shown in Figure 2-3, σ is the characteristic stress (e.g., characteristics stress for a CT specimen is the remotely applied tensile load), and a is the characteristic crack dimension. The subscripts represent the value of K in each loading mode, viz. mode I (opening), mode II (in-plane shear mode) and mode III (out of plane shear mode).

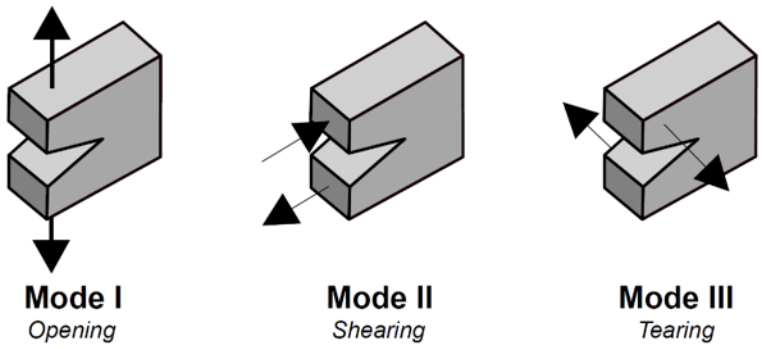

Figure 2-3: Fracture modes [47]

The strain energy release rate (G) and stress intensity factor are related as shown in Eq. (2–4):

$$G = \frac{K^2}{E'} \tag{2–4}$$

where, $E'=E$ for plane stress and $E' = E/(1-\nu^2)$ for plane strain conditions. E is the Young's modulus of elasticity and ν is the Poisson's ratio.

(2) Elastic-Plastic Fracture Mechanics

Elastic plastic fracture mechanics (EPFM) covers the high toughness structural materials undergoing large plastic deformation before fracture. *J*-Integral, crack tip opening displacement (CTOD) and R-Curve methods are some of the EPFM based parameters for crack analysis [36].

J-Integral is the change in potential energy of the body with crack extension. It is a contour integral taken around the crack tip which results in energy release rate as given in Eq. (2–5):

$$J = \oint \left[w dy - T\left(\frac{\partial u}{\partial x}\right) ds \right] \tag{2–5}$$

where, w is the strain energy per unit volume; T is the traction vector along the contour as shown in Figure 2-4; u is the displacement vector; ds is the incremental length along the contour.

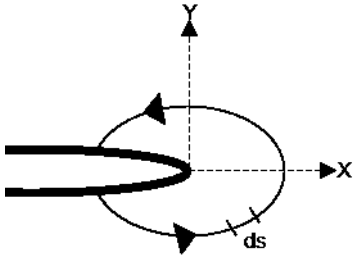

Figure 2-4: Arbitrary contour around a crack tip

The total magnitude of J-Integral consists of elastic and fully plastic part. For linear elastic and non-linear elastic materials in 2D plane, J-integral and G are equivalent. Therefore, J-Integral is related to the SIF as $J = K^2 / E'$; where $E' = E$ (Young's modulus of elasticity) for plane stress condition and $E' = E/(1-\upsilon^2)$ for plane strain condition and υ is the Poisson's ratio.

2.2.2.2 Numerical Methods for Various Types of Crack Growth Modeling

In order to quantify the damage levels numerical models can provide a very fast and inexpensive alternative over experimental approach to understand damage process like crack growth. The concept of fracture mechanics discussed in the previous section is the fundamentals for numerical modeling of the crack analysis. In this section, various works and further concepts related to numerical modeling of various types of crack growth in pipelines are discussed in detail.

(1) Quasi-Static Crack Growth Modeling

When the loading condition is slow enough where equilibrium assumption can be made at every loading step such phenomenon can be termed as quasi-static condition. For instance, in numerical modeling of burst pressure testing of pipelines the load is applied in small increments to provide static loading condition at each step whilst crack growth, this can be a quasi-static condition. Cohesive zone model (CZM) is a very popular method of numerical modeling of crack growth [48]. In CZM it is assumed that a local fracture occurs in the zone where stress has reached its limiting value causing stress to fall to zero at some displacement afterwards [49]. Traction separation law (TSL) is a constitutive relation that defines the CZM. TSL basically defines the

relation between cohesive traction acting on the crack surfaces to resist crack propagation and the corresponding separations of surfaces across an extended crack tip [48]. Selection of TSL depends on the material type either brittle or ductile. Figure 2-5 (a) shows a typical TSL curve for a brittle material and the area under the TSL curve is the critical strain energy release rate (G_c) [50]. Figure 2-5 (b) shows a typical stress-strain response curve for a ductile material with damage properties. Hillerborg et al. (1976) used CZM with brittle TSL for concrete fracture modeling using FEM [51] and this work was first of its kind. Wells et al. (2001) used CZM to model fracture in quasi-brittle material using FEM with unstructured mesh that allowed introduction of displacement jumps based on concept of partition of unity i.e. XFEM [52].

CZM is widely used for crack propagation analysis in pipelines. Shim et al. (2011) demonstrated the use of CZM to simulate ductile crack growth behavior of a through-wall cracked pipe, where the values of bending moment, *J*-Integral compared well with the experimental results [53]. Chanda et al. (2015) used CZM based FEM model to study the effects of temperature on fracture behavior of pipeline steel. Furthermore, based on a temperature dependent CZM parameters i.e. maximum traction and fracture energy for a pipeline steel, dynamic fracture was simulated in [54]. Wang et al. (2016) developed a method to estimate parameters required for CZM: maximum traction and cohesive energy based on stress-strain curve of the material. The predicted dynamic fracture behavior modeled using FEM was reported to have good agreement with previous works for X70 and X80 grade pipeline steel [55].

Extended Finite Element method (XFEM), first introduced by Belytschko et al. (1999) [56], has also been gaining popularity for engineering problems with discontinuity such as cracked pipelines. In XFEM cracks can be modeled independent of the actual structure which provides flexibility of no re-meshing or minimal re-meshing. XFEM model can alleviate the need of focused meshing and minimal re-meshing is required. Comprehensive studies have been performed at the University of Alberta using full scale pipe test and laboratory specimens to calibrate different damage initiation criterion like maximum principal stress, maximum principal strain. Agbo et al. (2019) [57] used XFEM to evaluate tensile strain capacity (TSC) after calibrating damage parameters based on experimental results and concluded that with appropriate damage parameters XFEM can reasonably reproduce full-scale experimental tests and can be used for parametric study. Lin et al. (2017) [58] calibrated fracture criterion to model crack propagation in XFEM

models using their previous experimental study on steel pipes with circumferential cracks subjected to eccentric tensile load on pressurized pipeline specimen. Lin et al. (2020) reported validated damage parameters based on maximum principal stress and fracture energy [48]. Okodi et al. (2020) used maximum principal strain and fracture energy as damage parameters to estimate burst pressure of pipeline with satisfactory results compared to the experimental and highlighted need of more full scale burst test for better calibration of the damage parameters [59]. XFEM has been successfully validated and used as a promising tool for quasi-static crack growth modeling, focusing more on the global structural response quantities (e.g., burst pressure) rather than local ones (e.g., SIF, *J*-integral).

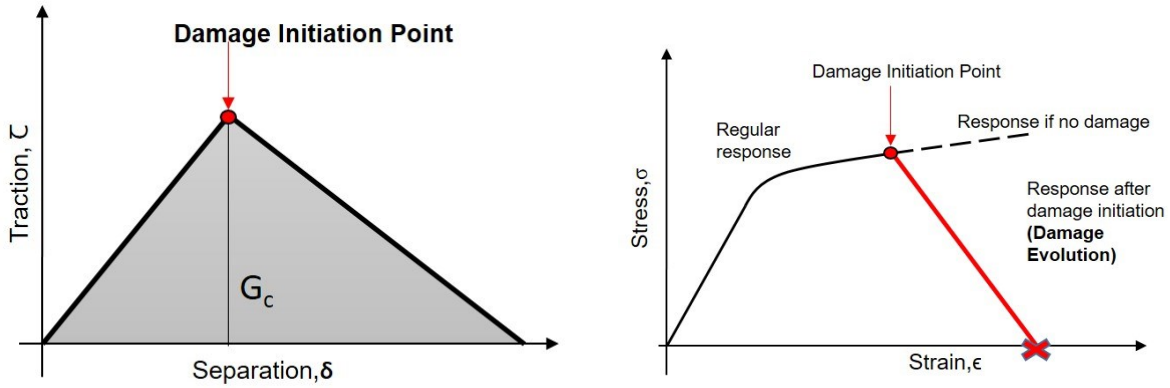

(a) (b)

Figure 2-5: (a) Typical traction separation law for brittle material, and (b) typical stress-strain curve for material with specified damage properties

(2) Fatigue Crack Growth Modeling

Numerical modeling of fatigue phenomenon, which involves a large number of load repetitions, can be prohibitively computationally expensive. Direct cyclic approach for fatigue damage modeling is based on the assumption that after a number of repetitive cycles, the response of elastic-plastic structures may lead to a stabilized state in which stress-strain relationship in each successive cycle is the same as in the previous one. Direct cyclic algorithm is implemented in Abaqus® which uses a modified Newton method in conjunction with a Fourier representation of the solution and the residual vector to obtain the stabilized cyclic response directly [60].

In Abaqus® only low cycle fatigue (LCF) analysis can be performed with XFEM. Low cycle fatigue (LCF) is associated with higher stress levels producing elastic and plastic deformation in the structure and fatigue life is usually less than 10000 cycles. Whereas, high cycle fatigue (HCF) are associated with relatively lower stress level producing elastic deformation in the structure and having fatigue life higher than 10000 cycles [61]. Selection of either LCF or HCF analysis depends on expected level of deformation in the component either elastic or elasto-plastic. LCF analysis implemented in Abaqus® XFEM relates fatigue crack growth rate to the fracture energy release rate (or strain energy release rate) at the crack tips in the enriched elements as shown in Figure 2-6. The fatigue crack initiates when the energy release rate is above some threshold values and governed by Eq. (2–6):

$$\frac{N}{c_1 \Delta G^{c_2}} \geq 1.0 \tag{2–6}$$

where, N is the number of cycles, c_1 and c_2 are material properties governing the crack initiation and ΔG is the energy release rate at the corresponding load cycle.

The fatigue crack growth is governed by Paris law in energy terms given by Eq. (2–7):

$$\frac{da}{dN} = c_3 \Delta G^{c_4} \tag{2–7}$$

where, da / dN is the rate of fatigue crack growth per loading cycle; c_3 and c_4 are fatigue properties of material; ΔG is the range of relative energy release rate when a structure is stressed from minimum to maximum load.

Based on the relation between energy release rate (G) and stress intensity factor (SIF) given by Eq. (2–8) [46]. The fatigue properties c_3 and c_4 are related to Paris law parameters C and m given by Eq. (2–9) and Eq. (2–10) respectively,

$$G = \frac{K^2}{E'} \tag{2–8}$$

where, $E'=E$ for plane stress and $E' = E/(1-\nu^2)$ for plane strain conditions. E is the Young's modulus of elasticity and ν is the Poisson's ratio.

$$c_3 = C \times E^m \tag{2–9}$$

$$c_4 = \frac{m}{2} \tag{2–10}$$

where, C and m are Paris' law parameters; and E is the Young's modulus of elasticity.

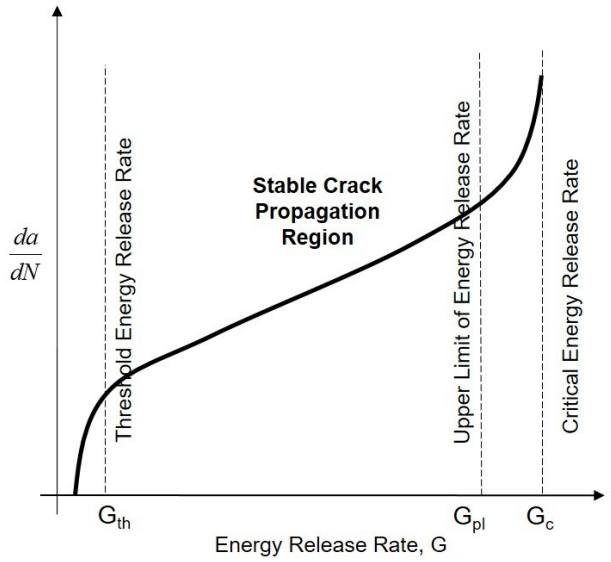

Figure 2-6: Fatigue crack growth with Paris law regime implemented in Abaqus®

Zhang et al. (2016) [16] used XFEM for low cycle fatigue analysis of offshore pipeline with embedded semi-elliptical crack subjected to cyclic tension load. A comparison between FCG

results from XFEM LCF analysis and that carried out using BS7910 method were in good agreement for the pipeline case studied [16]. Xiao et al. (2020) [62] performed fatigue crack initiation and growth investigation on steel pipeline, containing 3D coplanar and non-coplanar semi-elliptical surface and elliptical embedded cracks, using XFEM. The authors concluded the reliability of the results in terms of fatigue crack growth rate and fatigue life, from XFEM upon comparison with the available experimental results found in open literature [62].

Various approaches and research works carried out to tackle the fatigue cracking threat in pipeline from fatigue crack initiation phase to propagation phase was discussed. Capabilities of XFEM implemented in Abaqus® for modeling quasi-static crack growth and LCF crack growth analysis were discussed. In this study, HCF crack growth analysis in oil and gas pipelines subjected to internal pressure cycling, which are usually lower than the maximum operating pressure which could cause the material to yield, that closely resembles the actual operating condition using XFEM is presented.

2.3 Fatigue Crack Driving Parameter Estimation based on Fracture Mechanics

Fatigue crack driving parameters can be estimated numerically either through conventional FEM or XFEM. To explicitly model cracks in conventional FEM, singular finite elements are used to represent the asymptotic displacement field at the crack tip. Thus, this requires a conforming mesh to ensure a smooth and accurate interpolation of the solution over the crack surfaces, as well as focused mesh to ensure accurate representation close to the crack tip or front. Consequently, re-meshing is required for growing cracks or crack analysis with different crack sizes.

As an extension of the conventional FEM, XFEM is based on the concept of partition of the unity and was first introduced by Belytschko et al. (1999) [56]. The displacement fields in XFEM, as given in Eq. (2–11), is approximated by introducing local enrichment to the elements that are cut by the crack. The nodes of those elements are enriched by introducing an additional set of degrees of freedom (DOFs) with both crack tip enrichment and cross-crack enrichment along with their traditional DOFs denoted by u_i in Eq. (2–11):

$$u = \sum_{\text{i}\in\text{All Nodes}} u_i N_i + \sum_{\text{j}\in\text{Type \#2}} b_j N_j H(x) + \sum_{\text{k}\in \textit{Type}\#1} N_k \left(\sum_{l=1}^{Ty} c_k F_l(r,\theta) \right) + \sum_{\text{m}\in\text{Type}\#3} N_m \left(\sum_{l=1}^{Ty} c_m F_l(r,\theta) \right) \quad (2\text{–}11)$$

where, u_i is the nodal displacement vector; b_j , c_k and c_m are additional degrees of freedom for enriched nodes as indicated in Figure 2-7; N_{i}, N_{j}, N_{k} and N_{m} are the shape functions; *H(x)* is the Heaviside (jump) function across the crack surface given by Eq. (2–12); F_l is the asymptotic crack tip function, and T_y is the number of asymptotic crack tip functions (T_y = 4 for linear elastic materials) given by Eq. (2–13):

$$H(x) = \begin{cases} 1 & ;(\mathbf{x}\text{-}\mathbf{x}^*).\mathbf{n} \geq 0 \\ -1 & ;\text{Otherwise} \end{cases} \quad (2\text{–}12)$$

where, ***x*** is a sample point in the FE domain, ***x**** is the point on crack closest to ***x*** and ***n*** is the unit normal at the crack tip.

$$F_l = \left[\sqrt{r}\sin\frac{\theta}{2}, \sqrt{r}\cos\frac{\theta}{2}, \sqrt{r}\sin\theta\sin\frac{\theta}{2}, \sqrt{r}\sin\theta\cos\frac{\theta}{2} \right] \quad (2\text{–}13)$$

where, (r,θ) is a polar coordinate system with the origin at the crack tip.

For example, in Figure 2-7, a 2D finite element domain is discretized into 4×4 grid. Nodes with red dots (*Type #1*) represent nodes at the crack mouth, nodes with blue dots (*Type #2*) represent nodes that are cut by the crack body and nodes with orange dots (*Type #3*) represent nodes at the crack tip. Note that ***s*** is the unit tangent to the crack tip and ***n*** is the unit normal to the crack tip.

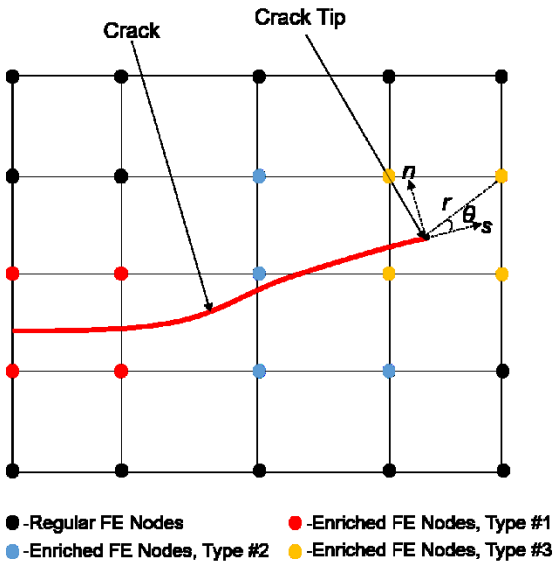

Figure 2-7: Schematic diagram of finite element domain enrichment in XFEM

As it can be seen in Eq. (2–11) the displacement field in XFEM is approximated by some additional enrichment functions compared to the conventional finite element formulation. The first term is same as the standard FE formulation, while the second term accounts for jump in displacement caused due to discontinuity (referred to as cross-crack enrichment), and the last two term captures the singularity around the crack tip (referred to as crack tip enrichment). Due to such enrichment in XFEM, finite element meshing can represent discontinuity inside elements through local enrichment functions and additional nodal DOFs (i.e., independent of FE mesh). As such, no re-meshing is needed for growing cracks or analysis of cracks of different crack sizes. The term crack tip is used for 2D cracks as shown above and referred to as crack front for 3D cracks dealt in later sections. The solution technique of conventional FEM and XFEM are similar. In commercially available FE analysis software package Abaqus®, both FEM and XFEM problems can be solved using direct linear equation solver or iterative solver with Newton or quasi-Newton technique. For further details on different solution algorithm readers can refer to [60].

As seen in Eq. (2–2), the fatigue crack growth rate is related to the range of stress of intensity factor. The range of stress intensity factor, ΔK is defined as the difference in the values of SIF when a structure is subjected to the maximum and the minimum load. Abaqus® can be used for determining SIF as used in this study. SIF is extracted in Abaqus® using *J*-Integral, which is

defined in terms of strain energy release rate (G) as crack tends to advance [60]. As explained earlier, for linear elastic and non-linear elastic materials in 2D plane, the strain energy release rate is related to the stress intensity factor as $J = K^2 / E'$; where E'=E (Young's modulus of elasticity) for plane stress condition and $E' = E/(1-\upsilon^2)$ for plane strain condition; υ is the Poisson's ratio. However, for a 3D numerical model extraction of SIF from J-Integral is slightly different and achieved using the relation as shown in Eq. (2–14). For further details on this readers can refer to the Abaqus® user manual [60].

$$J = \frac{1}{8\pi}\mathbf{K}^T.\mathbf{B}^{-1}.\mathbf{K} \tag{2–14}$$

where, $\mathbf{K} = \left[K_I, K_{II}, K_{III}\right]^T$ are stress intensity factors along normal (mode I), shear (mode II) and tangential (mode III) directions and **B** is pre-logarithmic energy factor matrix, which is diagonal for homogeneous isotropic material [60].

Fakkoussi et al. [63] and Coelho et al. (2017) [64] reported the comparative study of the fatigue crack driving parameter SIF values obtained using XFEM, FEM and analytical methods. The authors concluded the robustness and reliability of the XFEM. Mora et al. (2021) used XFEM to estimate SIF in a core region of the reactor pressure vessel considered as a hollow cylinder with different defect or crack sizes when subjected to thermal shock. The SIF estimated using XFEM was verified against the values obtained using weight function formula (WFF) and were found to give good results [65]. Olamide et al. (2020) used conventional FEM to estimate SIF for a pipe segment with semi-elliptical circumferential crack. The results obtained were compared with other analytical, numerical results with reasonably good agreement [66].

A brief background on formulation of XFEM and implementation of numerical method of computing SIF in Abaqus® for estimation of SIF was presented above. SIF estimation related works using XFEM and FEM carried out by other researchers were also presented. In this study, comprehensive details related to reliable estimation of SIF using XFEM compared to FEM and Analytical method are presented. To be specific, selection of finite element types, mesh size,

different meshing strategies and enrichment radius (singularity calculation radius) are discussed in detail.

2.4 Surrogate Modeling for Fatigue Crack Driving Parameter Estimation

Surrogate models, also known as meta-models, are approximation models that mimic the behavior of the simulation model as closely as possible while being computationally cheap. It is constructed based on modeling the response of the simulator to a limited number of intelligently chosen data points. Surrogate models are used for estimating system response and supporting decision making in engineering processes with a focus on pointwise estimation [67].Well-known surrogate models include polynomial response surface, linear or nonlinear regression, kriging (i.e., Gaussian process regression), polynomial chaos expansion, radial basis function, support vector machine, and artificial neural network. Data driven surrogate models establish relationship between input vector and output response with an error quantifying deviation of target output and prediction as given by Eq. (2–15):

$$\mathbf{y} = f(\mathbf{x}) + \varepsilon \tag{2–15}$$

where, **y** is the response, **x** is the available data and ε is an error.

In order to measure the performance of a surrogate model, the error term quantifying the deviation of target output and the predictions are generally quantified using statistical performance function. Coefficient of determination (R^2) and the root mean squared error (*RMSE*) are the common metrics used to measure the performance of a surrogate model. Coefficient of determination (R^2) measures the proportion of the variance in the variability of the dependent variables that is accounted for in the model between the prediction and target and given by Eq. (2–16):

$$R^2 = 1 - \frac{SS_{\mathrm{Res}}}{SS_{Tot}} \tag{2–16}$$

where, SS_{Res} is the sum of squared residuals and given by Eq. (2–17) and SS_{Tot} is the total sum of squares given by Eq. (2–18):

$$SS_{Res} = \sum_{i=1}^{n} (y_i - f(x_i))^2 \tag{2–17}$$

where, x is the available sample data, y is the target, and $f(x)$ is the prediction.

$$SS_{Tot} = \sum_{i=1}^{n} (y_i - \bar{y})^2 \tag{2–18}$$

where, $\bar{y}$ is the average of the target values y.

Root mean squared error (*RMSE*) is the mean squared root of the SS_{Res} and is given by Eq. (2–19):

$$RMSE = \sqrt{\frac{1}{n} \sum_{i=1}^{n} (y_i - f(x_i))^2} \tag{2–19}$$

Higher the value of the coefficient of determination (R^2), the better the model prediction. Alternatively, lower the value of *RMSE,* the better the model prediction.

Some initial efforts on using surrogate modeling can be found in the pipeline engineering for pipeline reliability analysis by Yang et al. (2013) [68] ; Hassanien et al. (2016) [69]. Xie et al. (2018) used polynomial surface fitting method to fit the data points of SIF obtained using 3D FE model of a pipe with semi elliptical crack front on the external surface and reported to have good goodness of fit [70]. Salemi et al. (2020) also used polynomial surface fitting and GPR to build surrogate models to predict SIF for pipelines with a semi-elliptical outer surface crack, trained using data points from 3D FE models. Loghin et al. (2020) used response surface modeling based on radial basis function as a surrogate model to predict SIF and crack path trained using three-dimensional (3D) finite element models of a laboratory specimen. The authors concluded use of 3D FE models and the surrogate model provided an accuracy-runtime trade-off that extended its application to component level probabilistic life assessment [71]. Surrogate models aim to reproduce the underlying relation between input and output based on the training data-set obtained from high-fidelity models but at very less computational expense [72].

In the following sections the published works and efforts made by various researchers related to GPR and other surrogate models for prediction of fatigue crack driving parameters like SIF, *J*-Integral are discussed.

2.4.1 Gaussian Process Regression for SIF Estimation

A Gaussian Process regression (GPR) is a non-parametric, kernel-based probabilistic model to approximate the underlying relationship between inputs and output response, as will be discussed in details in Chapter 4. Specific to fatigue life analysis of pipelines, Keparate et al. (2017a) [73] used adaptive Gaussian process regression as an alternative to conventional FEM in ANSYS to predict the SIF. Furtherly, Keprate et al. (2017b) [74] compared different meta-modeling approaches to predict the SIF of semi-elliptical cracks in plates and recommended the GPR as the best surrogate model for predicting SIF, and GPR was chosen as it could quantify the uncertainty in the predicted values. Salemi et al. (2020) [75] also employed GPR as a surrogate model to predict SIF values of a flawed pipeline. Selection of appropriate kernel or co-variance function and sensitivity towards length scale parameter in GPR modeling is discussed [75]. Additionally, GPR models were reported to perform bad when extrapolating the values and recommended on having as many boundary points as possible [75].

Leser et al. (2017) [76] used SIF from finite element models of a single-edge notched specimen with two holes created using FRANC3D with thirty different crack initiation locations to build GPR model to estimate SIF and coupled it with crack growth algorithm for remaining useful life (RUL) estimation. The GPR model was built using "*scikit-learn*" learn library in Python programming language [76].

2.4.2 Others

An artificial neural network (ANN) as per Maureen et al. (1989) is defined as a computing system made up of number of simple, highly interconnected processing elements, which process information by their dynamic state response to external inputs. Jang et al. (2020) proposed an approach based on machine learning technique to estimate *J*-Integral, an elastic plastic fracture parameter, for surface cracked pipelines. Deep multilayer perceptron ANN models based on

training dataset from FE models were developed and concluded to have better accuracy compared against closed-form solution [77].

Keprate et al. (2017) proposed using gradient boosting regression to predict SIF values of a crack propagating in small bore pipe and was reported to have reasonable accuracy and reduced computation time [78]. Hoffman et al. (2016) used response surface polynomials, ordinary krigging and interpolation to estimate stress intensity factor influence coefficient in a flawed reactor pressure vessel and reported to have good performance for interpolated values only when compared with the benchmark solution [79].

2.5 Bayesian Approach for Fatigue Crack Growth Estimation

Paris' law as described earlier is a physics-based model that describes the Fatigue crack growth (FCG). Crack sizes obtained using measurements such as from ILI, in-ditch measurement or any other technique can be utilized for estimation of the fatigue model parameters such as C and m. If the crack size measurement data is error free, the model parameter estimation is a straight forward task. However, in reality there is always measurement uncertainty and the physics-based method has its own limitations in accuracy. Different kinds of ILI tools such as Magnetic flux leakage (MFL), Ultrasonic (UT) tools, Electromagnetic acoustic transducers (EMAT) etc. are used in the pipeline industry with their respective capabilities, limitations and accuracy [80]. Xie et al. (2018) proposed an integrated approach for pipeline FCG prediction with large crack sizing uncertainty, which integrates physics- based model and the ILI data using Bayesian method. The study demonstrated promising results using the approach and concluded that the FCG prediction can be more accurate with the improvement in the accuracy of the ILI tool [70].

A Bayesian approach provides a method to express degree of belief on a certain event based on the collected information such as ILI measurements and knowledge about a process such as Paris' law for FCG [81]. This is because Bayes' theorem describes the probability of an event (posterior) based on the previous knowledge (prior) and likelihood of its occurrence for given set of observations. To be specific, if $\boldsymbol{\theta}$ is the model parameter, which is used to describe a physical process, it can be estimated from a given set of observations $\mathbf{X}$. The updated estimate of the parameter, considering the observations of the actual physical process, according to Bayesian approach would be given by Eq. (2–20):

$$P(\boldsymbol{\theta} \mid \mathbf{X}) = \frac{L(\mathbf{X} \mid \boldsymbol{\theta}).P(\boldsymbol{\theta})}{P(\mathbf{X})} \tag{2–20}$$

where, $P(\boldsymbol{\theta} \mid \mathbf{X})$ is the posterior probability density function (PDF) of $\boldsymbol{\theta}$, $L(\mathbf{X} \mid \boldsymbol{\theta})$ is the likelihood of making the observations $\mathbf{X}$ given the parameter, $P(\boldsymbol{\theta})$ is the prior PDF of $\boldsymbol{\theta}$, and $P(\mathbf{X})$ is marginal density function of $\mathbf{X}$ or also known as normalizing constant to make integral of posterior PDF to be one.

In this study, epistemic uncertainty or reducible uncertainty in the estimation of fatigue model parameters and crack size is dealt. This can be achieved by improving the knowledge about the process based on the observed data.

The uncertainty in tools are inherent due to various factors like signal interference and cannot be reduced to zero but can be reduced to levels where the desired accuracy can be achieved. As such, Fang et al. (2017) presented a detailed literature review on commonly used ILI tools, for e.g. UT, MFL, EMAT, including technical principles, signal analysis, defect sizing method and inspection reliability [82]. Pipeline Research Council International (PRCI) reported that the industry EMAT ILI performance validation result shows the probability of sizing of 80% at 95% confidence for crack depths, which meet the tool performance specification. The results are in line with that obtained by Enbridge from a EMAT performance validation program on a Canadian gas transmission pipeline [83]. The field results were used to determine the crack depth and length sizing accuracy. In a program to test the performance of EMAT ILI tools performed at PRCI ILI test facility by Katz et al. (2017) crack depth sizing accuracy of ±15% of pipe wall thickness with an 80% confidence was reported. However, the crack lengths reported by EMAT tool were longer than field measurement [84].

However, leveraging the power of crack size measurement data and the existing FCG models can be a promising solution to improve the confidence in the crack size measurements and to make better prediction of the fatigue crack growth, which is beneficial for predictive maintenance of pipelines against fatigue cracks. In the following section different methods of implementing

Bayesian approaches to reduce the epistemic uncertainty in model parameter and crack size estimation is discussed, including the relevant works from other researchers.

Stochastic filtering, as an iterative Bayesian approach, can be used for extraction of information about unknown model parameters and crack states at certain time of interest by using data measured up to and including that point of time. Essentially, it provides a 'best estimate' for the true value of the state for a system or process based on noisy observations available, and the updated model can be further used for better predictions. Performance of the stochastic filtering method is usually measured by the stability of the estimated mean values and its confidence interval (CI). CI of a mean is a range of mean values bounded by lower and upper limit. 95 % CI is the most commonly used confidence level, it is the range of estimated mean between 2.5 and 97.5 percentile values. For a normal distribution, 95% CI is ±1.96 times the standard deviation. Narrower the CI higher the confidence in mean or the estimation is reliable.

2.5.1 Particle Filter (PF) for FCG Model Parameter and Crack Size Estimation

Particle filtering (PF), as a MC sampling-based filtering method where distributions are approximated by a discrete set of weighed particles representing probabilistic information, is a promising tool for stochastic estimation of state (e.g., crack size) and model parameters. Cadini et al. (2009) employed PF for structural prognostic problems and to estimate the distribution of structural component's remaining lifetime [85]. Wang et al. (2015) used PF along with Paris' law for diagnostics and prognostics of a single-crack near fastener hole specimen. Performance of PF was reported to be superior even though the computational cost was high and author also proposed a modification in the prediction step of PF to save on computational expenses [86]. Robinson et al. (2016) presented comparative study between interval technique, a deterministic method, and two stochastic non-linear prognosis methods [87]. Liu et al. (2017) coupled PF and Paris' law to predict fatigue crack growth model parameters and crack size. The coupled method was reported to produce accurate results of monitoring degradation of gear and residual fatigue life [88]. Yang et al. (2017) used deterministic resampling PF for crack size and crack growth model parameter estimation in edge-crack specimens [89]. Besides fatigue crack growth, PF has been employed in robot tracking, lithium-ion batteries, rolling bearings and so on [90]. Note that in these estimation

problems when model parameters are unknown and assumed to be time invariant, the parameters are jointly estimated by augmenting the parameters to the state vector [91].

2.5.2 Others

There exists various stochastic filtering approaches, such as Kalman filter (KF), extended Kalman filter (EKF), and unscented Kalman filter. Kalman filter (KF), a pioneer method in the estimation problem, provides optimal solution for linear problems with Gaussian noise. Furthermore, extended Kalman filter (EKF) and unscented Kalman filter (UKF) are more sophisticated version of KF built to deal with non-linear system with Gaussian noise assumptions and reported to have poor performance for highly non-linear system [89].

Ray et al. (1996) used EKF for real time computation of the fatigue rate and fatigue damage accumulation in aluminum alloy specimen and verified the results against the experimental data and also pointed out that EKF can be used for crack size following normal distributions only [92]. Moussas et al. (2005) compared Adaptive Lainiotis Filter (ALF), a multi-model partitioning algorithm, with EKF for FCG monitoring and identification and reported ALF to have superior performance over EKF for both parameter identification and residual fatigue life estimation [93]. Cobb et al. (2008) studied a fatigue crack growth estimation problem by utilizing data from energy-based wave propagation model from ultrasonic tools as the measurement model and Paris' law as the system model in Kalman Filter. They reported that their approach provided highly accurate crack size estimates compared to those observed from either methods alone [94]. Wang et al. (2016) presented a comparative study for joint estimation of crack size and Paris law parameters of an aircraft fuselage panel using both EKF and UKF, and concluded that EKF provided results within comparable accuracy to UKF but at less computational expense [95]. Wang et al. (2019) proposed a coupled EKF-linearization method which provided satisfactory results for fatigue crack growth model parameter estimation, and future crack growth trajectory prediction of an aircraft fuselage panel [96]. Besides fatigue crack growth, UKF has been employed in other engineering problems, e.g., parameter estimation of resistor-capacitor building energy models [97] and complex non-linear finite element models [98].

Stochastic filtering technique is widely used for diagnosis and prognosis of threats caused by fatigue cracking in various structures as discussed above. Despite being a powerful and robust tool

for FCG model parameter and crack size estimation, not many works in the field of oil and gas pipelines for FCG monitoring can be found. However, utilizing Bayesian approach based on stochastic filtering methods can help make better predictions even with the limited number of data and is discussed further in Chapter 5 of this thesis.

CHAPTER 3: CRACK PROPAGATION MODELING AND STRESS INTESITY FACTOR ESTIMATION FOR FATIGUE CRACK GROWTH ANALYSIS

3.1 Introduction

This chapter presents comprehensive details of numerical methods of modeling different types of crack propagation using conventional FEM and XFEM. Numerical modeling techniques has been proven to be a reliable alternate to full scale tests for pipelines to model different kinds of crack propagation mechanism. First, a brief introduction and previous works relevant to crack modeling using FEM and XFEM is presented. Quasi-static crack propagation analysis based on cohesive zone modeling (CZM) with traction separation law (TSL) is a popular method for modeling crack propagation in numerical modeling techniques like FEM and XFEM. Burst pressure estimation of a pipelines with internal and external surface cracks using XFEM implemented in Abaqus® with damage modeling based on maximum principal stress and fracture energy is presented to demonstrate the capabilities and robustness of XFEM for quasi-static crack propagation simulation.

In order to model fatigue crack growth (FCG) reliable estimation of stress intensity factor (SIF) along with other material properties plays a crucial role. Analytical models for simple crack geometries are available in literatures. For complex and irregular crack geometries FEM with focused mesh which confirms to the crack geometry has been widely used. XFEM allows cracks to be modeled independent of the mesh in crack domain and can be utilized for building robust crack growth model by eliminating need of re-meshing or minimal re-meshing. A comparison of SIF estimated using FEM and XFEM along with various factors like mesh size, mesh design, number of contours, and enrichment radius (singularity calculation radius) is presented. Furthermore, the numerical methods are also used to estimate SIF for different crack geometries on pipeline body and compared with the analytical model available in API 579 and reasonable agreement is found. In the final section, a methodology to estimate FCG using SIF estimated from XFEM and relevant values of fatigue model parameters is presented with the help of case studies on a compact tension (CT) specimen and a pipeline.

3.2 Crack Modeling

For pipelines, existence of fatigue and/or SCC cracks poses a major integrity threat and has been a major concern especially in aged pipelines. Performing full-scale experiments on pipeline to study crack propagation under various pipe configurations and loading conditions is of significant value, but it is limited to knowledge of particular cases under restricted scenarios. Time and cost associated with the full-scale tests or even reduced-scale specimens has motivated researchers to use alternate methods based on numerical techniques such as FEM and XFEM in order to study the different types of crack growth mechanism. Using appropriate numerical techniques allows researchers to deal with pipelines subjected to complex loading and boundary conditions. Furthermore, parametric and sensitivity studies become much more feasible which otherwise would have been prohibitively time consuming and expensive using full-scale pipelines or even reduced scale specimens.

Finite Element (FE) method, one of the leading numerical methods used in various engineering fields, is widely adopted for evaluating fracture mechanics-based crack driving parameters and crack growth prediction under monotonically increasing loading or cyclic fatigue loading [99]. With the use of appropriate modeling strategy and analysis method, FEM is shown to be a viable tool for simulating cracks in metallic pipes [100]. Several researchers have discussed about the use of meshing strategy like spider web, wedge elements at the crack tip and number of contours for reliable and accurate estimation of SIF [101-103]. A detailed review on use of FE models for fatigue crack analysis in pipes which summarizes the studies focusing on the factors influencing the mechanism of crack growth, such as geometry and loading, can be found in Li et al. (2020) [99]. Branco et al. (2015) [104] used a FE model with adaptive re-meshing technique and appropriate sized mesh to estimate fatigue crack driving parameter like SIF and coupled it with fatigue crack growth model such as the Paris law to update crack dimension until pre-determined crack dimension was achieved to model fatigue crack growth. FE models are an alternative to the experimental method but still has cumbersome modeling procedure such as mesh design, mesh confirming to the crack, re-meshing, and also requires user's expertise to obtain reliable estimation for the SIF estimation or crack growth under quasi-static loading and fatigue loading.

In contrast, Extended Finite Element method (XFEM), first introduced by Belytschko et al. (1999) [56], has gained popularity for engineering problems with discontinuity such as cracked pipelines. In XFEM, cracks can be modeled independent of the actual structure providing flexibility of no re-meshing or minimal re-meshing. XFEM model can alleviate the need of focused meshing and minimal re-meshing is required. Even though XFEM has such potential for numerical simulation, it has not been widely used in fatigue growth analysis and fatigue crack driving parameter estimation of pipelines in the open literature except for few works by [63, 64] as discussed earlier.

In the following sections of this chapter: (a) Case study demonstrating capabilities of XFEM to model a quasi-static crack propagation in pipeline is discussed, (b) Case study demonstrating fatigue crack propagation in a compact tension (CT) specimen and pipelines using an alternate method i.e. indirect method is presented, with special focus on the fatigue driving parameter, SIF. For all the numerical simulations, the commercially available finite element analysis software Abaqus®19.0 is used in this study.

3.3 Quasi-Static Crack Growth Simulation

The crack defects in pipelines subjected to internal pressure can propagate in the radial direction (along the wall thickness) and/or the longitudinal direction (along the pipeline axis). The crack propagation below a critical size when subjected to monotonically increasing load usually grow in a stable fashion. Under such condition equilibrium can be assumed at each incremental load step and this type of crack growth can be taken as quasi-static in nature.

A case study showing capabilities of XFEM implemented in Abaqus® for quasi-static crack growth in pipeline to estimate burst pressure, i.e., where crack grows through wall thickness of pipeline, is presented in the following section.

3.3.1 Pipeline Section

Failure behavior of axially flawed pipelines was studied by Brazilian State Oil Company (Petrobras) [105], using a series of full-scale burst test on end-capped API 5L X60 grade pipe specimens. Dotta et al. (2004) [105] performed crack growth analysis for pipes having internal and external cracks with semi elliptical crack front taken from the experimental study, using plane strain finite element models. In this study, two pipelines with internal and external cracks from the

same experimental and numerical study presented in [105] are modeled to demonstrate the capabilities of XFEM implemented in Abaqus® for crack growth analysis under monotonically increasing internal pressure. The geometrical properties of the pipe and cracks are summarised in Table 3-1. The yield strength is 483 MPa and the ultimate tensile strength is 597 MPa. The Young's modulus of elasticity (E) and Poisson's ratio (v) are 210000 MPa and 0.3, respectively. The true uniaxial stress-strain response of the API 5L X60 steel used in Abaqus® is shown in Figure 3-1. The end caps are 20 mm thick and made up of steel having same E and v as pipe.

Table 3-1 Geometric properties of pipe and axial cracks

Outer Diameter, OD (mm)	**Wall Thickness, WT** (mm)	**Length, *L*** (mm)	**Internal Crack**		**External Crack**	
			Depth, *a* (mm)	**Length, 2*c*** (mm)	**Depth, *a*** (mm)	**Length, 2*c*** (mm)
508	15.8	3000	7	140	7	140

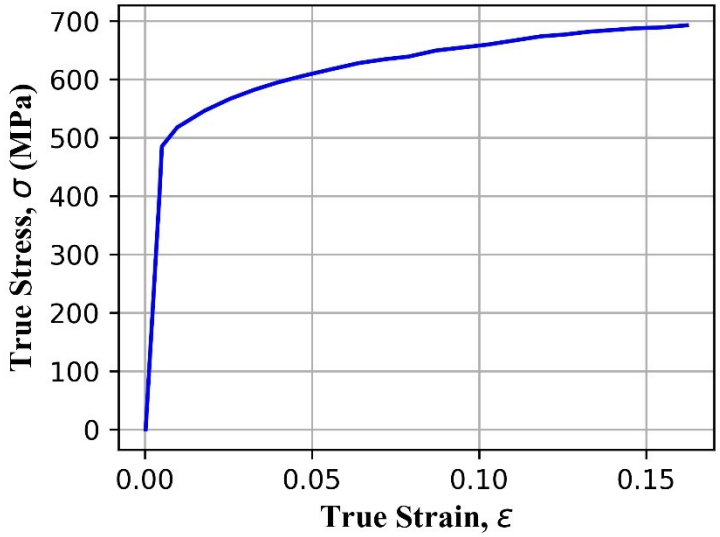

Figure 3-1: Uniaxial stress-strain response of API 5L X60 steel used in Dotta et al. (2004) [105]

3.3.1.1 Numerical modeling details

Two FE models of full-scale pipes with the geometric properties as given in Table 3-1 are developed in Abaqus®. In order to model the crack propagation XFEM implemented in Abaqus® is used. The XFEM model process begins with creating geometry of pipe as in conventional FEM and a crack feature is added to the geometry of the pipe making it independent of any mesh created

in the pipe. Following the modeling strategy used by Okodi et al. (2020) [59], three dimensional (3D) deformable solid elements with reduced integration (C3D8R) are used to model the pipe and end caps. In order to save the computational expenses utilizing symmetry of the pipe along the longitudinal direction, only half of the pipe length is modeled. Symmetric boundary condition along longitudinal direction, i.e. z- symmetry $(u_z = u_{rx} = u_{ry} = 0)$ on all faces of the circumference of the pipe is applied as shown in Figure 3-2 (a). The end plate and the pipe are connected using tie constraint. The boundary condition at the capped end of the pipe are pinned and only rotation about longitudinal axis is allowed $(u_x = u_y = u_z = u_{rx} = u_{ry} = 0)$ as shown in Figure 3-2 (b). Furthermore, the model constitutes two regions, viz. the crack domain and the non-crack domain, which allows using different fineness level of mesh as shown in Figure 3-3. The crack domain is a solid strip of size 20 mm × 15.8 mm × 140 mm, where mesh size of 1.53 mm × 0.55 mm × 2 mm is used along circumferential, thickness and longitudinal directions respectively. The meshing is shown in Figure 3-3 (b) and (c) for internal surface and external surface cracks respectively. The crack domain and non-crack domain are connected using tie constraints. This method of domain splitting is used in many studies ([48, 59]) for crack propagation simulation as it makes the modeling more robust and efficient. Whereas, the remainder of the pipe and end caps have relatively coarser mesh, overall mesh size of approximately 36 mm in pipe body and 8 mm in end cap is used. Internal surface of the pipe is subjected to internal pressure load applied in very small increments.

XFEM implemented in Abaqus® allows users to specify different damage initiation and evolution criteria. Since the study of sensitivity of different damage criteria are outside the scope of this work, in this study maximum principal stress (MPs) is used as the damage initiation criterion and fracture energy as damage evolution criterion with cohesive zone modeling based linear traction separation law. Maximum principal strain (MPe) damage initiation criterion has been already used by Okodi et al. (2020) for the exact same burst pressure estimation problem. In order to check the results and performance of XFEM based on different damage initiation criteria MPs is used in here. The damage modeling properties are given in Table 3-2. Zhang et al. (2016) [16] used maximum principal stress as damage initiation criteria in XFEM for X65 grade steel pipeline and recommended using the true ultimate tensile strength obtained from the tensile test as MPs. Hence, the value of maximum principal stress is adopted to be equal to true ultimate tensile strength from

the available test data. Whereas the value of fracture energy is adopted from Okodi et al. (2020) [59] as the pipe materials are from same X60 grade steel.

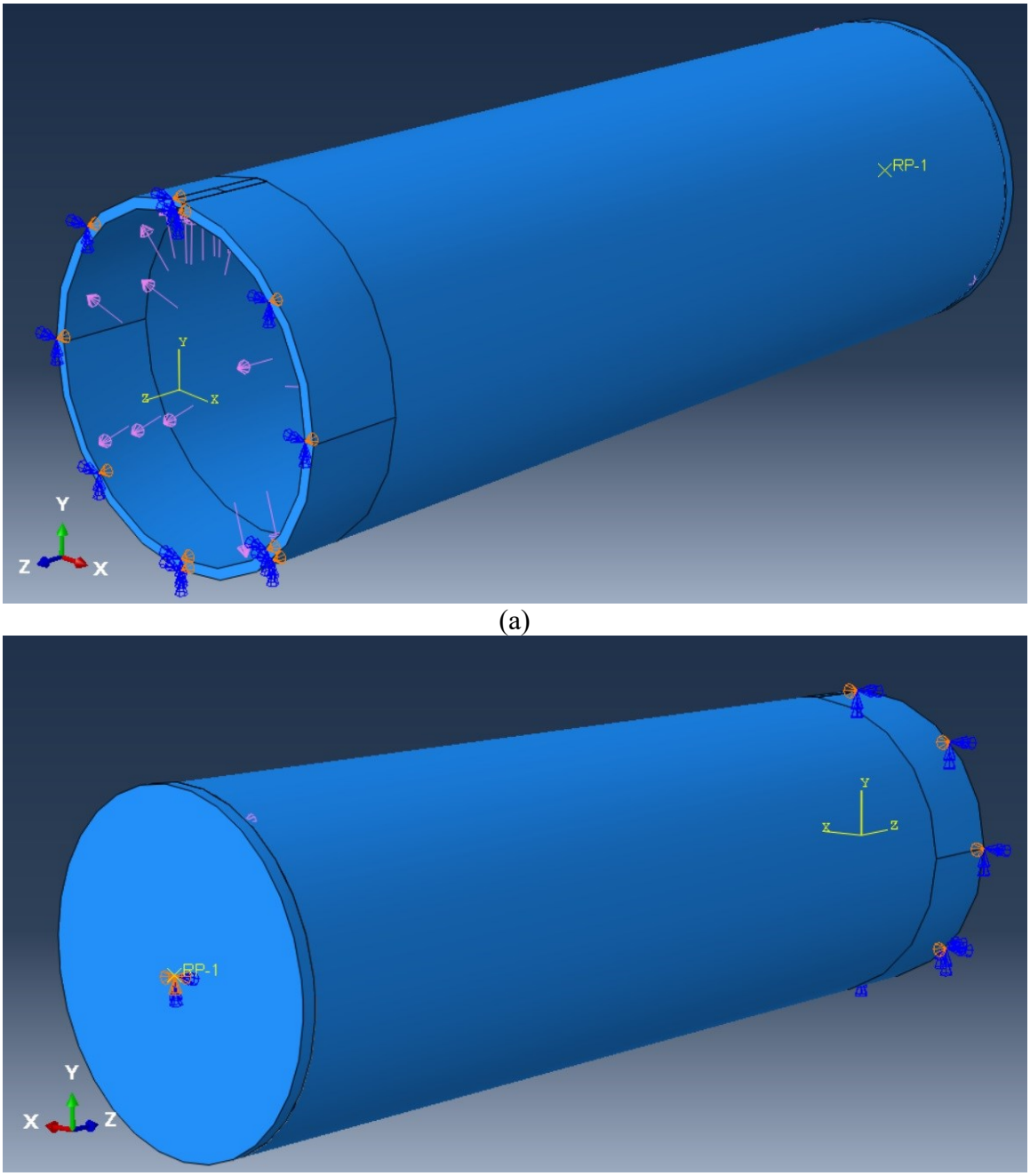

(a)

(b)

Figure 3-2: Typical 3D XFEM model showing boundary conditions used in the pipeline for estimation of burst pressure (a) z-axis symmetry condition at the half length, and (b) boundary condition at the capped end of pipe

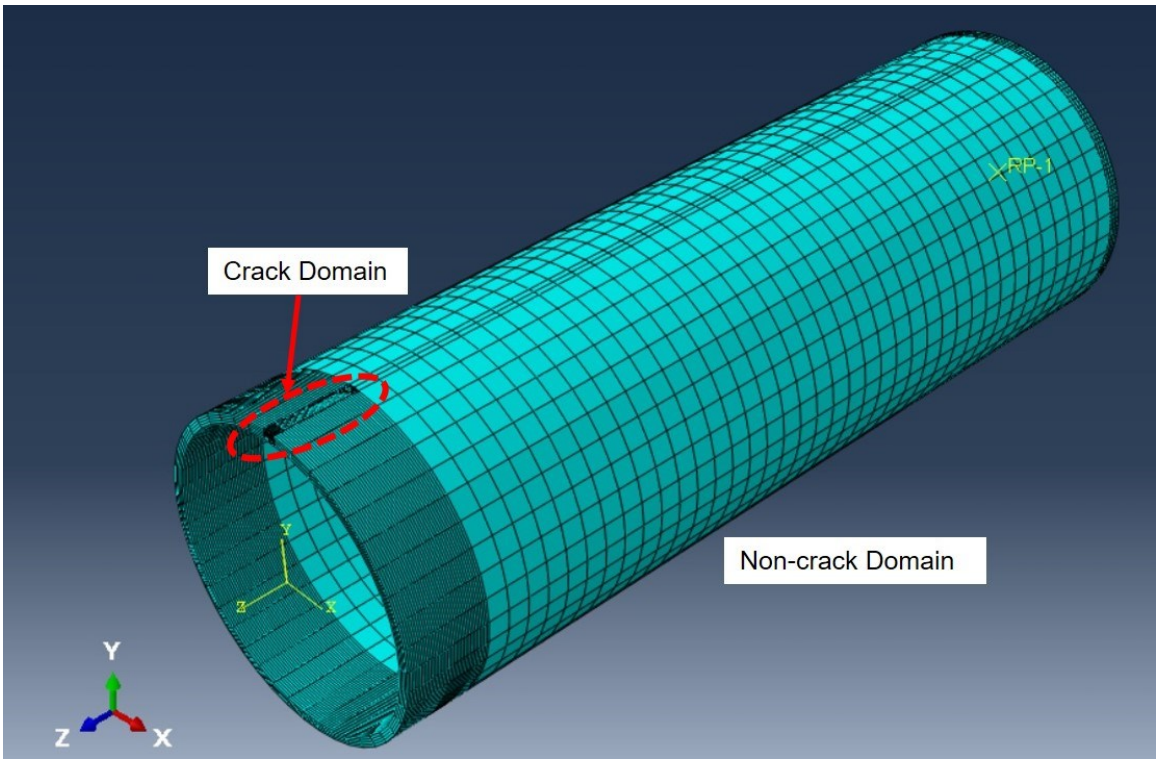

(a)

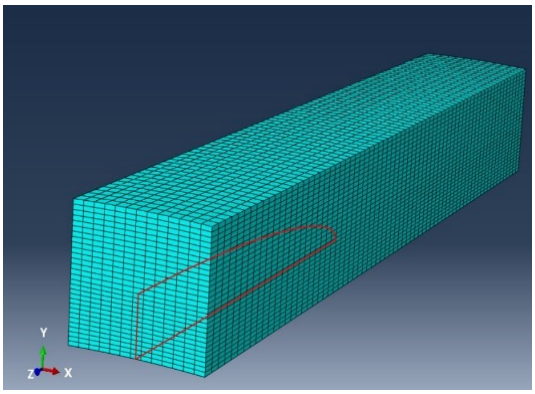

(b)

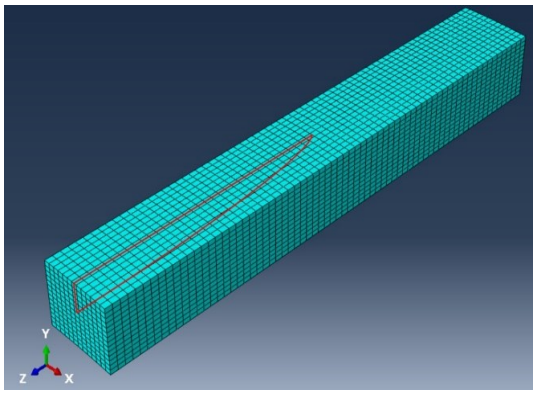

(c)

Figure 3-3: Overall view of a typical 3D XFEM model for burst pressure estimation with mesh (a) close-up view of crack domain with mesh and internal crack, and (c) close-up view of the crack domain with mesh and external crack (Note: Highlighted red solid curves are the XFEM crack feature)

Table 3-2 Damage modeling properties

Maximum Principal Stress (MPa)	692.6
Fracture Energy (N/mm)	150

3.3.1.2 Results and Discussion

The internal pressure load is applied to the internal surface of the pipe and increased quasi-statically to cause the element at the outermost end of the crack tip to fracture completely, leading to the burst failure. The corresponding internal pressure is considered burst pressure in this study. In order to estimate the burst pressure of the pipeline using XFEM in Abaqus® 'STATUSXFEM' variable is tracked, value of 1 represents complete fracture of the element. Figure 3-4 shows the status of the enriched elements in the pipeline, the red color of the elements with STATUSXFEM=1 representing complete fracture. To be specific, Figure 3-4 (a) shows the status of the enriched elements that represent the initial internal crack geometry and Figure 3-4 (b) shows the status of the enriched elements at internal pressure corresponding to the burst pressure i.e. final crack morphology of the initial internal crack. Similarly, Figure 3-4 (c) shows the status of the enriched elements that represent the initial external crack geometry and Figure 3-4 (d) shows the status of the enriched elements at internal pressure corresponding to the burst pressure i.e. final crack morphology of the initial external surface crack. Figure 3-5 (a) shows the internal crack growth with the increasing internal pressure using experimental and FEM results from [105], and XFEM. The crack size after 11.98 mm from experimental results was not presented and was reported to have propagated unstably in [105]. As mentioned earlier the elements were considered to be completely fractured when value of variable 'STATUSXFEM' is 1, see Figure 3-5 (c). At approximately same pressure (burst pressure), all elements ahead of the crack tip at the deepest location are completely fractured. After that, the crack propagation is unstable and represented by solid red line in Figure 3-5 (a). However, with the increasing pressure, elements ahead of the crack tip are fractured partially (see Figure 3-5 (b)) and represented by dashed red line in Figure 3-5 (a). The crack growth estimated from XFEM closely matches to that from experimental results even though the exact burst pressure are slightly off, as discussed in the following section. Also, the experimental results for external crack growth was not presented in [105] and hence left out here. Table 3-3 summarizes burst pressure estimated using maximum principal stress and fracture energy as damage parameters in XFEM. The results are compared to the burst pressure obtained by experiment and finite element method from Dotta et al. (2004) [105]. Dotta et al. (2004) performed non-linear FE analysis using WARP3D FE analysis code assuming plain strain condition achieved by using a single thickness layer 3D eight node trilinear hexahedral elements [105]. The burst pressure estimated for same crack geometry using different methods are in

reasonably good agreement with each other. XFEM estimated burst pressure for internal and external cracks are about 1.9 % and 5.4 % less than that from experimental results. The reason for this discrepancy is due to the specification of the damage initiation and propagation criteria. As mentioned earlier XFEM implemented in Abaqus® allows users to specify different damage modeling criterion. However, selection of appropriate set of parameters and calibration of these values are field of study being investigated by different researchers [59].

Table 3-3 Burst Pressure Comparison for API 5L X60 Grade Steel Pipeline

Crack Location and Geometry	**Burst Pressure** (MPa)		
	XFEM	**Experimental** (Dotta et al., 2004 [105])	**FEM** (Dotta et al., 2004 [105])
Internal (7 mm × 140 mm)	26.978	27.5	27.8
External (7 mm × 140 mm)	23.65	25.0	26.9

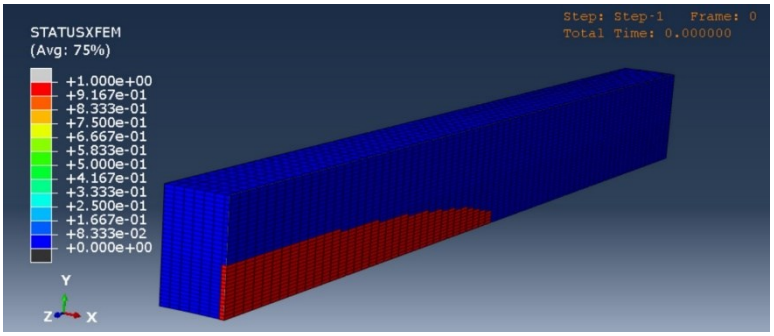

(a)

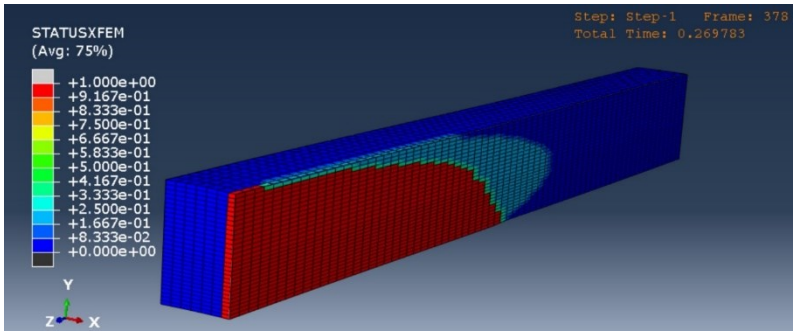

(b)

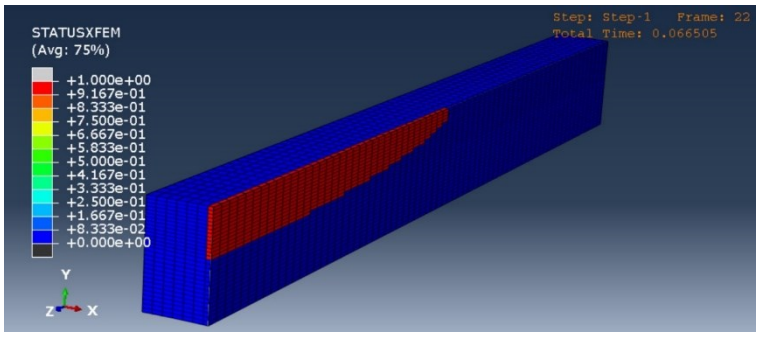

(c)

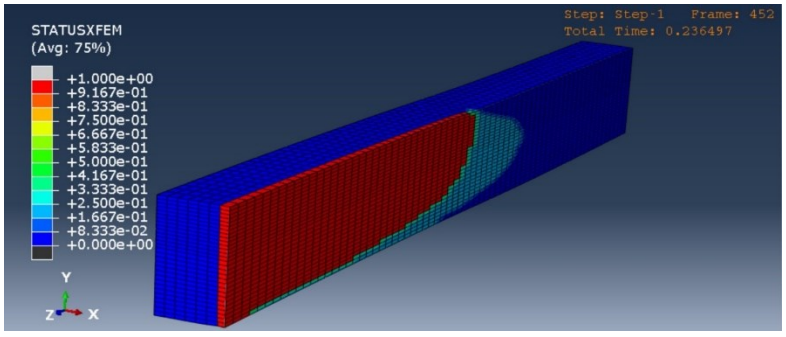

(d)

Figure 3-4: Longitudinal view of the crack domain showing status of enriched elements due to (a) initial internal crack, (b) internal crack at burst pressure, (c) initial external crack, and (d) external crack at burst pressure

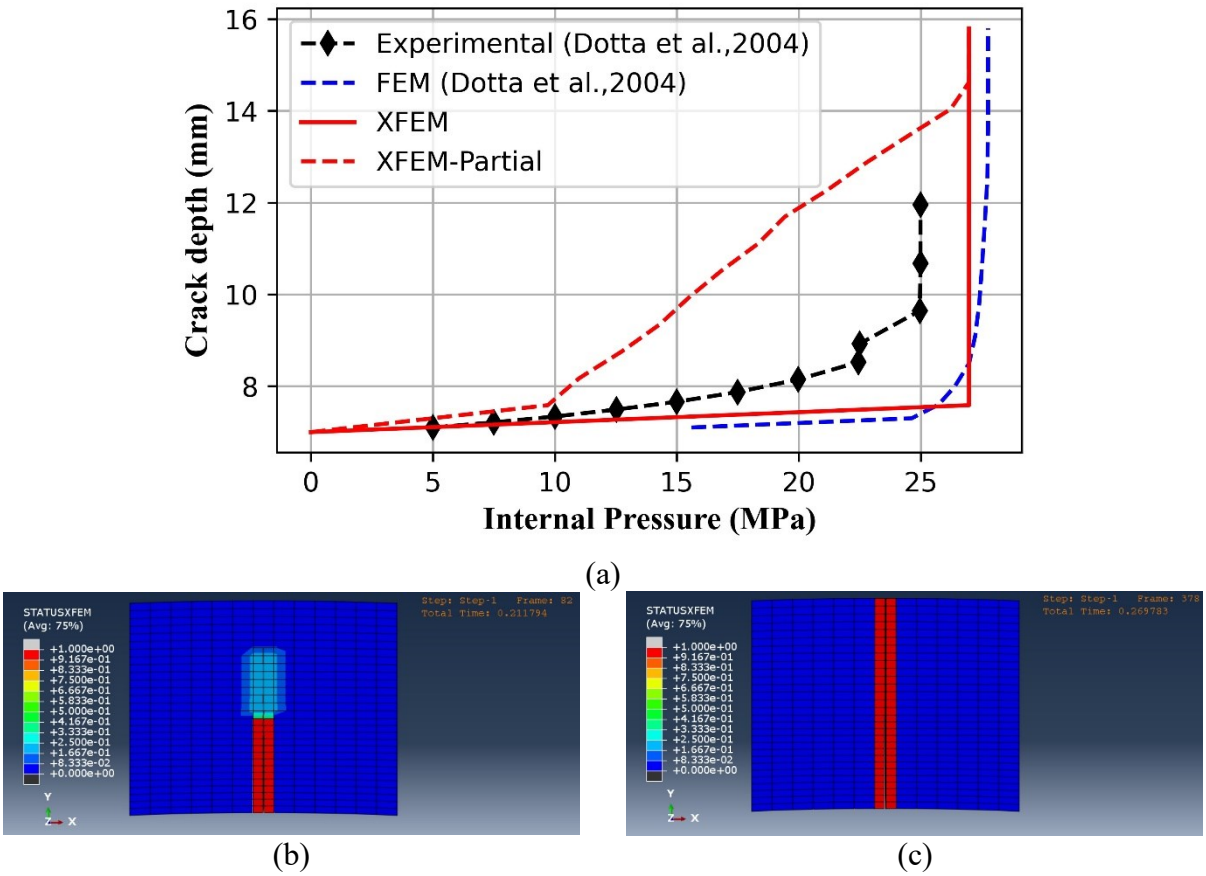

Figure 3-5: (a) Comparison of internal crack growth with internal pressure using various methods, (b) status of enriched element ahead of the crack tip showing partial fracture, and (c) status of enriched element ahead of the crack tip showing full fracture

3.4 Fatigue Crack Growth Modeling

The limitation of existing fatigue analysis code to perform LCF only as discussed in section 2.2.2.2, computational expenses and modeling complexity using conventional finite element analysis of component subjected to cyclic load lead to find an alternative method for fatigue analysis. A fracture mechanics based assessment of the fatigue crack growth rate with respect to loading cycles is related to the crack driving parameters like stress intensity factor (SIF) and crack growth resisting material properties. Paris law is one of such equations that quantifies the crack growth rate in the stable crack growth phase of fatigue life and given by Eq. (3–1):

$$\frac{da}{dN} = C(\Delta K)^m \tag{3–1}$$

where, da/dN is the rate of fatigue crack growth per loading cycle; C and m are fatigue properties of material; ΔK is the range of SIF when a structure is stressed from minimum to maximum load.

The fracture mechanics based assessment has been gaining popularity and incorporated in industry practiced standards like API 579 [10] and BS 7910 [42]. These standards provides analytical expression for estimation of SIF. Due to less conservative estimate of SIF using API 579 model compared to BS 7910, supported by many studies [63], is used in this study for comparison and other purposes discussed in the following sections. The values of the material properties C and m are recommended to be calculated experimentally in both standards, as they greatly depend on the factors like load ratio, and environment [106, 107]. In order to assess the fatigue crack growth in pipelines using Paris Law the values of C and m mentioned in API 579 (Clause 9F.5.3.2), for ferritic and austenitic steels in air or other non-aggressive service environment at temperatures up to 100 $°C$ and yield strengths less than or equal to 600 MPa, are 5.218×10^{-13} $(\text{unit}: mm/Cycle, MPa\sqrt{mm})$ and 3.00 respectively. Similarly, these values in BS 7910 (Clause 8.2.3.3), for steels (ferritic, austenitic or duplex ferrtic-austenitic) with yield strengths less than or equal to 700 MPa operating in air or other non-aggressive environments at temperatures up to 100 $°C$, are 3.980×10^{-13} $(\text{unit}: mm/Cycle, MPa\sqrt{mm})$ and 2.88 respectively for load ratio less than 0.5. In addition, 5.860×10^{-13} $(\text{unit}: mm/Cycle, MPa\sqrt{mm})$ and 2.88 for load ratio greater than or equal to 0.5.

FE Model of a component with XFEM crack feature is created in Abaqus® and static analysis is performed. From the generated output file of the XFEM analysis, fatigue crack driving parameters are extracted. Numerical estimation of fatigue crack driving parameters such as Stress Intensity Factor (SIF) and J-Integral as explained in section 2.3 and is used for estimating number of cycles required to extend crack by some predefined length, at least one element length ahead of crack tip. An Euler discretized form of the Paris' law is used as analytical solution of the differential equation due to complex formulation of the range of SIF is not always viable. The discretized form provides accurate results for engineering purposes and given by Eq. (3–2):

$$a_k = C(\Delta K_{k-1})^m \cdot \Delta N + a_{k-1} \tag{3–2}$$

where, a_k is the crack size at current time step *k*, ΔK_{k-1} is the range of SIF at the previous time step (*k-1)* when a structure is stressed from minimum to maximum load, ΔN is the number of load cycles, *C* and *m* are Paris' law model parameters. Note: When using discretized form of differential equations smaller the value of ΔN better the accuracy.

A flowchart to model fatigue crack growth using an indirect method is shown in Figure 3-6. A brief description of the method is as follows: start with a FE model of a pipe along with the crack geometry. Selection and use of appropriate FE modeling method i.e. either conventional FEM or XFEM is discussed in details in following sections. Fatigue crack driving parameter like SIF is extracted after analyzing and post processing the model. Use of analytical method for calculating SIF is equally applicable in this method. For a linear-elastic material once the SIF corresponding to the maximum load is evaluated it can be used to calculate the corresponding value at the minimum load and hence the range of SIF. If the calculated range of SIF is greater than the critical value of SIF it signifies that the unstable fatigue crack growth has started and the process is terminated. If not, number of cycles required to grow a crack by an incremental size is evaluated using the discretized equation given by Eq. (3–2). The relation can be used either by fixing the difference between number of load cycles (ΔN) corresponding to the increment in crack size (Δa) or vice versa. The crack geometry is then updated and checked if the critical crack size is reached or not. If yes, the process is terminated else a new FE analysis is performed with the updated crack geometry and repeated until critical values of either crack size or SIF is reached. In a previous study by the author [108], demonstration and potential of estimating FCG for CT specimen and pipeline section has been presented.

In the following sections, different SIF estimation methods like analytical and numerical methods are discussed. The section ends with demonstration of the methodology using different case studies.

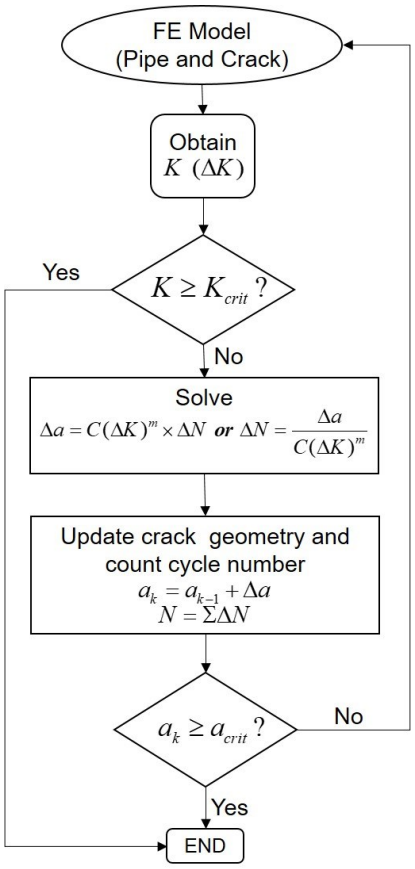

Figure 3-6: Flowchart showing the indirect method of fatigue crack growth

3.4.1 SIF Estimation Methods and Comparison

Estimation of SIF plays a vital role in assessing the state of the structure ahead of the crack tip or crack front. As shown in the previous section one of the important parameters for modeling fatigue crack growth is the range of SIF. Accurate SIF estimation is crucial as it has exponential relation with the crack growth as shown by Eq. (3–1). In this section, analytical method and two different numerical methods for SIF estimation are discussed in detail.

3.4.1.1 API 579 Model: Background and Formulation

API 579-1/ASME FFS-1 [109] provides an analytical of solution for estimation of SIF for different pipe and crack geometries. API 579 model for calculation of SIF is developed based on the influence coefficient approach, which basically employs the principle of superposition to a cracked body subjected to polynomial stress distribution and using Taylor series expansion to get the fourth

order polynomial. The influence coefficients are obtained from over 2700 finite element analyses [46], with a typical meshing strategy used as shown in Figure 3-8. Furthermore, a sixth-degree polynomial fit to the finite element results of SIF estimation from Franc2D software was used to obtain the influence coefficients [110]. Additionally, the 6th-order polynomial was fitted to the FEM results excluding those at the free surface and those values at the surface were estimated by extrapolating the polynomial fit. This was done because the results at the surface were unreliable and highly sensitive to mesh size, theoretically the value of SIF at the free surface of a 3D body is zero [46]. Further details about how the API 579 model was developed can be found in [110].

The values of SIF for a longitudinal crack with a semi-elliptical crack front on the outer surface of a pressurized cylinder, as shown in Figure 3-7 as per API 579-1/ASME FFS-1 [109], is given by Eq. (3–3):

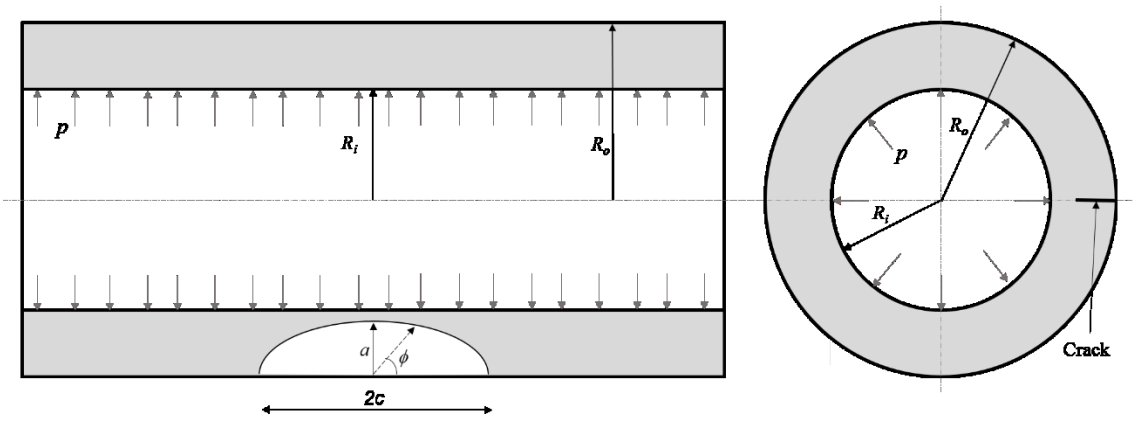

Figure 3-7. Longitudinal section (left) and cross section (right) of pipeline with semi-elliptical crack front on the external surface and subjected to internal pressure load

$$K_I = \frac{pR_i^2}{R_o^2 - R_i^2}\left[2G_o + 2G_1\left(\frac{a}{R_o}\right) + 3G_2\left(\frac{a}{R_o}\right)^2 + 4G_3\left(\frac{a}{R_o}\right)^3 + 5G_4\left(\frac{a}{R_o}\right)^4\right]\sqrt{\frac{\pi a}{Q}} \qquad (3\text{–}3)$$

where, p is the internal pressure, R_i is the internal radius, R_o is the external radius, Q is a crack geometry parameter and $G_0 - G_4$ are influence coefficients and valid for $0 \le t/R_i \le 1.0$,

$0.03125 \le a/c \le 2$ and $0.2 \le a/t \le 0.8$. The coefficients G_0 and G_1 are tabulated in Table 9B.13 of API 579 [10]. Whereas, $G_2, G_3,$ and G_4 are calculated based on G_0 and G_1, given by equations presented there. The equations for influence coefficients $G_2, G_3, G_4,$ and Q can be found in ANNEX-C.

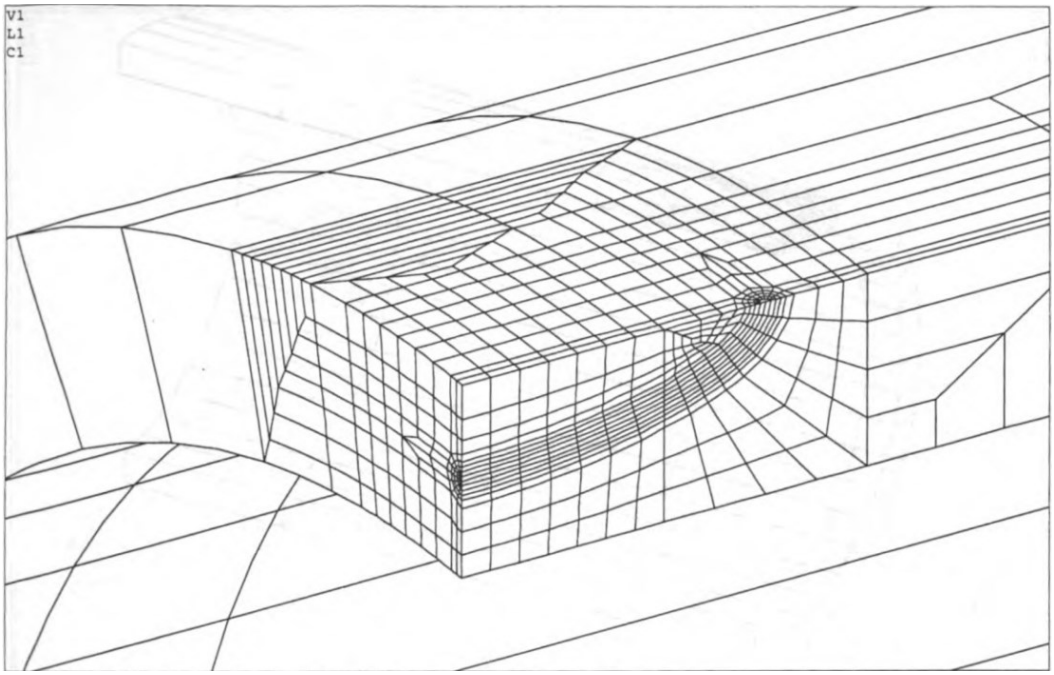

Figure 3-8: Typical meshing strategy used in FE models used for developing the API 579 model for SIF estimation [110]

3.4.1.2 Numerical methods for SIF estimation

In the next section, SIF estimation using conventional FEM and XFEM models are demonstrated. Firstly, a compact tension (CT) specimen with a straight crack front is presented. Sensitivity of the mesh size, selection of element type, number of contour integral request and other factors are dealt in detail. Finally, a pipeline section having semi-elliptical (curved) crack front is presented. Various factors such mesh size, element type, number of contour integral request and effect of curved crack front in SIF estimation are dealt in detail.

(1) CT Specimen

One of the nine CT specimens subjected to fatigue testing in Silva et al. (2011) [44] (designated as CTC5 in that study) is used for demonstrating SIF estimation method using FEM in Abaqus®. CTC5 specimen is chosen in this study because all of the specimens have approximately same geometric properties. Additionally, testing details and other information are clearly mentioned for this specimen in Silva et al. (2011) [44]. The geometric details, material properties, loading and boundary conditions are used from the literature [44] directly such that the numerical model closely replicates the experimental model presented. Figure 3-9 shows the geometric details of the CT specimen. The CT specimens were cut out from a pipeline section of API 5L X65 and Table 3-4 summarizes the material properties of the pipeline steel.

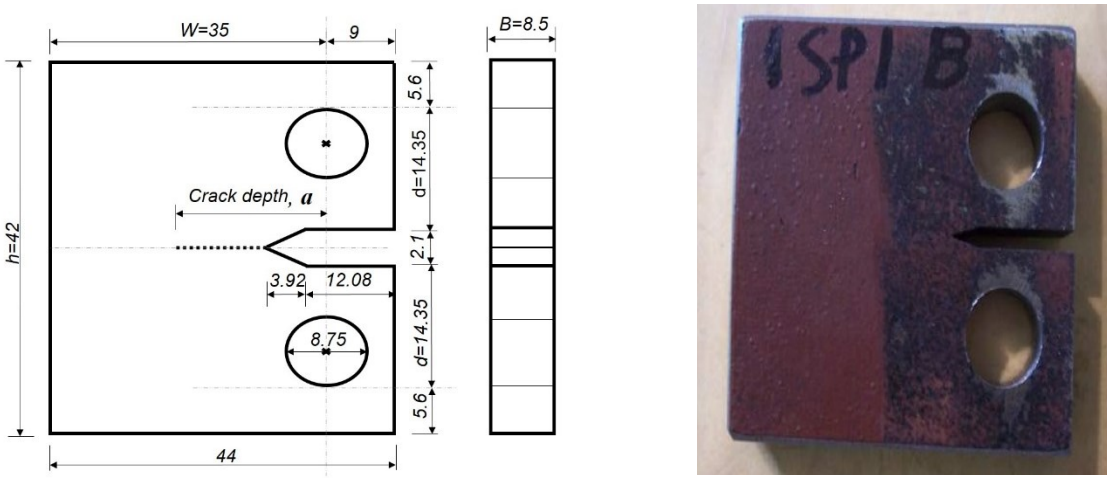

(a) (b)

Figure 3-9: (a) Geometric details of the CT specimen: flat view (left) and sectional view (right) and (b) CT specimen used in experiment [44] (Note: All dimensions are in *mm*)

Table 3-4 Material Properties

Young's modulus (*MPa*)	200000
Yield stress (*MPa*)	571
Ultimate stress (*MPa*)	709
Ultimate strain (%)	9.1
C $((mm/cycle)/(MPa.\sqrt{mm})^{m})$	1.504×10^{-16}
m	4.14

(a) Modeling Strategy

A 3D model of CT specimen is created, as in Abaqus® SIF can be requested for 3D models only while using XFEM, in order to make a fair comparison between conventional FEM and XFEM as discussed in the following sections. Both conventional FEM and XFEM models are created for the CT specimen described above. Figure 3-10 shows typical 3D finite element model of CT specimen used in this study. The lower clamp hole is pinned in all direction $(u_x = u_y = u_z = 0)$.The upper clamp hole is pinned along longitudinal and transverse direction $(u_x = u_z = 0)$ and subjected to concentrated load of 10 KN along the normal direction $(P_y = 10KN)$. As mentioned in [44]; material property of the CT specimen is assumed to be linear elastic, isotropic and homogeneous. The SIF has proportional relation with the load hence; the range of SIF (ΔK) is calculated once the value for maximum load $(P_{\max})$ is calculated. Even though modeling cracks in conventional FEM is a tedious job, the accuracy is higher due to less approximation compared to XFEM due to additional degrees-of-freedom (DOF) to the conventional DOFs as given in Eq. (2–11). The cracks studied here are sharp and the strain field becomes singular at the crack tip, including singularity in the model for small-strain analysis improves the accuracy of the contour integral as well as stress and strains [60]. In order to get as accurate result as possible, different kinds of meshing strategies and finite element types are used and compared. The estimated value of SIF is compared to that prescribed by ASTM E647 which given by Eq. (3–4):

$$\Delta K = \frac{\Delta P}{B\sqrt{W}} \frac{2 + a/W}{(1 - a/W)} \left[0.886 + 4.64\, a/W - 13.32(a/W)^2 + 14.72(a/W)^3 - 5.6(a/W)^4 \right] \quad (3–4)$$

where, $\Delta P = P_{\max} - P_{\min}$, B is the width of the CT specimen, a is the crack depth measured from center of clamp holes, W is the effective length of CT specimen.

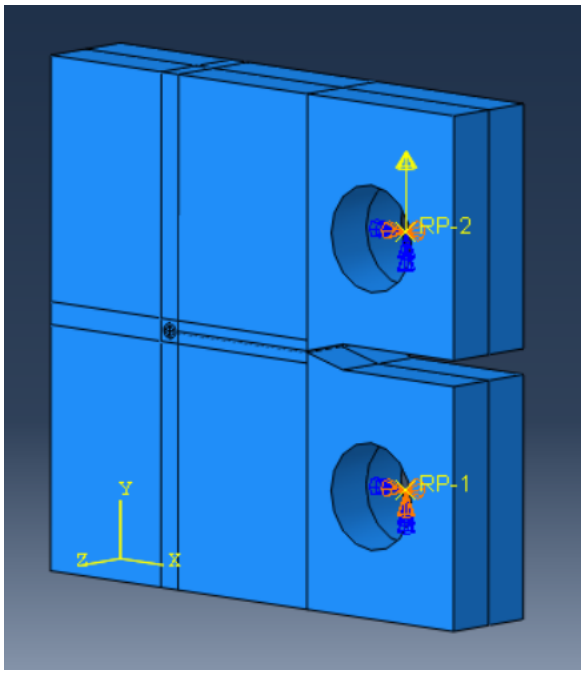

Figure 3-10: 3D finite element model with boundary conditions

(b) Mesh Design for FEM and XFEM Models

In conventional FEM mesh should confirm to the crack geometry. Figure 3-11 shows the meshing strategies used in conventional FEM model. Spider-web type mesh having wedge elements with reduced integration (C3D6R) as shown in Figure 3-11 (b) is used in the first contour region. Using this type of strategy improves the accuracy of the results by considering the singularity at the crack tip as recommended in [60]. In all other region hexahedral elements with reduced integration (C3D8R) is used. Also, a spider web type mesh with regular hexahedral elements with reduced integration (C3D8R) all over is used as shown in Figure 3-11 (c) in order to make comparison with the results obtained using XFEM. Reduced integration scheme is used to save on computational expenses.

Figure 3-12 shows the meshing strategies used in the XFEM model. Similar to FEM, two meshing strategies are deployed in XFEM models too. First, a general meshing strategy such that the cracks can be modeled independent of the mesh as shown in Figure 3-12 (b). The other meshing strategy is similar to that used in conventional FEM as shown in Figure 3-12 (c). The C3D8R elements are used in entire XFEM model. XFEM implemented in Abaqus® 6.19 does not support wedge elements (C3D6R) yet. It should be noted that crack can be modeled independent of mesh even if

an unfocused type of meshing strategy is used. However the mesh size around the crack tip should be sufficiently small to capture the response accurately [60]. Which in turn increases computational time but the tedious modeling time is reduced remarkably.

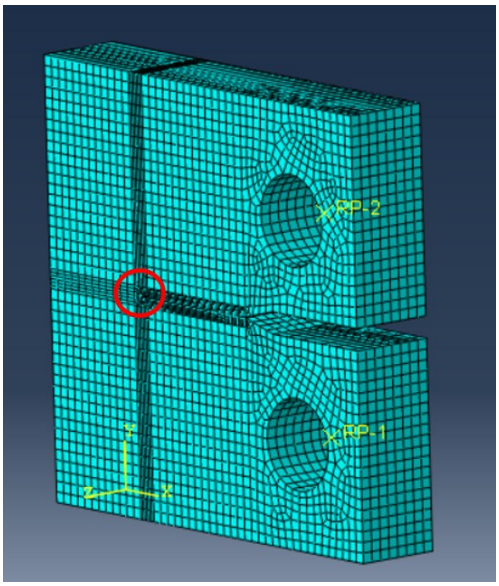

(a)

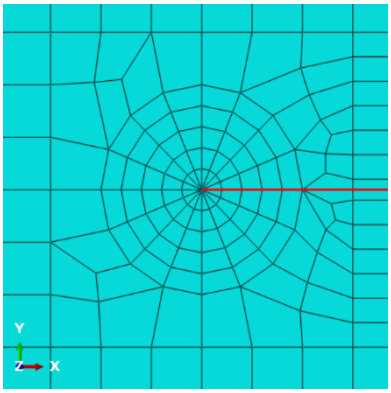

(b)

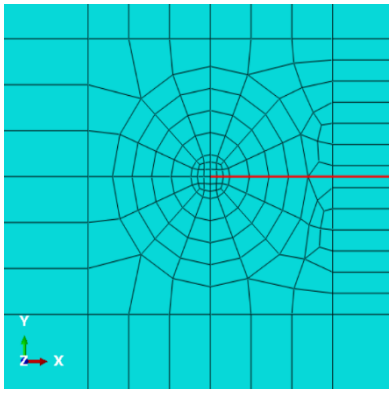

(c)

Figure 3-11: (a) Overall mesh design in the CT specimen using conventional FEM method, (b) Mesh type #1 and element type used in the crack tip zone (red circle in (a)), and (c) Mesh type #2 and element type used in the crack tip zone (red circle in (a)). Note: Red lines in (b) and (c) is crack

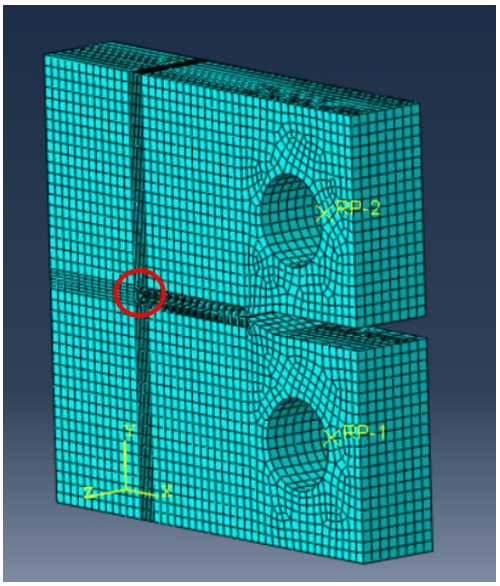

(a)

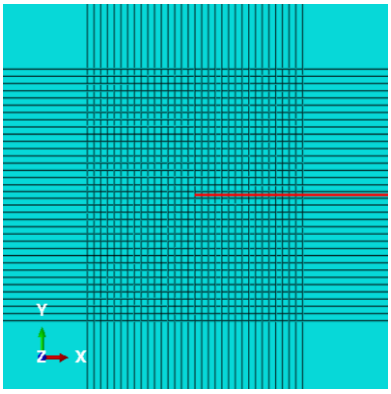

(b)

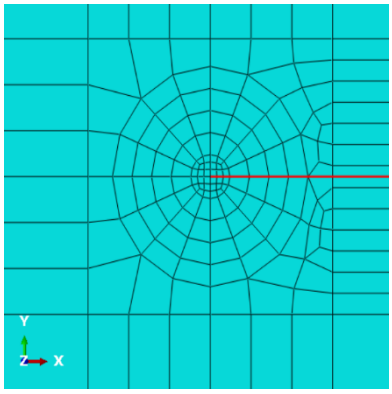

(c)

Figure 3-12: (a) Overall mesh design in the CT specimen using XFEM method, (b) Mesh type #1 and element type used in the crack tip zone (red circle in (a)), and (c) Mesh type #2 and element type used in the crack tip zone (red circle in (a))). Note: Red lines in (b) and (c) is crack

(b) Results and Discussion

To get converged SIF values first a mesh size convergence study is performed, which is one of very important factor that helps in selecting appropriate mesh size, which in turn increases efficiency of a finite element model. SIF values estimated using conventional FEM with wedge elements, as shown in Figure 3-11 (b), is used as the base model since it has been reported to produce reliable results for various crack geometries in different structures [111, 112]. The mesh fineness increases from #1 to #4 by a factor of two. For example, number of elements along

thickness and around the crack tip are 4 and 16 respectively in model with mesh size #1 and those in model with mesh size #2 are 8 and 32 respectively.

Ideally, the contour integral around the crack tip should be path independent but due to numerical approximations, they are not. However, extraction of SIF values is also of concern. As such, the sensitivity of number of contours is firstly analyzed, considering mesh level #3, as this mesh level provides sufficient accuracy as is explained later. Figure 3-13 (a) and (b) shows the values of SIF at the surface and mid-thickness of the CT specimen respectively. It shows different number of contour integral (solid lines with dot marking) requested around the crack tip and the average values of SIF (dashed lines) after ignoring the first two contours as per recommendation in [60] for the case with a/W= 0.4. For e.g. red solid line with dot marking represents SIF values obtained from a model where total five contour integrals were requested, and each dot corresponds to SIF value from that contour number. First two contours are ignored due to numerical issues which gives unrealistic values of SIF. The average SIF values for different number of contours are within ±1% of each other. Similar plot for different values of a/W can be found in ANNEX-A.

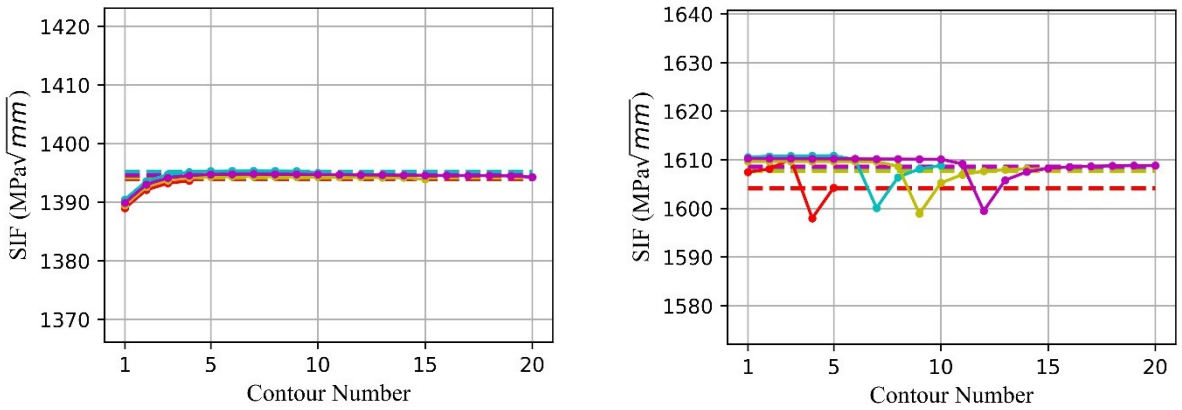

(a) (b)

Figure 3-13: Contour integral values around the crack tip in CT specimen for a/W= 0.4, requesting different number of contours in Abaqus® (a) at the surface, and (b) at the mid thickness

In Figure 3-13, the average values of coefficient of variation (CV) at surface and mid-thickness of CT specimen are 0.266 % and 0.220 % respectively. CV is the ratio of standard deviation to the mean. Here, CV is calculated based on the standard deviation and mean value of SIF from each

model with different number of contours requested i.e. 5, 10, 15, and 20. Therefore, in order to get a reliable estimate of SIF, average value of at least five number of contours after ignoring first two contours i.e. remaining three should be adequate. Requesting more number of contour integrals can be computationally expensive. Hence, in all of the models five contours are requested and extracted from output file (.odb) using a post processing Python [113] script. Also, mesh size #3 is used to analyze the sensitivity of number of contours, as this mesh size provides a trade-off between accuracy and computational expenses which is explained further in the following sections.

Figure 3-14 shows the SIF values along the thickness of the CT specimen with a/W= 0.4 when estimated using conventional FEM with wedge elements of different mesh sizes. It also contains SIF values calculated based on Eq. (3–4), which is based on two dimensional plane strain assumption and has a constant value throughout the thickness [114]. Similar plots for different values of a/W can be found in ANNEX-A.

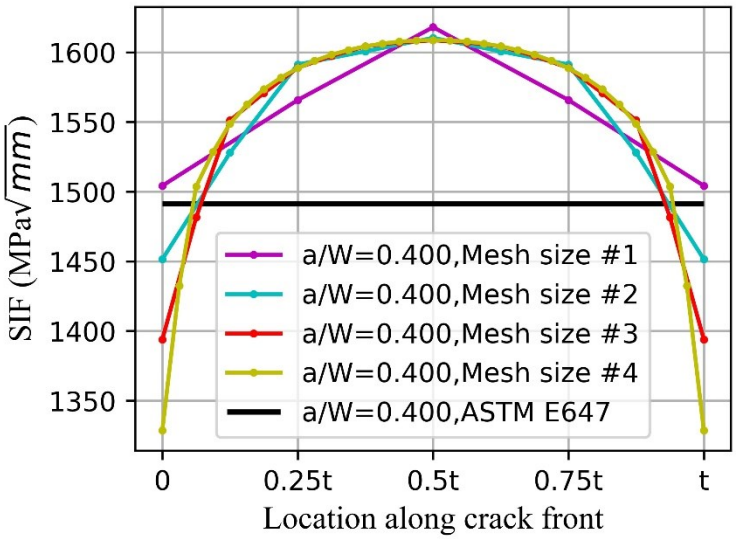

Figure 3-14: SIF values along thickness of the CT specimen using conventional FEM with wedge elements for a/W= 0.4

Figure 3-15 shows the values of SIF at the surface, finite distance inside the surface and mid-thickness of the CT specimen for different values of a/W for all mesh sizes used. The values of SIF at the mid-thickness of the specimen is less sensitive to the mesh fineness but that at the surface is very sensitive to the mesh fineness. This behavior can be explained based on the computation

algorithm. At the free surface SIF is typically computed over a domain that is one element thick. Also, the theoretical value of SIF on the free surface of a three-dimensional body is zero. Therefore, with mesh refinement the value will continually decrease [46]. The theoretical value of SIF at the surface is of little practical importance because crack propagation is governed by the SIF (crack driving force) over a finite distance inside the surface [46]. Here, the finite distance inside the surface is 0.258 mm which is the finite element node location immediately inside the surface element node in the model with mesh size #4, having 32 number of elements along the thickness of the CT specimen and is the finest mesh used here. The values of SIF at the finite distance inside the surface for mesh size #1, #2 and #3 are calculated using linear interpolation method.

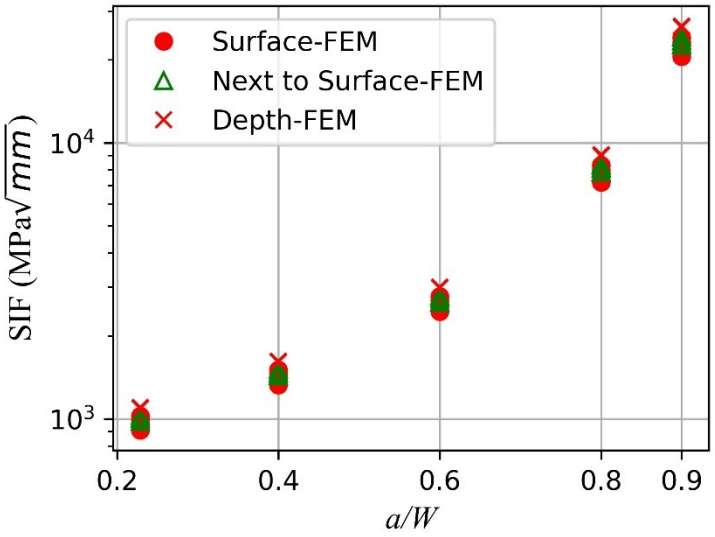

Figure 3-15: SIF values at the surface, finite distance inside the surface and mid-thickness of the CT specimen for different mesh sizes for values of *a/W*

The coefficient of variation (CV) for average values of SIF at the surface, finite distance inside the surface and mid-thickness of the CT specimen calculated using different mesh sizes as mentioned above are 4.994 %, 2.369 %, and 0.277 % respectively. The wedge element size using mesh size #3 around the crack tip, i.e. the first contour region, has radius of 0.125 mm and 0.258 mm thick; based on number of elements around the crack tip the remaining dimension can be calculated. Here, the mesh seeding around the area of interest in the models are done based on number of elements. Also, the radius of contour region increases by 0.125 mm for example the radius of fifth

contour region is 0.625 mm. As it can be observed, mesh size #3 can provide a reliable estimate of SIF values for different values of *a/W*. Therefore, the results from mesh size #3 is used as the base results for making comparison with the results obtained using various meshing strategies and sensitivity of the number of contour integral request as mentioned above.

The SIF values estimated using the base model as described in previous section are compared with the SIF values estimated using other meshing strategy used in FEM and XFEM models. The SIF values estimated using FEM models with meshing strategy as shown in Figure 3-11 (c) are compared directly to the results obtained using XFEM with meshing strategy as shown in Figure 3-12 (c). The enrichment radius or singularity calculation radius in XFEM models equal to at least one element length ahead of the crack tip produces stable and reliable results. The enrichment radius for the mesh size #3 is 0.125 mm. First, in order to check the robustness of XFEM, SIF values are estimated using XFEM and shown in Figure 3-16, with a general mesh strategy as shown in Figure 3-12 (b). Fineness of mesh is similar to that used for conventional FEM as mentioned previously. The values of SIF at depth is more sensitive but that at surface shows similar trend to that observed with conventional FEM. The mesh size of elements around the crack tip used in this study is in the range of 0.25-1.15% of the CT specimen thickness, mesh size #3 corresponds to 0.25% of thickness.

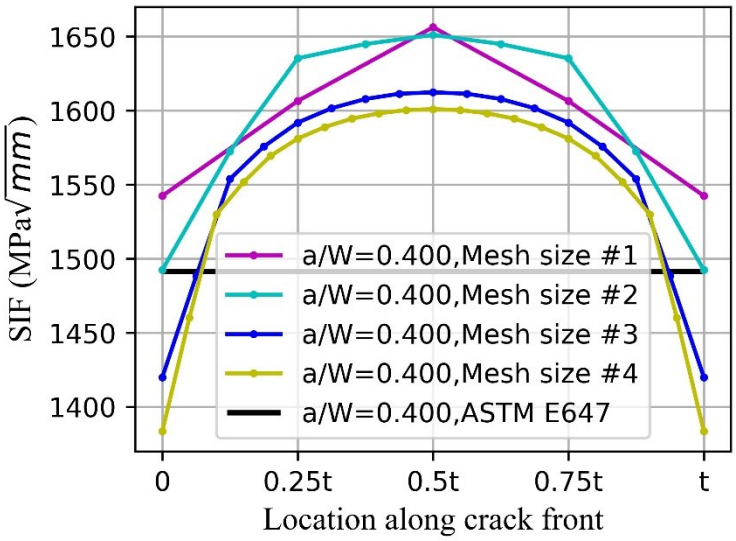

Figure 3-16: SIF values along thickness of the CT specimen using XFEM with general meshing strategy for *a/W*= 0.4

Finally, a comparison between different meshing strategies used in both conventional FEM and XFEM with the mesh size #3 is done, see Figure 3-17. FEM-Wed, FEM-Hex, XFEM-Gen and XFEM-Hex in Figure 3-17 corresponds to meshing strategies shown in Figure 3-11 (b), Figure 3-11 (c), Figure 3-12 (b) and Figure 3-12 (c) respectively. The SIF values estimated using different meshing strategies for different values of *a/W* at surface, finite distance inside the surface and mid-thickness of the CT specimen is shown in Figure 3-18. The values of SIF estimated using different meshing strategies are compared with the finest base model, i.e. focused mesh strategy as shown in Figure 3-11 (b). The values are within +3% of that estimated using focused mesh strategy. Hence, if a general meshing strategy is used in XFEM sufficiently fine mesh around the crack tip is required to get a reliable estimate of SIF. Mesh convergence result plots for different values of *a/W* using general meshing strategy in XFEM can be found in the ANNEX-A.

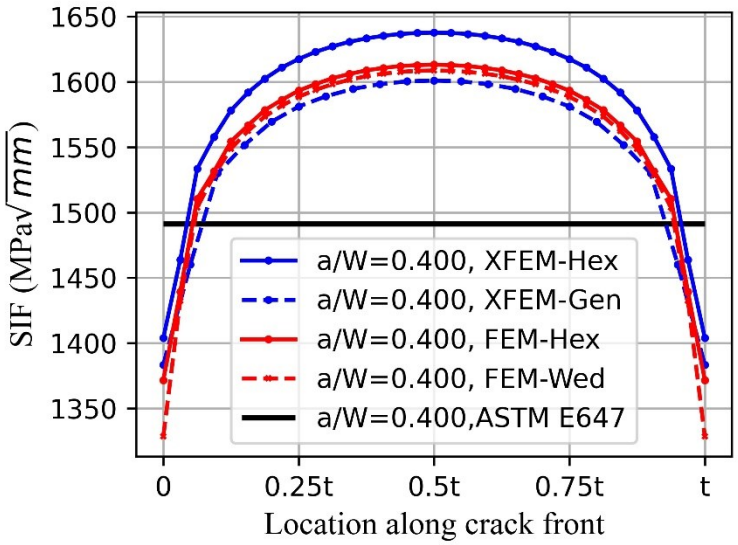

Figure 3-17: SIF values along thickness of the CT using different meshing strategies in XFEM and FEM models for *a/W*= 0.4

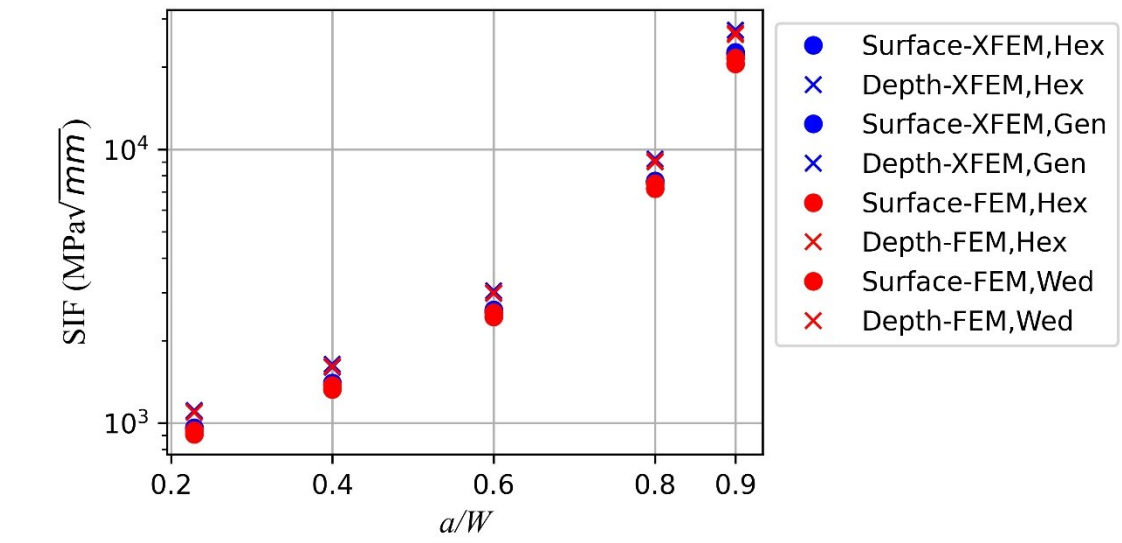

(a)

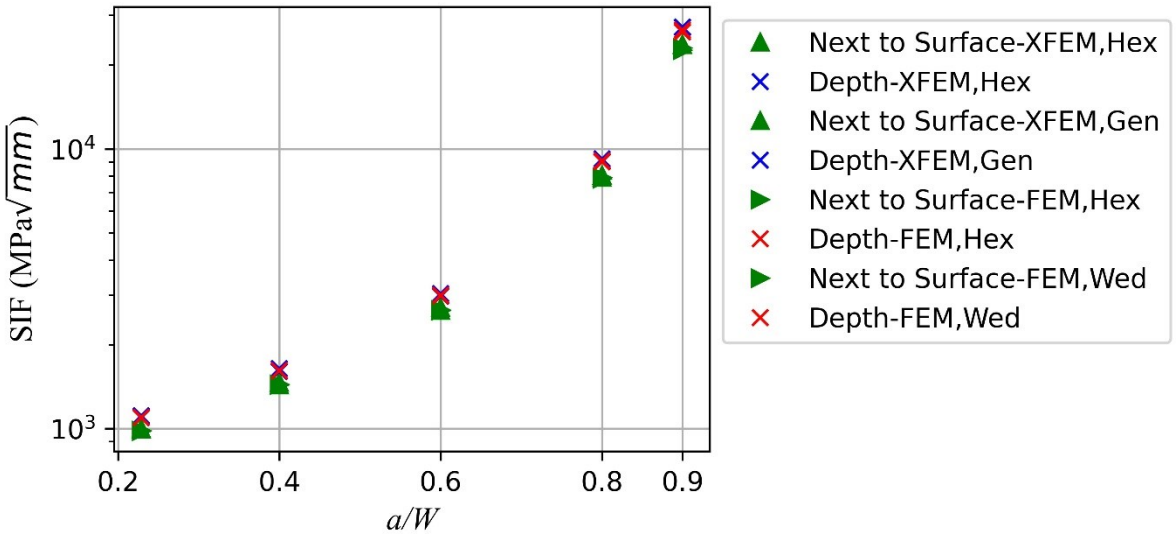

(b)

Figure 3-18: SIF values for different values of *a/W* (a) surface and mid-thickness of the CT specimen, and (b) finite distance inside the surface and mid-thickness of the CT specimen

(2) Pipeline Section

In this section, a pressurized pipeline section with semi-elliptical surface crack along longitudinal direction studied in [111] is used for validation of both FEM and XFEM models. The Young's modulus of elasticity (E) and Poisson's ratio (v) are 204500 MPa and 0.3 respectively. Figure 3-19 shows the geometrical features of the pipeline section (a hollow cylinder) and longitudinal crack. The wall thickness (t), internal radius (R_i) and length (L) are 19.00 mm, 1139.75 mm and 6000.00

mm respectively. The pipeline section has a longitudinal crack with semi-elliptical crack front having depth *a* and length *2c*. Various combination of crack geometries with constant *a/c*=0.5 and varying *a/t* is used in this study similar to that in [111] for estimation of SIF when subjected to monotonic internal pressure of 3.5 MPa.

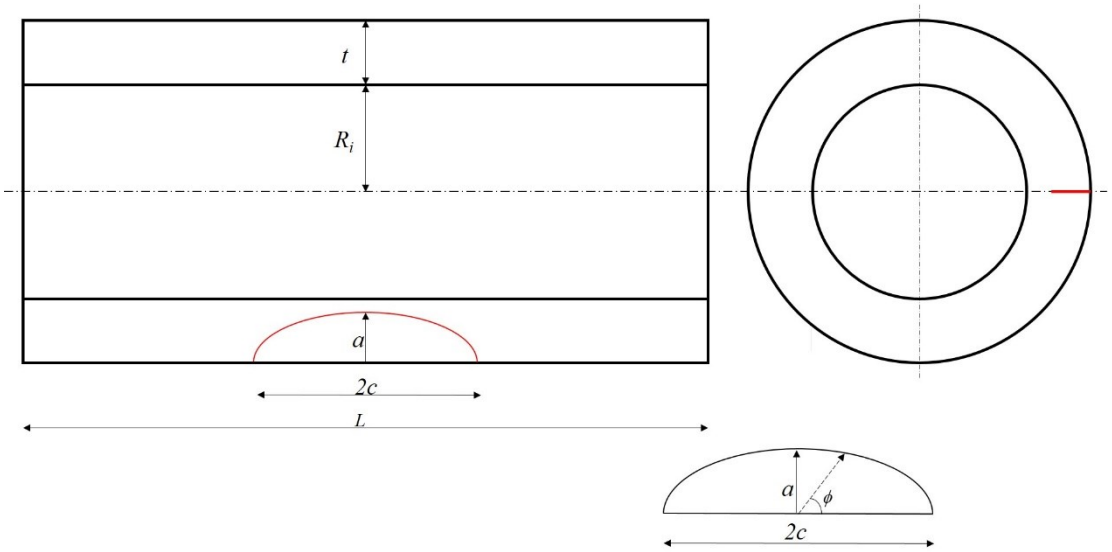

Figure 3-19: Geometric details of the hollow cylinder with longitudinal crack in the outer surface

(a) Modeling Strategy

Both conventional FEM and XFEM models are developed for the pipeline section (hollow cyclinder) using Abaqus®. Figure 3-20 shows a typical 3D finite element model of the pipeline section. Either ends of the pipeline section are pinned ($u_x = u_y = u_z = 0$) . A monotonically increasing maximum pressure load of 3.5 MPa is applied on the internal surface of the pipeline section. In order to reduce complexity in meshing, the pipeline section is divided into three sub parts and tied together with surface based constraint tie as shown in Figure 3-21. Similar technique has been successfully used in [115]. The three sub-parts are viz. Main pipe body, transition pipe body and crack location part as shown in Figure 3-21 (b), (c), and (d) respectively. The value of angle subtended at the center $\alpha = 1.875°$. The length of subpart transition pipe body is three times the length of crack i.e. $6c$ and that of the main crack location part is 1.5 times the length of crack i.e. $3c$. The length of pipeline section in the models are taken to be 1000 mm, as per [111, 112] $L/2c \geq 10$ should be enough to neglect the length effect on the SIF.

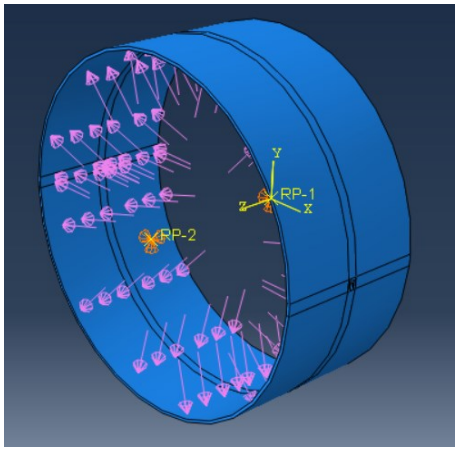

Figure 3-20: 3D finite element model with boundary conditions and load in the hollow cylinder

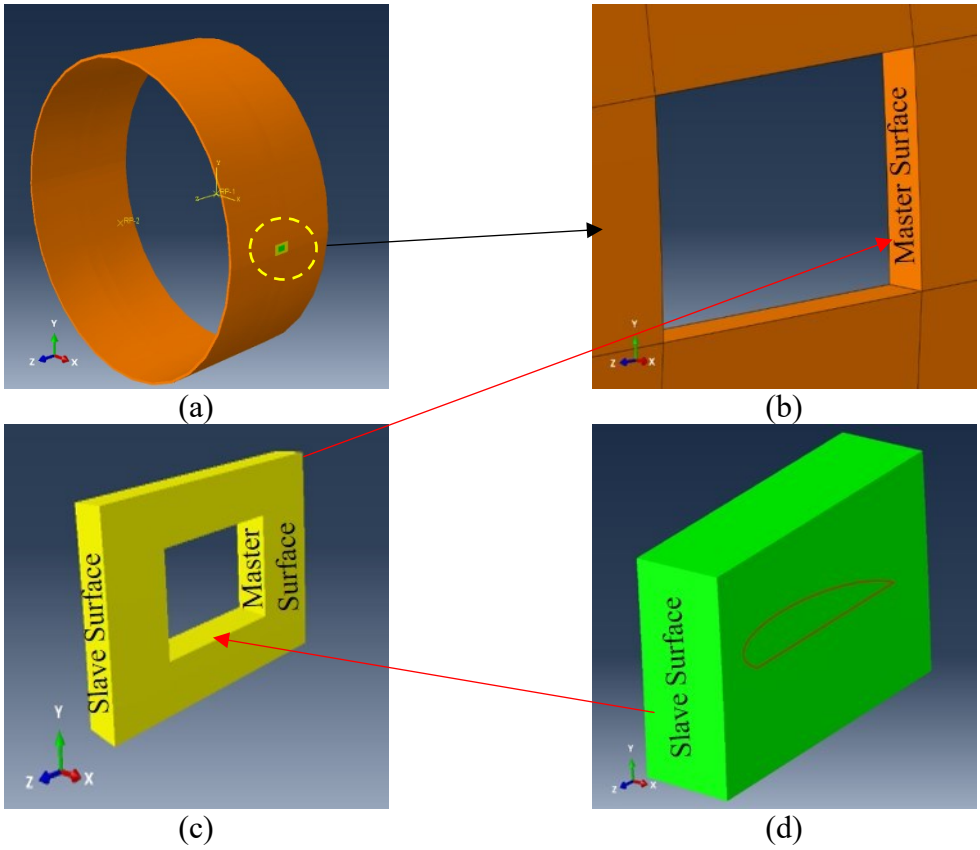

(a) (b)

(c) (d)

Figure 3-21: 3D parts created in the models and tied together with surface based tie constraints (red arrow shows location of each sub-part being constraint to the other) (a) Main pipe body (Coarse Mesh), (b) zoomed in view of main pipe body at the constraint location, and (c) Transition pipe body (Medium size mesh), and (d) Crack location part with the crack (finest mesh size)

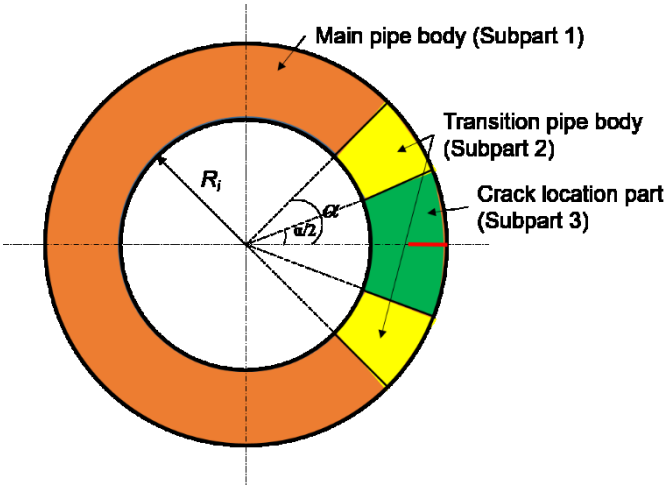

Figure 3-22. Typical section of 3D models of the pipeline section showing geometrical features of each sub-parts

(b) Mesh Design for FEM and XFEM Models

A very similar meshing strategy as discussed in previous section 0 for CT specimen is used for the pipeline section as well. Figure 3-23 shows the detail of the meshing strategy used in the pipeline section. Spider web type mesh having wedge elements with reduced integration (C3D6R) as shown in Figure 3-23 (e) is used in the first contour region. In all other region hexahedral elements with reduced integration (C3D8R) is used. A spider web type mesh with regular hexahedral elements with reduced integration (C3D8R) is also used in the entire model as shown in Figure 3-23 (f) in order to make comparison with the results obtained using XFEM.

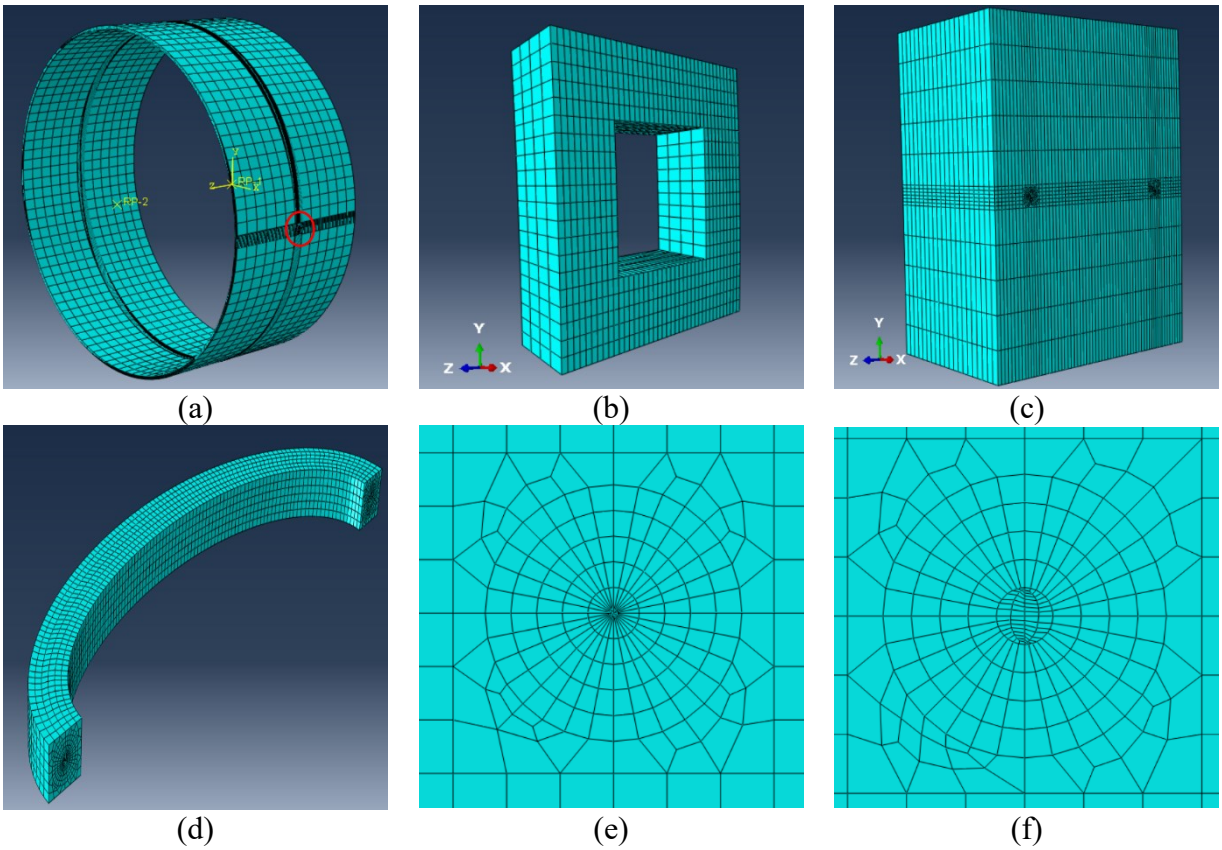

Figure 3-23: Typical meshing strategy used in FEM models (a) overall meshing in the pipe, (b) mesh in the transition pipe body part, (c) mesh in the crack location part, (d) mesh along the semi-elliptical crack front, (e) focused mesh with wedge type element in FEM model, and (f) focused mesh with hexahedral type element used in FEM and XFEM models

(c) Results and Discussion

A mesh convergence study of FEM models with six out of twelve crack configurations with different values of *a/t* and constant value of *a/c*=0.5 similar to that in [111] is carried out in this study. Table 3-5 summarizes different crack geometry configurations used in this study for FEM and XFEM model verification. Four different mesh sizes, mesh size #1 being coarsest and #4 being finest mesh size. The level of fineness around the crack tip and along the crack front increases by a factor of two from mesh size #1 to mesh size #3. For example, element size along the crack front in mesh size#1 is 1 mm and that in mesh size #3 is 0.25 mm and element size around the crack tip in mesh size #1 is 1 mm and that in mesh size #3 is 0.25 mm. The element size along the crack

front is same in mesh size #3 and mesh size #4 but that around the crack tip in mesh size #4 is 0.125 mm. This change in fineness is done to save in computational expenses.

Table 3-5 Crack geometry used for FEM and XFEM model verification

Crack #	***a*** (mm)	***c*** (mm)	***a*/t**
1	5	10	0.263
2	11	22	0.579
3	15.8	31.6	0.832
4	16.5	33	0.868
5	17.18	34.36	0.904
6	17.3	34.6	0.911

Figure 3-24 shows SIF values along the crack front calculated from FEM model with focused mesh as shown in Figure 3-23 (e) for *a/t*=0.868. Similar plot for different values of *a/t* can be found in ANNEX-A. Figure 3-25 shows the values of SIF at the surface, finite distance inside the surface and at the depth of the pipeline section for different values of *a/t*. A very similar kind of trend in the values of SIF at surface and depth can be observed as mentioned in previous section (b) for CT specimen for similar reasons. The value of SIF at the surface is of little practical importance because crack propagation is governed by the SIF (crack driving force) over a finite distance inside the surface as mentioned in section (b) [46]. SIF values for mesh size #1 and mesh size #2 at finite distance under the surface i.e. $\phi = 0.523^{\circ}$ are calculated by interpolation technique, as the number of elements along the crack front are less than that in mesh size #3 and #4. The mean value of CV of average values of SIF at the surface, finite distance under the surface and depth of the pipeline section using different mesh sizes mentioned above are 1.566 %, 0.873 %, and 0.339 % respectively. The CV of SIF at different location along the crack front shows a converged behavior. As it can be observed in Figure 3-24, that SIF estimated using model with mesh size #3 can provide a reliable estimate of SIF. Hence, FEM model with mesh size #3 is used as base model for comparison with other meshing strategies.

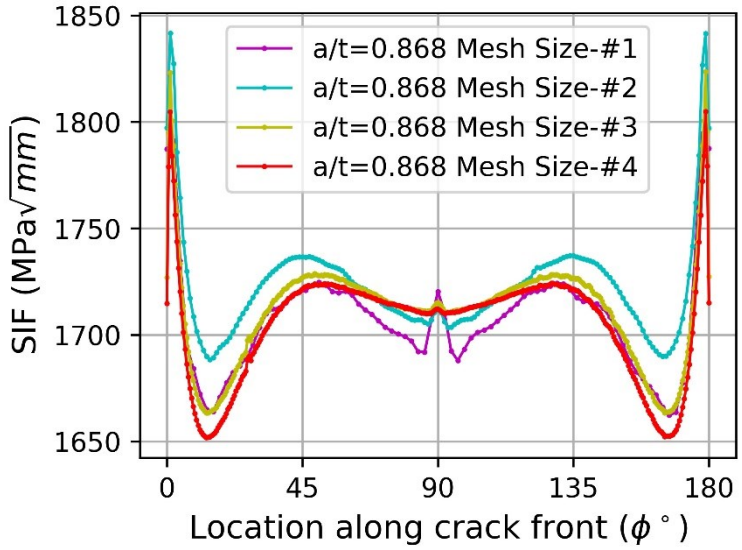

Figure 3-24: SIF values along crack front calculated using FEM with focused mesh having wedge elements for *a/t*=0.868

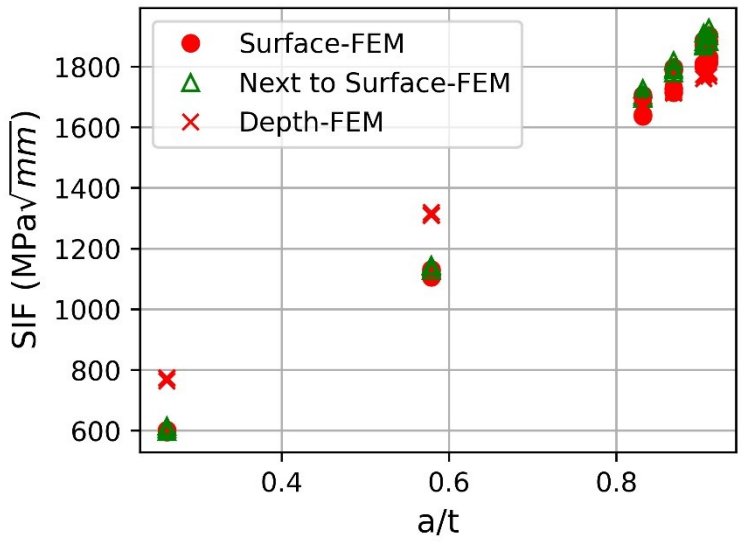

Figure 3-25: SIF values at the surface, finite distance inside the surface depth of the pipeline section for different values of *a/t*

The SIF values estimated using the base model as described in previous section are compared with the SIF values estimated using other meshing strategy used in FEM and XFEM models. Figure 3-26 shows comparison of SIF values using different meshing strategies in FEM and XFEM

models. The SIF values estimated using FEM models shows a smooth behavior along the crack front but those using XFEM shows an oscillating behavior especially towards the depth. This behavior can be explained based on the difference in the technique used for modeling cracks in FEM and XFEM. In FEM, cracks are modeled by confirming to the mesh i.e. mesh actually represent the crack. Whereas, in XFEM cracks are modeled independent of the mesh and for a curved crack front the nodes might not necessarily coincide with the crack geometry and due to interpolation approximations of the values between the nodes such oscillating behavior might be observed. However, the trend of values along the crack front are very similar and are in reasonable agreement using different mesh strategies in FEM and XFEM

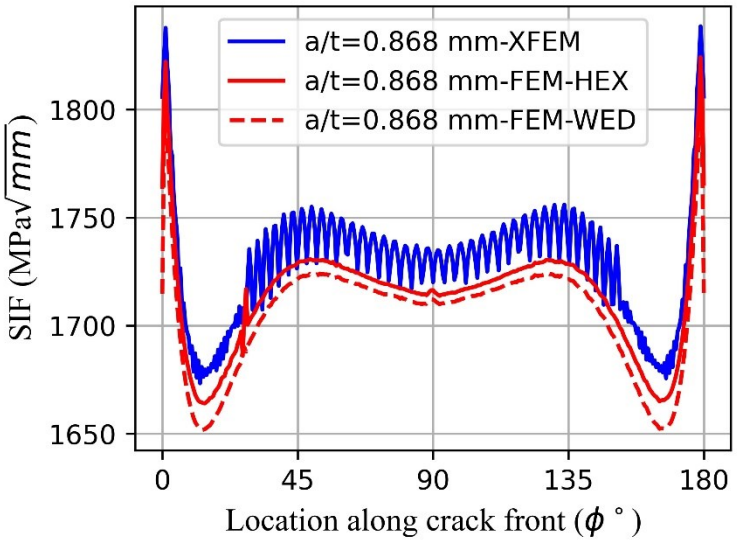

Figure 3-26: SIF values along crack front calculated using different meshing strategies in XFEM and FEM models for *a/t*=0.868

Figure 3-27 shows the values of SIF at the surface, finite distance inside the surface and at the depth of the pipeline section for different values of *a/t*. The values of SIF estimated using various meshing strategy in FEM and XFEM are within +3% of that estimated using focused mesh strategy except for surface values using XFEM where it is just below +5.5%. As stated, earlier the values of SIF at the surface are of less practical significance. Hence, SIF values estimated using appropriate mesh size and technique in both XFEM and FEM are reliable.

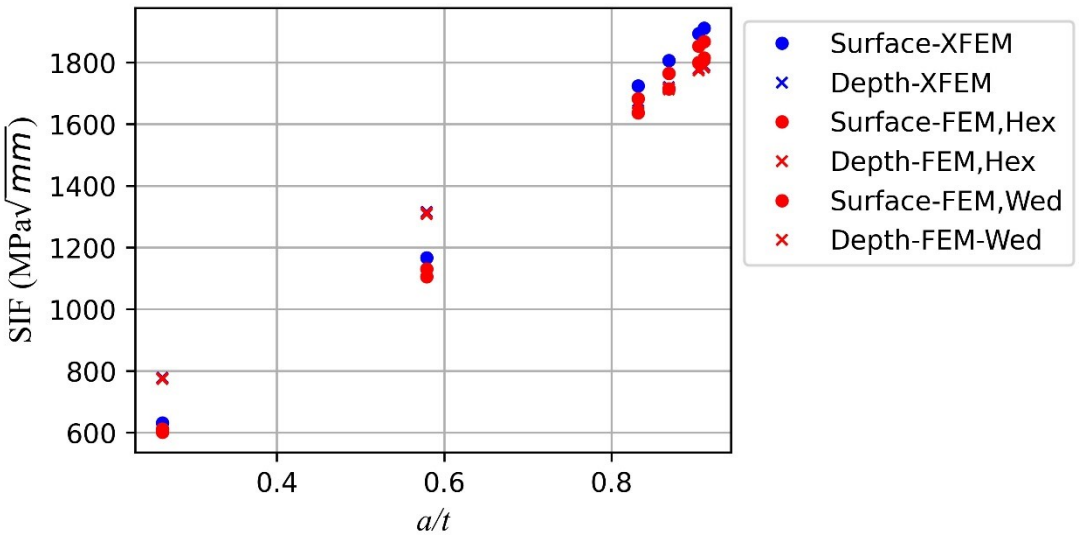

(a)

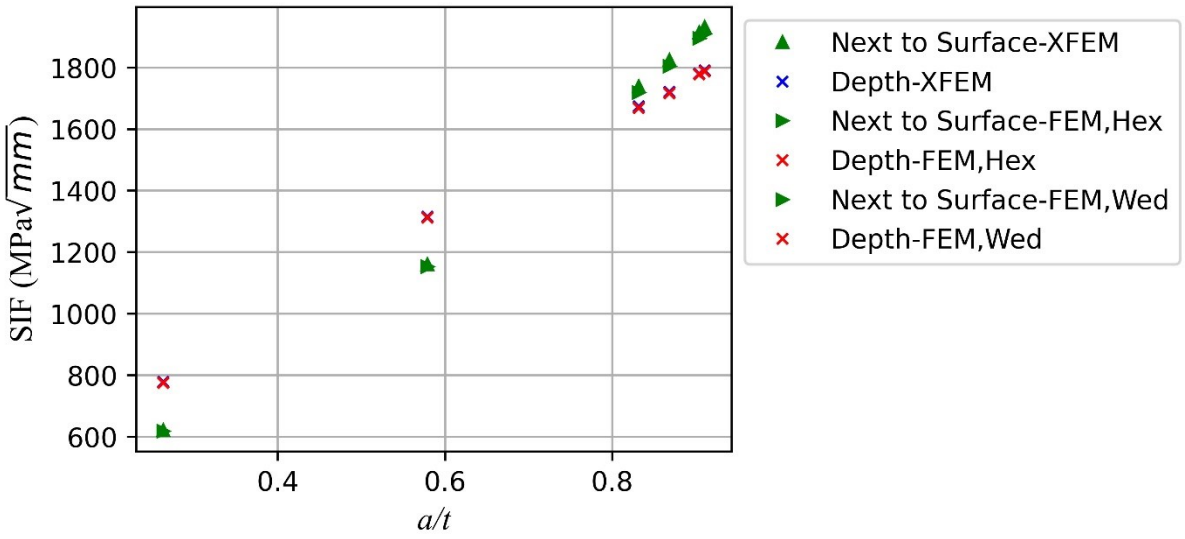

(b)

Figure 3-27: SIF values for different values of *a/t* (a) surface and depth of the pipeline section, and (b) finite distance inside the surface and depth of the pipeline section

3.4.1.3 Comparison of SIF estimation using different methods

In previous section, meshing strategies and other factors like number of contour request to get reliable estimate of SIF values for straight crack front and semi-elliptical crack front were discussed in detail. Based upon the strategies discussed above SIF values for three different

pipeline sections is estimated to further validate numerical modelling procedure. Pipeline and Hazardous Materials Safety Administration (PHMSA) is a regulatory based in United States of America that regulates safe transportation of energy to the public. Any incident/accidents related transportation of energy are required to be reported and such reports are made available to public. Using such publically available data, three pipeline sections reported to have incident related to fatigue crack in pipe body were selected and SIF values for these pipelines were calculated using FEM, XFEM and API 579 model given by Eq. (3–3). Table 3-6 lists various information related to three pipelines from PHMSA database reported to have incident related to fatigue crack in pipe body. It lists wall thickness (WT or t), internal radius (R_i), t/R_i, operating pressure at the time of incident (OP), maximum operating pressure (MOP) and specified minimum yield strength (SMYS).

Table 3-6 Pipelines reported to have incident related to fatigue crack in pipe body in PHMSA database

S.N.	**Operator Name**	**WT, t** (mm)	R_i (mm)	t/R_i	**OP** (MPa)	**MOP** (MPa)	**SMYS** (MPa)
1	Phillips 66 Pipeline llc	6.350	146.05	0.043	9.570	13.000	413.685
2	West Texas Gulf Pipeline Co.	7.925	322.275	0.025	3.089	5.500	358.527
3	Colonial Pipeline Co	7.137	450.063	0.016	2.179	4.000	358.527

(1) Results and Discussion

Both FEM and XFEM models with modeling strategies discussed in section 3.4.1.2 were built for the three pipelines #1- #3 with various crack geometries listed in Table 3-7 with respective t/R_i and subjected to respective MOPs. For each pipeline, 25 (5 a/c × 5 a/t) data are produced. The values of a/c and a/t are selected such that the results could be compared to that calculated using API 579 model.

Table 3-7 Pipe and crack geometry configuration

t/R_i	a/c	a/t
0.016 (PHILLIPS)	0.125, 0.25, 0.5, 1, 2	0.2, 0.4, 0.6, 0.8, 0.9
0.025 (WEST)		
0.043 (COLONIAL)		

A comparison between SIF values at the surface and depth using FEM, XFEM and API 579 models for three pipeline section for $a/c = 0.5$ is shown in Figure 3-28. A similar plot for different values of a/c for each pipeline section can be found in ANNEX-A. Note that, the SIF values corresponds to values at finite depth from the surface of the pipeline section for $\phi = 1.7^{\circ}$. The results obtained using XFEM are in good agreement with FEM and API 579 models. This can be explained based on the fact that API 579 models were generated by fitting 6th –order polynomial to the results obtained using FEM analysis having 20 node brick elements [110] with meshing strategy same as in this study. Additionally, the 6th- order polynomial was fitted to the FEM results excluding those at the free surface and the values of SIF at the surface are estimated by extrapolating the polynomial fit. The meshing strategy used in API 579 model building is as shown in Figure 3-8. Table 3-8 summarizes average values of difference between SIF values calculated using XFEM vs. FEM and API 579 for different values of a/c and a/t listed above given by Eq. (3–5):

$$\delta = \frac{SIF_{XFEM} - SIF_{FEM/API}}{SIF_{FEM/API}} \text{x}100\% \qquad (3–5)$$

where, SIF_{XFEM} is SIF value obtained using XFEM and $SIF_{FEM/API}$ is SIF value obtained using FEM and API 579 model.

The values of SIF at the surface estimated using XFEM are in average higher up-to 3.87% than FEM and those at the depth are within ±1.328%. The results from XFEM when compared to the API 579 model are overall less conservative at depth and surface. The values of SIF for $a/t > 0.8$ was linearly extrapolated for API 579 model for comparison.

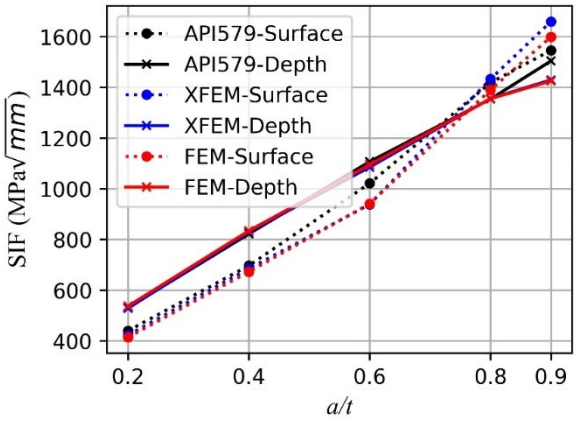

(a)

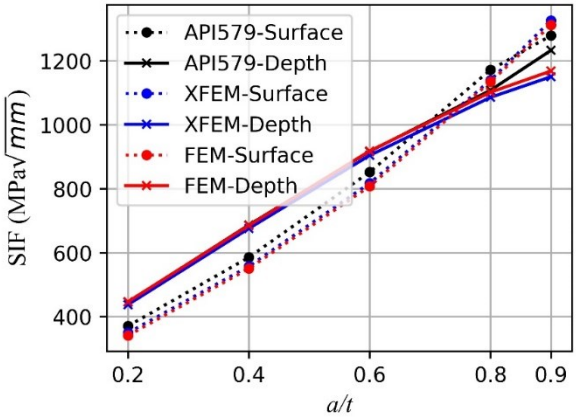

(b)

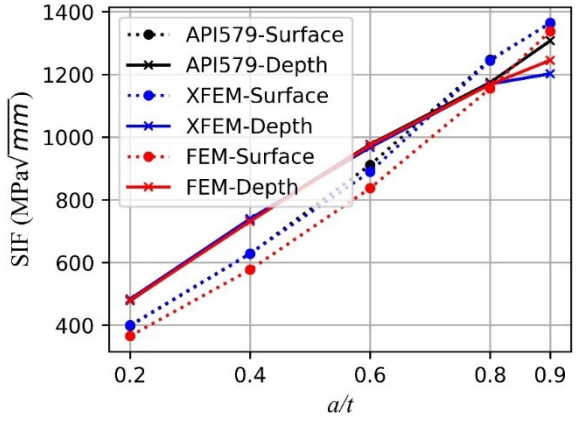

(c)

Figure 3-28: SIF values at finite depth from surface and depth ($\phi = 90^{\circ}$) for *a/c*=0.5 (a) Pipeline #1, (b) Pipeline #2, and (c) Pipeline #3

Table 3-8 Comparison between SIF values calculated using XFEM vs. FEM and API 579

Pipeline	XFEM compared to FEM		XFEM compared to API 579	
	Surface (%)	**Depth** (%)	**Surface** (%)	**Depth** (%)
Phillips 66 Pipeline LLC	3.870	0.288	2.014	-3.951
West Texas Gulf Pipeline Co	2.288	-0.399	-0.147	-3.532
Colonial Pipeline Co	3.375	-1.328	-1.174	-3.562

3.4.2 Implementation of Indirect Method of FCG Modeling

Comprehensive details on various methods including XFEM for estimation of one of the main parameters required for fatigue crack propagation, SIF, was presented in previous section. In the following section SIF calculated using verified XFEM modelling procedure is coupled with Paris' law as explained in section 3.4 to demonstrate implementation of indirect method of FCG modeling using CT specimen and pipeline section are presented as case studies.

3.4.2.1 Demonstration of Indirect FCG Modeling in CT Specimen

In this section, the CT specimen as described in section (1) is used to demonstrate the indirect FCG modeling. A 3D XFEM model with the meshing and modeling strategy discussed in the section (1) is used for estimation of SIF at the surface and mid thickness of the CT specimen.

Figure 3-29 shows the FCG generated using the indirect method as explained in the previous section. The experimental result data is taken from Silva et al. (2011). The experimental result is for a through crack, i.e. the entire cross section at particular crack depth is cracked. The FCG generated using indirect method is based on the SIF value at particular point of interest, like mid-thickness and surface. Due to high tri-axiality at the mid thickness, the value of SIF is high relative to the surface, also verified in the previous section. Hence, an average of the FCG estimated at the surface, mid thickness provides a more realistic FCG curve, and matches closely to the experimental results.

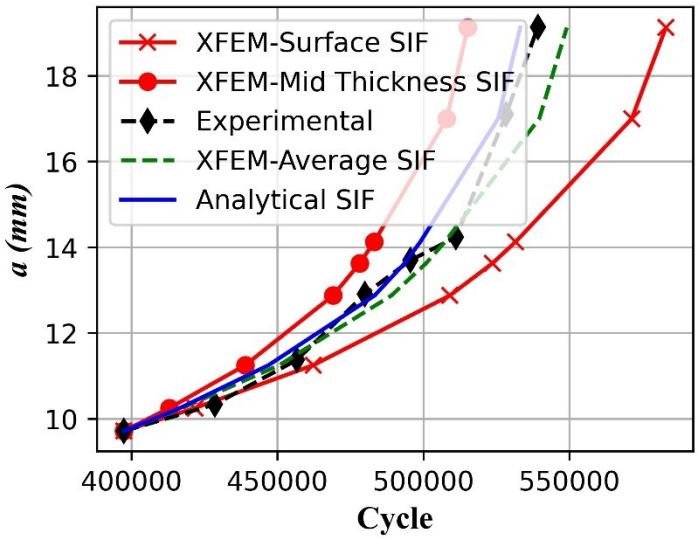

Figure 3-29: Fatigue crack growth curve of CT specimen obtained using In-direct method

3.4.2.2 Demonstration of Indirect FCG Modeling in Pipeline Section

(1) Model Description and Details

Tiku et al. (2020) proposed the fatigue crack growth equation parameters *C* and *m*. The values were based on the pipeline material fatigue crack growth database developed using 185 fatigue crack growth rate tests on 45 pipeline materials ranging in grade from X46 to X70 and in vintage from 1937 to 2014 [45]. The FCG data was generated using proposed *C* and *m* values coupled with API 579 model for SIF estimation. This was compared against FCG data obtained various methods like BS 7910, API 579, and experiments. In this section one of the pipes studied in Tiku et al. (2020) whose FCG curve, using proposed values of *C* and *m*, is presented with all the necessary details is selected to demonstrate and compare the indirect FCG modeling procedure.

X46 grade pipeline with geometric and material properties listed in Table 3-9 and Table 3-10. Initial cracks having semi elliptical crack front with crack geometries shown in Table 3-9 are machined. The pipelines are subjected to maximum internal pressure corresponding to 55% of SMYS and minimum internal pressure corresponding to 5% of SMYS, i.e. stress ratio is 0.1. The values of internal pressure are not mentioned explicitly. However, the maximum internal pressure is estimated to be 5.5 MPa and minimum internal pressure is estimated to be 0.55 MPa based upon

the provided data. Length of the pipe is adopted to be 4064 mm, making it greater than 10 times the outer diameter, on order to make the effect of end conditions negligible [116]. Pinned boundary condition is applied at both ends $(u_x = u_y = u_z = 0)$. Similar to Tiku et al. (2020) [45] the crack growth along axial direction is assumed to be negligible and kept constant.

XFEM models are created using the strategies discussed in section (2). Figure 3-30 shows a typical XFEM model of the pipeline for estimation of SIF and FCG. The general meshing strategy is used in the main crack domain region with an objective to check the performance of the XFEM with non-confirming mesh for crack modeling. The mesh size in the crack domain is approximately 1 mm × 0.2 mm × 1 mm, along the circumferential, thickness and longitudinal direction respectively. The crack depth used in the XFEM model ranges from 2.667 mm to 5.397 mm, and crack length is held constant at 250 mm.

Table 3-9 Geometric details of pipe and crack

Pipe ID	**Outer Diameter, OD** (mm)	**Wall Thickness, WT** (mm)	**Initial Crack Depth, a_0** (mm)	**Initial Crack Length, $2c_0$** (mm)
A	406.4	6.35	40 % of WT = 2.54	250

Table 3-10 Material properties

Grade	**Specified Minimum Yield Strength , SMYS** (MPa)	**C** $(mm/cycle)/(MPa.\sqrt{mm})^{m}$	**m**
X46	317.15	3.03E-14	3.24

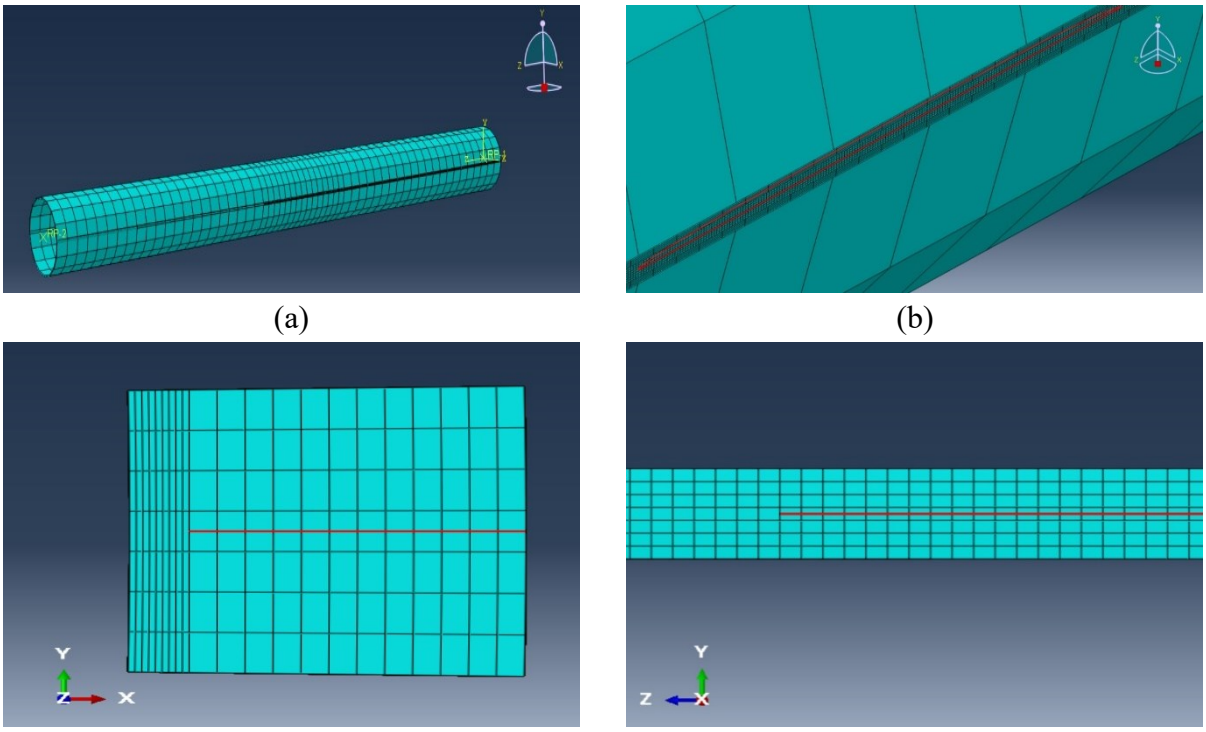

Figure 3-30: Typical XFEM model of Pipeline section for FCG estimation using indirect method (a) overall view, and (b) overall close up view at the crack location, and (c) mesh view along the pipe wall thickness, and (d) mesh view along the axial direction. (Highlighted red geometry is the crack)

(2) Result and Discussion

FCG curve generated using indirect method for the pipeline section with the initial crack geometry, crack depth of 40 % of WT i.e. 2.54 mm, is shown in Figure 3-31. However, the data FCG data available in [45] is reported starting from slightly higher value i.e. 2.677 mm which might be due to experimental measurement condition. This value of crack depth was adopted for XFEM models. The results obtained using indirect method and that from Tiku et al. (2020) [45] are in good agreement with each other. In Tiku et al. (2020) [45] the FCG was obtained using fatigue parameters from experiment and SIF was estimated using API 579 model. The factors like mesh size and discrepancies in the internal pressure data could be the reason for minor differences. However, more experimental data is required for further validation of the method. It is worth mentioning that reasonable results are obtained for both straight crack front as shown in section

3.4.2.1 for CT specimen and curved crack front as demonstrated is this section. The promising results hints towards the potential of the indirect method to be used as FCG estimation tool.

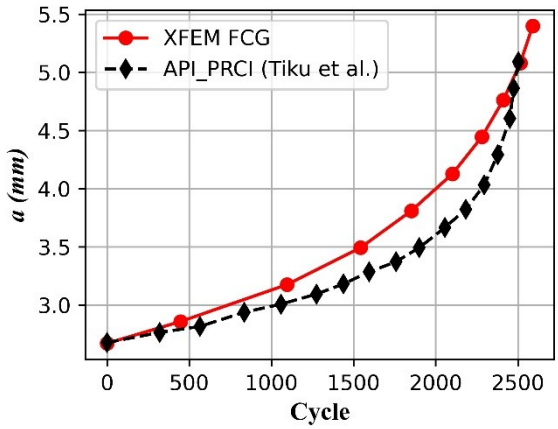

Figure 3-31: Fatigue crack growth curve of pipeline section with initial crack obtained using indirect method

3.5 Summary

In this chapter, comprehensive details about numerical methods for quasi-static and fatigue crack propagation in steel pipelines is presented. Influence of damage modeling properties used in quasi-static crack propagation analysis for estimation of burst pressure using XFEM implemented in Abaqus® is discussed. Various factors like meshing strategy, mesh size, number of contours, and enrichment radius for estimation of SIF is dealt in detail using case studies on CT specimen and pipeline section. An alternate method i.e. indirect method, for FCG estimation from SIF estimated using XFEM and coupled with discrete form of Paris' law is discussed.

Calibration of damage modeling properties with full scale tests is recommended to accurately predict the burst pressure of pipe using quasi-static analysis. This is a field of investigation and many researcher are putting their efforts on it. FEM requires a crack confirming mesh and wedge type of elements for better accuracy. Mesh size of 0.125 mm – 0.25 mm along the crack front and around the crack tip produces reliable values of SIF. In XFEM crack can be modeled independent of the crack geometry with a general meshing strategy, but a mesh structure confirming to the shape of crack geometry provides better accuracy. Mesh size of 0.125 mm – 0.25 mm produces good results when using focused type mesh. When general meshing strategy is used the mesh size

of 0.02 mm around the crack tip is required, which is about one fifth of that required when using focused type meshing strategy. Mesh size 0.125 mm – 0.25 mm along crack front is sufficient. Five number of contours around the crack tip and calculating the average after ignoring first two contours provides a reliable estimate. The appropriate enrichment radius around the crack tip is estimated to be at least one element size ahead of the crack tip, which is 0.125 mm in this study. The estimated SIF values compared to those from the API 579 model for different pipelines are in very good agreement, which provides further confidence in use of XFEM. The FCG estimated using indirect method produced results with good agreement in other published experimental work.

CHAPTER 4: SURROGATE MODELING FOR FATIGUE CRACK DRIVING PARAMETER ESTIMATION

4.1 Introduction

In this chapter, a surrogate model for reliable, fast and computationally less expensive way of estimating SIF is presented. Data-points for building surrogate model will be generated from API 579 model, as it has been verified using FEM and XFEM model in previous section and proven to provide reasonably accurate values of SIF. Furthermore, API 579 model for SIF estimation was developed based on a large set of finite element models and hence covers a wide range of pipe and crack geometry.

4.2 Motivation for Building Surrogate Model for SIF Estimation

Surrogate models are approximation models that mimic the behavior of the simulation model as closely as possible while being computationally cheap. It is constructed based on modeling the response of the simulator to a limited number of intelligently chosen data points. Surrogate models are used for estimating system response and supporting decision making in engineering processes with a focus on pointwise estimation [67].

Several surrogate models have been used in the literature to estimate the growth of cracks in offshore pipelines, including linear regression, polynomial regression, nonlinear models (e.g., Artificial neural network: ANN), kernel-based models (e.g., Gaussian Process: GP), and sparse kernel based models (e.g., Support vector machines: SVM) [117]. For onshore pipelines, which are typically thin-walled and larger diameter pipelines, polynomial regression is the most commonly used approach [46, 110]. The results of this approach are included in the commonly used industry standards such as “Fitness for service: Assessment of crack-like flaws” (API 579-1 Part 9, 2016). In a comparative study, between ANN, SVM, and GPR for estimation of SIF of pipeline with crack on the outer surface the authors concluded that all three methods provided flexible ways of model fitting over wide variety of inputs [118]. However, as mentioned earlier Gaussian Process Regression is a non-parametric, kernel-based probabilistic model to approximate the underlying relationship between input and output response instead of relying on a functional relationship. GPR is also capable of uncertainty quantification making it an attractive choice as a surrogate model.

As discussed in previous chapter in section 3.4.1.1, the API 579 model for calculating SIF due to semi-elliptical crack on the outer surface of pipe subjected to internal pressure is made utilizing the influence coefficients $G_0 - G_4$. The coefficients G_0 and G_1 are tabulated in Table 9B.13 of API 579 [10]. Nevertheless, G_2, G_3, and G_4 are calculated based on G_0 and G_1 given by equations presented there. Linear interpolation between the tabulated values are allowed but extrapolation is not. The parameters required for extracting the coefficients are t/R_i, a/c, and a/t which have 8, 7 and 5 distinct tabulated values respectively for each G_0 and G_1. Hence, the table contains 280 data points of each G_0 and G_1 i.e. 560 data points are present. Here, t/R_i is a ratio of pipe wall thickness to the internal radius, a/c is a ratio of crack depth to the half crack length, and a/t is the ratio of crack depth to the pipe wall thickness.

In order to get the SIF values at the tabulated values of parameters t/R_i, a/c, and a/t, it is straightforward. However, when SIF at intermediate values of these parameters need to be estimated, multiple linear interpolation is required based on the table and execution time increases significantly, which partly depends on the implementation. For example, loading the table data into python repeatedly can be time consuming. When performing operations like stochastic filtering as discussed in the following chapter, involving calculation of SIF for various combinations of pipe and crack geometry, load etc., the computational expense plays a vital role. Also, to automate the SIF extraction using a single model, instead of a piece-wise model consisting of multiple sub-models in API 579, a surrogate model was developed. Thus, developed surrogate model was eventually integrated with PF and Paris' law for FCG trajectory prediction in the next chapter.

4.3 Gaussian Process Regression (GPR) for SIF Estimation

4.3.1 Introduction

Gaussian Process (GP) is a collection of an infinite number of correlated random variables, any finite number of which has multivariate normal distributions. A GP is fully specified by a mean vector and covariance matrix as shown by Eq. (4–1):

$$f \sim N(\boldsymbol{\mu}_{Pr}, \boldsymbol{\Sigma}_{Pr}) \tag{4–1}$$

where, $\boldsymbol{\mu}_{Pr}$ and $\boldsymbol{\Sigma}_{Pr}$ are the prior mean vector and prior co-variance matrix of the GP f, respectively.

Gaussian Process Regression (GPR) is a non-parametric, kernel-based probabilistic model to approximate the underlying relationship between inputs and target response. Consider a training dataset with input parameters $\mathbf{x}_t$ and target response $\mathbf{y}_t$. If the prediction required is $f(\mathbf{x})$ for a given set of input parameters **x,** the conditional probability distribution of the required prediction is modeled in GPR as a Gaussian distribution, leading to a GP as shown by Eq. (4–2):

$$P(f(\mathbf{x}) \mid \mathbf{x}_t, \mathbf{y}_t, \mathbf{x}) \sim N(\boldsymbol{\mu}_{Po}, \boldsymbol{\Sigma}_{Po}) \tag{4–2}$$

where, $\boldsymbol{\mu}_{Po}$ and $\boldsymbol{\Sigma}_{Po}$ are the posterior mean and covariance of $f(\mathbf{x})$. The essential ingredients of GPR is presented below, without providing a comprehensive overview of this method. For details, readers of interest can refer to [119].

GPR model can be defined using function-space view and/or weight space view for posterior mean and variance calculation. The weight space view is given by Eq. (4–3) making it analogous to the standard linear model with non-linear function of the inputs [119].

$$f(\mathbf{x}) = \phi(\mathbf{x})^{\mathrm{T}} \mathbf{w} \tag{4–3}$$

where, $\mathbf{x}$ is the input parameter, $\phi(\mathbf{x})$ is a mapping function and $\mathbf{w}$ is the weight vector.

4.3.2 Kernel Functions

The covariance between the data points is defined using the so-called kernel functions. These co-variance functions measure the correlation between different input data points using some special functional relation. Each of these kernel functions has hyper-parameters that build a functional relation with the distance between input points. For instance, when $\boldsymbol{x}$ is a scalar, the hyper-parameters basically comprise

of a length scale (l) that takes into account the closeness of the input points between $\boldsymbol{x}$ and $\boldsymbol{x'}$, a scale factor (σ_k) which governs the average distance of function value or deviation from its mean, and another scale factor (σ_{v}) which accounts for noise in the observed dataset. A typical kernel function has the form as shown in Eq. (4–4):

$$K(\mathbf{x},\mathbf{x}';\Theta:\sigma_k,l,\sigma_{\mathrm{v}}) = \sigma_k{}^2 f(\mathbf{x},\mathbf{x}',l) + \mathbf{I}\sigma_v{}^2 \tag{4–4}$$

where, $\mathbf{x}$, and $\mathbf{x}'$ are input data points, $\sigma_{\mathrm{k}},l,\sigma_{\mathrm{v}}$ are hyper-parameters represented by Θ and $\mathbf{I}$ is an identity matrix.

4.3.3 Formulation

In order to build a GP model the observed response or points are treated as samples, which are assumed to be drawn from Gaussian process to be fitted, and thus are used as training points. Some portion of observed data-set is used while training or fitting the model and the remaining are known as testing points. These testing points are used for checking the goodness of fit of model before deploying it. As GP is a collection of random variables, any finite number of which has multivariate normal distribution. The joint distribution of the training and testing points according to the prior probability distribution is given by Eq. (4–5):

$$P(Y_{TR},Y_{TS}) \sim N\left(\begin{bmatrix}\mu_{TR}\\ \mu_{TS}\end{bmatrix},\begin{pmatrix}K(X_{TR},X_{TR}) & K(X_{TR},X_{TS})\\ K(X_{TS},X_{TR}) & K(X_{TS},X_{TS})\end{pmatrix}\right) \tag{4–5}$$

where, Y_{TR} is the training output, Y_{TS} is the testing output, μ_{TR} is the mean of training output, μ_{TS} is the mean of testing output, X_{TR} is the training input, X_{TS} is the testing input, and $K(.)$ are the co-variance matrices or the kernel functions. If there are n_{TR} training points and n_{TS} testing points the co-variance matrix will have $n_{TR}\times n_{TS}$ dimension.

For predicting values of testing points or other points, the sample are drawn from the posterior distribution formed by conditioning on the observations as shown by Eq. (4–6):

$$P(Y_{TS} \mid X_{TS}, X_{TR}, Y_{TR}) \sim N(\mu_{TS|TR}, \Sigma_{TS|TR}) \tag{4–6}$$

where, $\mu_{TS|TR}$ and $\Sigma_{\boldsymbol{TS|TR}}$ are the mean and co-variance of the posterior distribution given by Eq. (4–7) and Eq. (4–8) respectively.

$$\mu_{TS|TR} = \mu_{TS} + K(X_{TS}, X_{TR}).K(X_{TR}, X_{TR})^{-1}.(Y_{TR} - \mu_{TR}) \tag{4–7}$$

$$\Sigma_{TS|TR} = K(X_{TS}, X_{TS}) - K(X_{TS}, X_{TR})K(X_{TR}, X_{TR})^{-1}K(X_{TR}, X_{TS}) \tag{4–8}$$

4.3.3.1 Hyper-parameter Tuning

An optimum set of parameters $\sigma_{\mathrm{k}}, l, \sigma_{\mathrm{v}}$ is required for designing an appropriate kernel function that can closely define the underlying relation between the data points. In GPR, usually the set of hyper-parameters that maximizes the log-marginal likelihood of the posterior is selected as the optimum set of values. The log marginal likelihood can be estimated using Eq. (4–9):

$$\log P(Y_{TR} \mid X_{TR}) = \log N(Y_{TR} \mid \mu_{TR}, K_{TR}) = -\frac{1}{2} {Y_{TR}}^{T} {K_{TR}}^{-1} Y_{TR} - \frac{1}{2}\log \mid K_{TR} \mid - \frac{N}{2}\log(2\pi) \tag{4–9}$$

where, Y_{TR} is the training output, X_{TR} is the training input, μ_{TR} is the prior mean of training output, K_{TR} is the kernel function of the training inputs with the hyper-parameters to be tuned.

4.3.4 Implementation of GPR Modeling

In this section detailed methodology of implementation of Gaussian Process Regression (GPR) for estimating the influence coefficients and hence the SIF values is discussed. A brief introduction of Gaussian Process Regression module in *scikit-learn* [120] library in Python programming language [121] and appropriate model parameter selection is discussed. The results and discussion on implementation of GPR for SIF estimation based on tabulated values of coefficients G_0 and G_1 are then presented.

4.3.4.1 Introduction to *scikit-learn* library for Gaussian Process Regression Modeling

The theoretical background of the Gaussian Process was presented in the previous section. Specifically, formulae for estimation of mean and co-variance of the fitted joint- Gaussian distribution conditioned on the training data is of special interest. As these equations help in estimating the mean and variance of the output based on the input, which is a classic regression problem. As such, *scikit-learn* library has a *GaussianProcessRegressor* class which takes in various input parameters and produce output such as mean, standard deviation [120] . The algorithm used for implementation of GPR in *scikit-learn* library is Algorithm 2.1 from Rasmussen et al. (2006) [119]. In this study scikit-learn version 0.23.1 is used.

Under *sklearn.gaussian_process* module the *GaussianProcessRegressor* class is implemented. A module in python simply means a collection of logical codes written to solve a problem, which can be imported inside other python function. Furthermore, a class is a means of bundling data and functionality together. Once imported the *GaussianProcessRegressor ( )* class can be used to fit or train a GPR model using the training data points, make predictions, draw samples from prior and fitted posterior distribution. The key input parameters for this class are *kernel, alpha, optimizer, n_restarts_optimizer, normalize_y.* The *kernel* input is the function which specifies the covariance function of the GP. The *alpha* is the value added to the diagonal of the kernel matrix, to ensure positive definiteness of the co-variance matrix and default value is 1^{-10}. The *optimizer* input is used for specifying the optimizing algorithm for hyper-parameters of the kernel function, as default the L-BFGS-B algorithm is used and serves the purpose of this study. The *n_restarts_optimizer* allows to specify the number of time to restart the optimizing algorithm such that log-marginal likelihood is maximized and to avoid local maxima. The *normalize_y* allows users to specify if the target

values to be normalized or not i.e. scale the output values to standard normal distribution, having zero mean and unit variance [120].

Once the input parameters are specified the *GaussianProcessRegressor( )* class can be used to train a GPR model by using *fit ( )* method, where the training data-set can be specified. A method in Python is a function which allows users to perform certain operation. Once trained or fitted using *fit ( )* method i.e. a posterior distribution is defined as explained in section 4.3.3. After which *predict ( )* method can be used to estimate the posterior mean and variance as explained before. There are few other methods like *sample_y ( )* which can be used to draw number of samples from both prior and posterior distributions. The *score ( )* method returns the coefficient of determination of the predictions [120].

4.3.4.2 GPR Model Parameter Selection

GPR is a supervised machine learning algorithm and its performance depends on different factors like selection of appropriate kernel function as discussed earlier. Surrogate models are basically machine learning algorithms that relies on data. Machine learning algorithm which uses data set, i.e. input or labels and corresponding output or features, to create some functional relationship or mapping function between input and output falls under supervised machine learning category.

It is very common practise in supervised machine learning to split up a given data set into training and testing subsets. The subset of data used to fit the model is training data and the one to evaluate the fitness of model is testing data. In order to make the model robust some portion of the data-set, say 20%, is kept unseen such that performance of the model using these unseen data is measured. Common training-testing splits are 80%-20%, 67%-33% and 50%-50% [122]. In order to further improve the generalization of the model, the training subset itself is split into number of subsets. One of such subset is used as validation set for testing the performance of model fitted using other subset. This testing or validation is done before the final testing using the initially held out or unseen testing data.

In this study appropriate kernel function is selected using grid search algorithm implemented in *scikit-learn* library [120]. A grid of different kernel functions: radial basis function (RBF), squared exponential (SQ), Matern 3/2 and Matern 5/2, is created. The grid search algorithm returns the

GPR model built with kernel function having the best performance metric i.e. R^2 value. In order to split the dataset into random training and testing sets, *scikit-learn* library function *train_test_split ( )* is used. Furthermore, repeated k-fold cross validation procedure implemented in *scikit-learn* library function *RepeatedKFold ( )* is used to further improve the generalization of the model as explained earlier. *k* represents the number of folds or subsets to be created from the training data set. Figure 4-1 shows a typical training and testing data set splitting scheme using k-fold cross validation procedure with five folds.

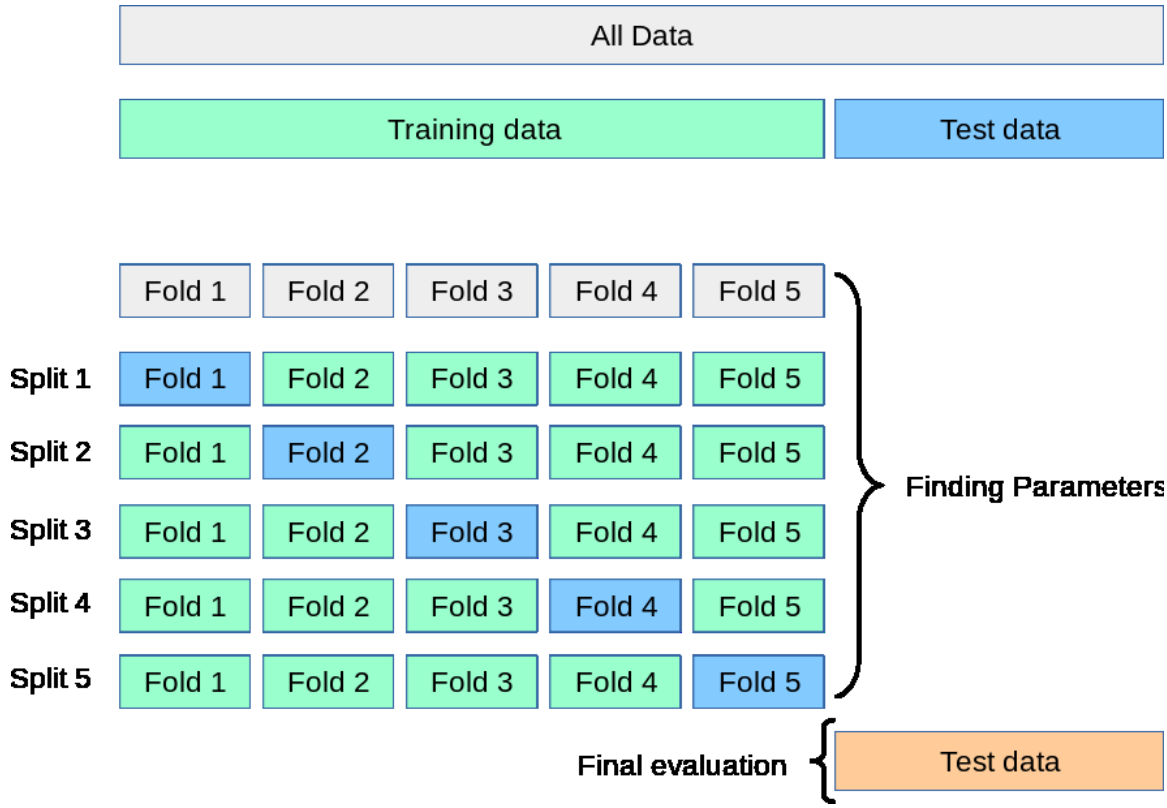

Figure 4-1: Typical k-fold cross validation training and testing data set split schematics [120]

4.3.4.3 GPR Model Development and Deployment

In this section, detailed procedure of developing a GPR model to estimate values of G_0 and G_1 from the tabulated values, measuring the performance of the model and saving it for future use or deployment is discussed.

(1) Illustration of GPR model development with one dimensional input

The coefficients G_0 and G_1 tabulated in Table 9B.13 of API 579 are functions of t/R_i, a/c, and a/t which requires the GPR model to be a three dimensional input model. In order to demonstrate the concept of GPR a simple one-dimensional input problem is first presented. Figure 4-2 shows samples drawn from GP fitted using training data set i.e. from posterior. The training data-set consisted of all the tabulated values of a/t and corresponding values of G_0 for a particular value of t/R_i, a/c. Due to limited number of points train-test split and cross validation is not performed for this one dimensional demonstration problem. It can be observed that the fitted model using RBF kernel function for varying a/t produced a very good model with more certainty in the predictions.

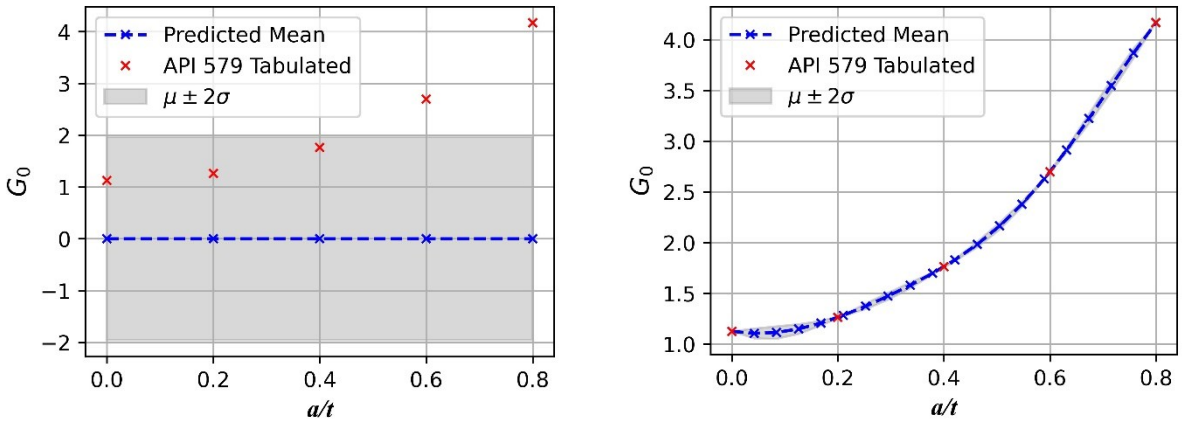

(a) (b)

Figure 4-2: One dimensional GPR model fitted using RBF kernel for estimating G_0 at depth for different values of a/t at t/R_i=0.01 and a/c=0.0625 (a) mean and confidence interval of samples drawn from prior, and (b) mean and confidence interval of samples drawn from posterior

Figure 4-3 shows samples drawn from GP fitted using training data set i.e. from posterior. The training data-set consisted of all the tabulated values of *a/c* and corresponding values of G_0 for a particular value of t/R_i, a/t . It can be observed that the fitted model using radial basis function (RBF) kernel function for varying *a/c* produced a good model but the confidence interval widened when the spacing between inputs increased.

Figure 4-4 shows samples drawn from GP fitted using training data set i.e. from posterior. The training data-set consisted of all the tabulated values of t/R_i and corresponding values of G_0 for a particular value of *a/t*, *a/c*. RBF kernel used for fitting the model for varying t/R_i is poor even though the confidence interval in the posterior is reduced considerably. The uncertainty remains constant except for the first and last inputs.

In addition, when a fitted model is used for making predictions beyond the training data points the confidence interval widens i.e. extrapolation uncertainty increases farther the input from observed data. Figure 4-5 shows predictions made at points beyond the training data set.

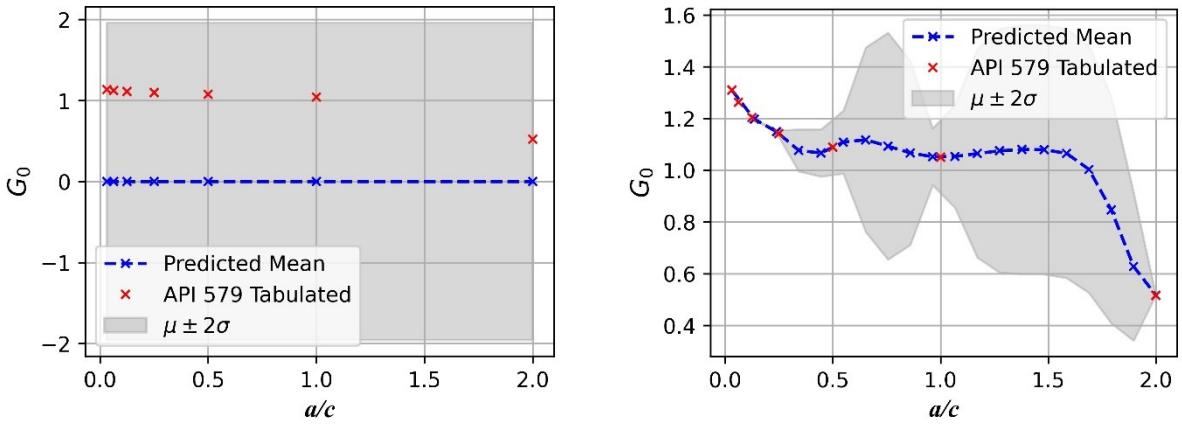

Figure 4-3: One dimensional GPR model fitted using RBF kernel for estimating G_0 at depth for different values of *a/c* at t/R_i =0.01 and *a/t* =0.2 (a) mean and confidence interval of samples drawn from prior, and (b) mean and confidence interval of samples drawn from posterior

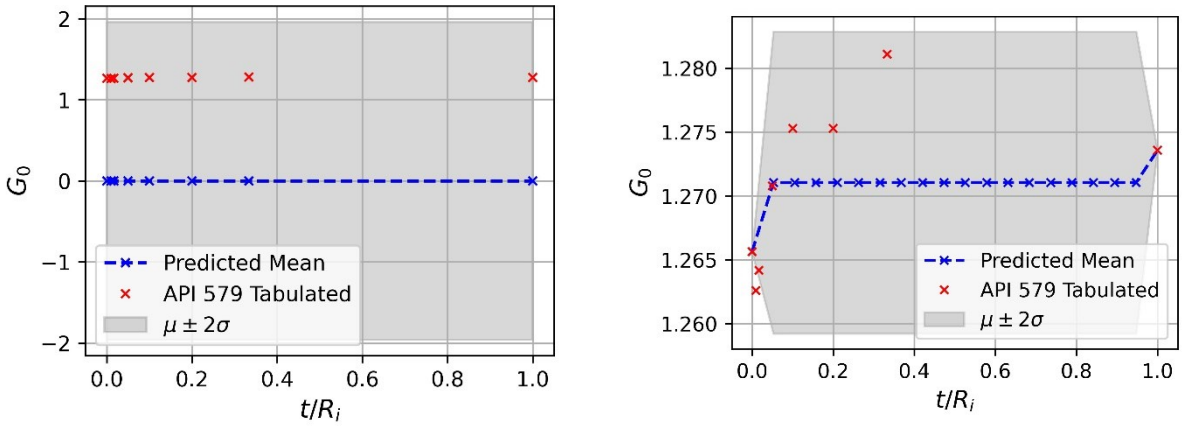

(a) (b)

Figure 4-4: One dimensional GPR model for estimating G_0 at depth for different values of t/R_i at a/c =0.0625 and a/t =0.2 (a) mean and confidence interval of samples drawn from prior, and (b) mean and confidence interval of samples drawn from posterior

A particular kernel function with a set of hyper-parameter might be appropriate for one set of input and output but not necessarily for other sets. In order to solve this problem and build an optimum model, the grid search algorithm and k-fold cross validation algorithms, as discussed in section 4.3.4.2, are employed.

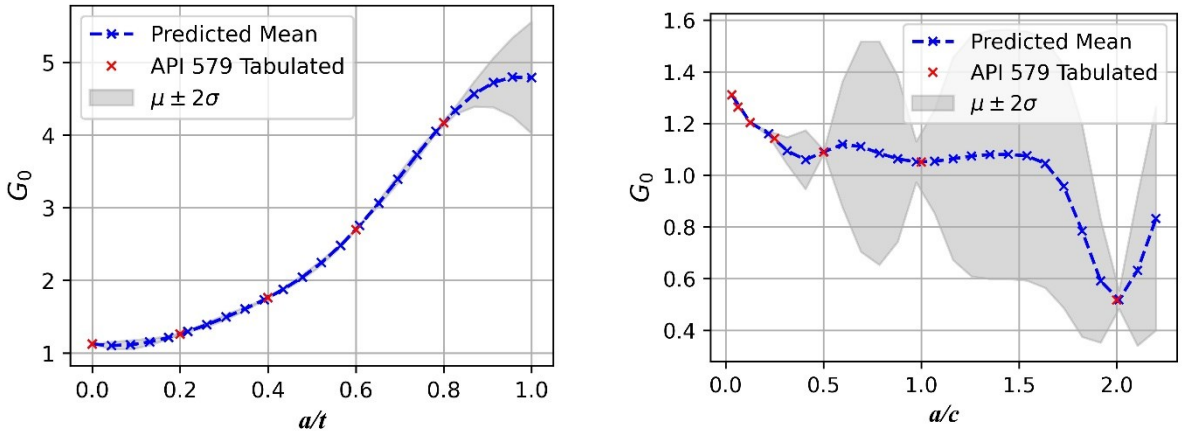

(a) (b)

Figure 4-5: One dimensional GPR model for estimating G_0 (a) mean and confidence interval of samples drawn from posterior with extrapolation for varying a/t, and (b) mean and confidence interval of samples drawn from posterior with extrapolation for varying a/c

(2) Illustration of GPR model development with three dimensional input

In this section details about GPR model development using all three inputs *a/t*, *a/c*, and t/R_i simultaneously to estimate values of G_0 and G_1. A split of 80 % training - 20 % testing of data set is done randomly using *scikit-learn*'s *train_test_split ( )* function. In order to reduce complexity in implementation four separate models for G_0 and G_1 at depth and surface are developed. For each G_0 and G_1, the training and testing data-set contains 224 points and 56 points respectively.

A grid of different kernel functions is created as summarized in Table 4-1. The basic structure of kernel function is as given by Eq. (4–4), formed by adding a basic kernel, like radial basis function (RBF), rational quadratic (RQ), Matern 3/2, Matern 5/2, to the white noise kernel which accounts for uncertainty in the training data. All numerical values within the kernel functions are initial guesses, which are tuned or optimized while fitting the GPR model by minimizing the log-marginal likelihood. As mentioned in section 4.3.4.1, *GaussianProcessRegressor( )* is used to perform all of these operations.

Table 4-1 Grid of Kernel Functions

S.N	Kernel Function
1	$1^2 \times \mathrm{RBF}(l=(\mu_{a/t}, \mu_{a/c}, \mu_{t/R_i})) + 0.001^2$
2	$1^2 \times RQ(l = 0.01, \alpha = 1) + 0.001^2$
3	$1^2 \times \mathrm{Mat3/2}(l=(\mu_{a/t}, \mu_{a/c}, \mu_{t/R_i})) + 0.001^2$
4	$1^2 \times \mathrm{Mat5/2}(l=(\mu_{a/t}, \mu_{a/c}, \mu_{t/R_i})) + 0.001^2$
5	$1^2 \times [\mathrm{RBF}(l=(\mu_{a/t}, \mu_{a/c}, \mu_{t/R_i})) + \mathrm{RQ}(l=(\mu_{a/t}, \mu_{a/c}, \mu_{t/R_i}))] + 0.001^2$

Note: μ represents mean of corresponding input parameters. The kernel function Rational Quadratic (RQ) implemented in *scikit-learn* library allows user to provide only scalar value [120]. So, the smallest distance between input t/R_i is provided as this kernel provided the best fit when tested with simple one-dimensional problem.

As mentioned in section 4.3.4.2, in order combine the grid search algorithm and k-fold cross validation to build a general GPR model *GridSearchCV ( )* function implemented in *scikit-learn*

library is used. The function takes in the basic GPR model, grid of kernels given in Table 4-1, and *RepeatedKFold ( )* with five-fold and repeated five times.

Matern 3/2 kernel is the best fitting kernel function for all the models with optimized hyper-parameters. All of the models have excellent coefficient of determination (R^2) value of more than 0.99. The log-marginal likelihood values are positive indicating that observance of posterior is highly likely and supports the good fit of model. The total duration of model building including grid searching over five different kernel functions, repeated k-fold cross-validation with five-fold and five repetition ranges from 12.609 seconds to 18.75 seconds.

Table 4-2 Model fitting and performance summary

Model	**Best Kernel Function**	**Log-Marginal Likelihood**	**Coefficient of Determination** (R^2)		**Training-Testing Duration** (sec.)
			Train	Test	
G_0 Depth	$1^2 \times Matern(l=[1.16, 0.107, 0.837], \nu=1.5) + 0.01^2$	30.984	0.992	0.995	17.078
G_1 Depth	$1^2 \times Matern(l=[1.31, 0.108, 0.854], \nu=1.5) + 0.01^2$	37.006	0.992	0.995	18.75
G_0 Surface	$1^2 \times Matern(l=[2.95, 0.513, 1.4], \nu=1.5) + 0.01^2$	129.94	0.997	0.996	18.27
G_1 Surface	$1^2 \times Matern(l=[1.89, 0.435, 1.15], \nu=1.5) + 0.01^2$	100.978	0.996	0.991	12.609

Figure 4-6 and Figure 4-7 shows scatter plot for true and predicted values of G_0 and G_1 at surface and depth respectively. A good fit of model can be observed.

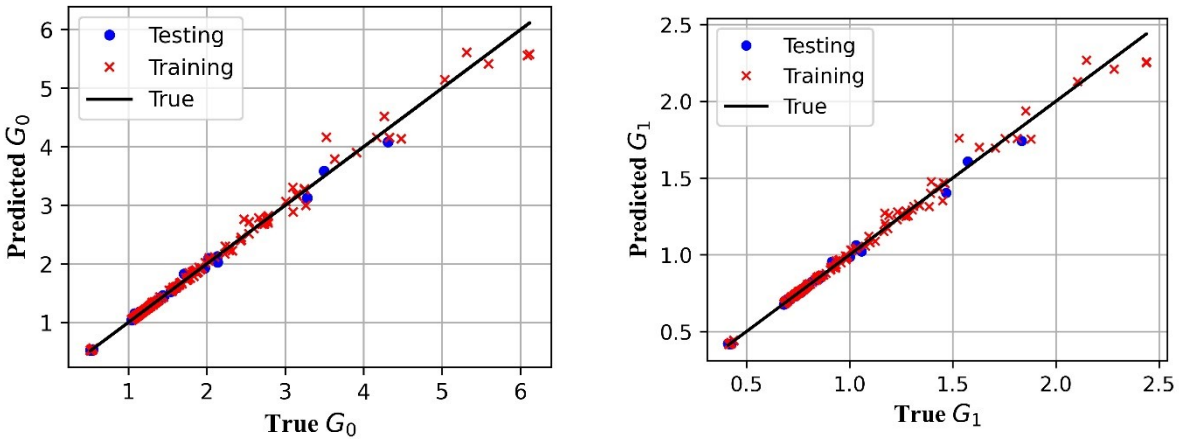

(a) (b)

Figure 4-6: Scatter plot for true training and testing values versus predicted training and testing values of influence coefficients at depth (a) G_0, and (b) G_1

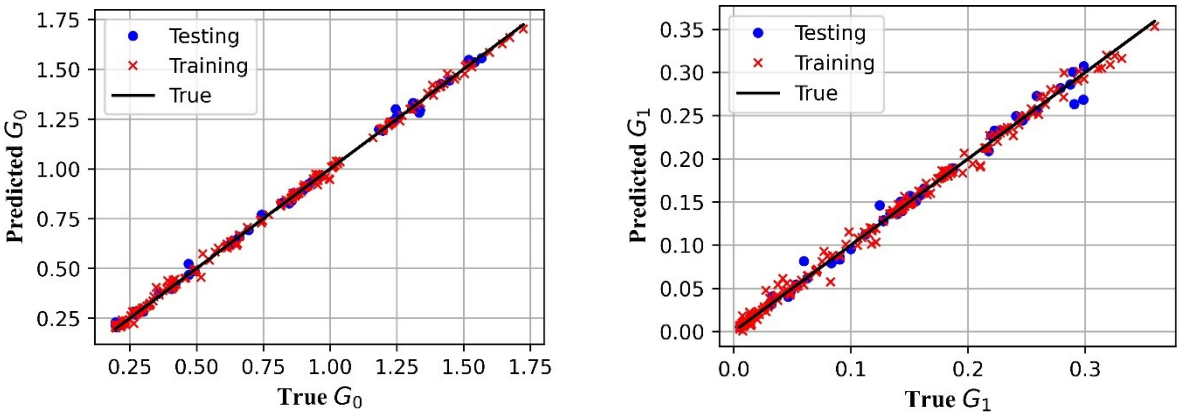

(a) (b)

Figure 4-7: Scatter plot for true training and testing values versus predicted training and testing values of influence coefficients at surface (a) G_0, and (b) G_1

(3) Model deployment

Once the model is developed as explained in the previous section it is saved and stored with all the required components such as kernel or covariance matrix using Python *pickle* [121] library. The use of saved model or deployment in discussed in the next chapter.

A comparison of computational time for estimation of G_0 and G_1 using the fitted GPR model and regular API 579 model is made. G_0 and G_1 were calculated at depth and surface for 1000 points,

including exact values in API 579 look-up table. The computation time between GPR model and interpolating function directly from API 579 model is shown in Table 4-3. The scatter plot between the values estimated using API 579 model directly and developed GPR model for tabulated and intermediate points at depth are shown in Figure 4-8 and Figure 4-9 respectively. Similar plot for the values at surface can be found in ANNEX-B. The coefficient of determination (R^2) for G_0 at depth, G_1 at depth, G_0 at surface, and G_1 at surface for intermediate points were 0.978, 0.975, 0.996, and 0.995 respectively. The GPR model performance is satisfactory and the computational time is drastically low. Hence, the developed GPR model provides a trade-off between computational expenses and accuracy.

Table 4-3 Computation time of different models

Model	**Time (sec)**
	For 1000 points
GPR fitted	0.363
API 579	176.868

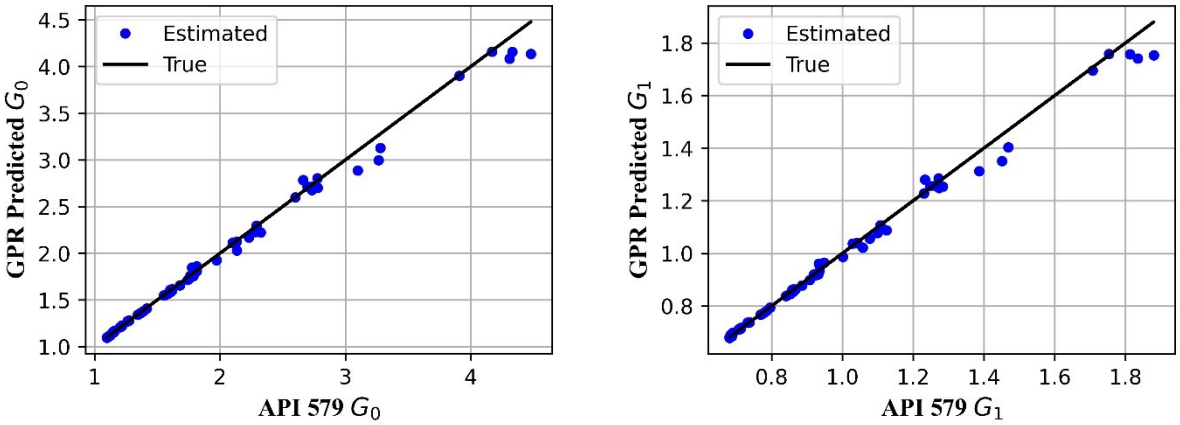

(a) (b)

Figure 4-8: Scatter plot for G_0 and G_1 estimated at tabulated points using API 579 model and developed GPR model at depth (a) G_0, and (b) G_1

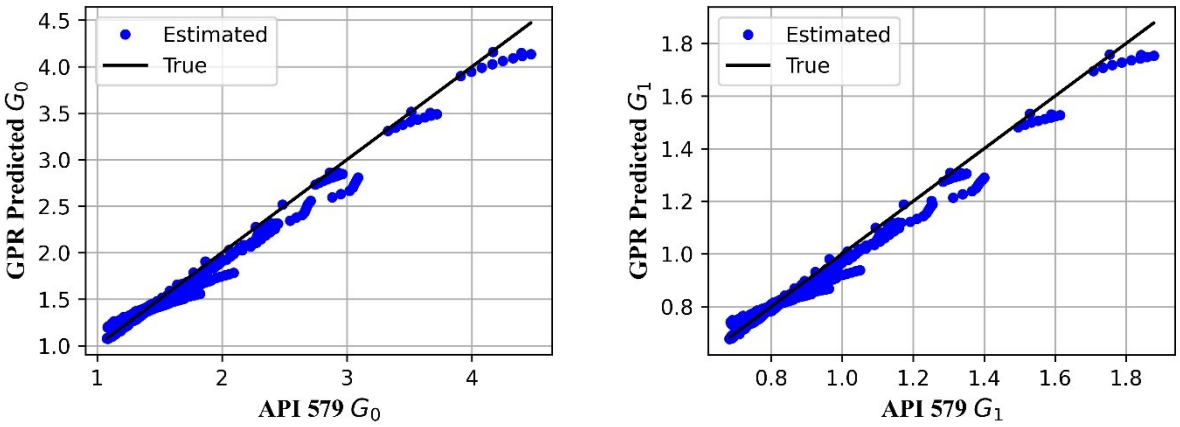

(a) (b)

Figure 4-9: Scatter plot for G_0 and G_1 estimated at intermediate points using API 579 model and developed GPR model at depth (a) G_0, and (b) G_1

4.3 Summary

In this, chapter details related to Gaussian Process Regression as a surrogate model to estimate the values of influence coefficients and hence the SIF is presented. Tabulated values for estimation of influence coefficients from API 579 is used for the training and testing purpose. The tabulated values are obtained from a large set of FE models and was verified using conventional FEM and XFEM for different pipelines is previous chapter. The accuracy of prediction, computational time and confidence interval estimated by GPR makes it a very good alternative tool to high-fidelity numerical models for estimation of SIF.

Performance of GPR greatly depends on the kernel or co-variance function with appropriate set of hyper-parameters. A grid-search over different types of standard kernel function helps in building an optimum performing model and is recommended. With increase in the dimensionality, the complexity of the GPR model fitting increases. Performing one-dimensional modeling before performing high dimensional modeling can provide a better insight of the underlying trend of the training data points. The optimum model fitting time and accuracy, with all necessary pre-processing steps like kernel function selection, hyper-parameter tuning, and training-testing splitting is very reasonable. Matern 3/2 is found to be the best kernel function based on the grid search performed using five-fold cross-validation with five repetition. The GPR trained model can

be saved and used later for routine tasks. The computational time from fitted GPR model for a large number of data points is negligible when compared to that from the regular API 579 model.

CHAPTER 5: A BAYESIAN APPROACH FOR FATIGUE CRACK GROWTH MODELING IN PIPELINES INTEGRATED WITH FATIGUE CRACK DRIVING PARAMETER ESTIMATION SURROGATE MODEL

5.1 Introduction

The fatigue crack growth model Paris' law, as discussed in previous chapters, requires reliable values of crack geometry and the material properties for good modeling performance. This chapter introduces stochastic filtering method specifically Particle Filter (PF) for fatigue crack growth model parameters and current crack size or state estimation. PF is an algorithm, which provides best estimate based on the available measurement data (e.g. ILI data) and a system model (e.g. Paris' law) which describes the phenomenon. Thus, a pseudo fatigue crack growth data set is generated for a pipeline and made noisy to mimic the ILI data by adding different levels of Gaussian white noise. A methodology to integrate PF, Paris' law and surrogate model to estimate model parameters, current crack size and future fatigue crack growth trajectory is proposed and implemented using a Python based tool. The performance of the tool, i.e. comparison between the true values of the crack sizes and model parameters to the predicted mean values with the confidence interval band, is presented for different cases and the results are reliable.

5.2 Stochastic Filtering for Fatigue Crack Growth Modeling in Pipelines

5.2.1 Particle Filter (PF)

Particle Filter (PF) method is a set of Monte Carlo algorithms that relies on repeated random sampling to obtain numerical results to solve filtering problems. The fundamental concept of PF is based on Bayesian approach, where posterior distribution is obtained by multiplying likelihood function with the prior distribution. In PF the prior and posterior probability density function (PDF) of parameters are represented by particles (samples). It has become a very popular numerical method for optimal estimation in non-linear non-Gaussian scenarios.

The principal advantage of PF over a popular standard approximation method Extended Kalman Filter (EKF) is that it does not rely on any local linearization or any crude functional approximation [123].

A generic algorithm of standard particle filter in shown below (see Algorithm 5-1) [124]

Algorithm 5-1

Line 1: Draw $\mathbf{X}_0^i$ from the prior PDF $p(\mathbf{X}_0)$, $i \in 1...N$

Line 2: Set $\mathbf{W}_0^i = 1/N$, $i \in 1...N$

Line 3: for time step $k \to 1$ to k do

Line 4: for $i \to 1$ to N do

Line 5: Sample $\mathbf{X}_k^i$ from $p(\mathbf{X}_k \mid \mathbf{X}_{k-1}^i)$

Line 6: Set $\mathbf{W}_k^i = \mathbf{W}_{k-1}^i . p(z_k \mid \mathbf{X}_k^i)$

Line 7: Normalize weights, $\hat{\mathbf{W}}^i = \dfrac{\mathbf{W}_k^i}{\sum \mathbf{W}_k^i}$

Line 8: for $i \to 1$ to N do

Line 9: Sample $\mathbf{X}_k^i \sim p(\mathbf{X}_k \mid z_k)$ by drawing new particles from the distribution defined by $(\mathbf{X}_k^j, \hat{\mathbf{W}}^j)$, $j \in 1...N$

Line 10: Set $\mathbf{W}_k^i = 1/N$, $i \in 1...N$

where, $\mathbf{X}$ is the state-parameter vector, $\mathbf{W}$ is the weight vector, z is the measurement, k is the time step, $p(.)$ is the PDF. The algorithm is described in detail using case studies in the section 5.4.

A general description of the algorithm can be presented in the following manner. A PF is initialized with an adequate number of particles sampled randomly from a distribution (for e.g. uniform, normal, and log-normal) for each state and parameter based on the experience or literature (Line 1). At the initial stage each of the generated particles are assigned equal weight i.e. 1/N such that the sum of all probabilities equals one, this combination of particles and weights forms the probability distribution (Line 2). In the prediction step a numerical model (e.g. Paris' Law)

describing the fatigue crack growth is used to update the belief in the system state with some noise which accounts for the uncertainty in the process model (Line 5). Based on the likelihood of the observed noisy measurement the weights of the predicted state are updated (Line 6 and 7). The particles close to the measurement data will generally have a higher weight, which is referred to as Sequential Importance Sampling (SIS). The SIS algorithm suffers the degeneracy phenomenon which occurs when the weights are updated with the same initial samples. Thus, large weight is assigned to the particles very close to the measurement and extremely low weight to the farther ones. There might be a scenario where very less number of particles with extremely high weights, meaningfully contributing to the estimation, be sampled [125]. This can lead to inaccuracy, which is the so-called filter degeneracy. Thus, a resampling algorithm is used (*Line* 9 and 10). The resampling algorithm discards particles with very low probability and replaces them with new particles with higher probability. The particles with relatively high probability are duplicated and slightly dispersed by the noise resulting in a set of points having large majority of the particles representing the distribution with higher accuracy [125].

In order to solve the filter degeneracy various resampling algorithms are popular like multinomial resampling or simple random sampling, residual resampling, stratified resampling, systematic resampling. In multinomial resampling the cumulative sum of the normalized weights is computed which gives an array of increasing values from 0 to 1. To select a weight a random number generated from uniform distribution between 0 and 1 and using binary search to find its positions in the cumulative sum array. This resampling algorithm can be implemented using inverse of the cumulative distribution function (CDF) of the distribution [81]. In residual resampling, the normalized weights are multiplied by number of particles (N), and then the integer value of each weight is used to define how many samples of that particle will be taken and will have some left out. For which residual is taken, the weights minus the integer part leaving the fractional part of the number. After which a multinomial resampling is done to select the rest of the particles based on the residual. Stratified resampling works by dividing the sample space into N equal sections, and then selecting one particle randomly from each section which guarantees that each sample is between 0 and $2/N$ apart. Systematic resampling works by dividing the sampling space into N divisions, then choosing a random offset to use for all of the divisions, ensuring that each sample is exactly $1/N$ apart. Choice of an appropriate resampling algorithm depends on the type of problem

and prior knowledge. However, in practise stratified and systematic resampling algorithms are considered to be superior to the other two across a variety of problems [125].

5.3 Methodology for Integration of Particle Filter and Surrogate Model for State-Parameter and Future Trajectory Estimation

In this study, a PF-based fatigue crack growth prediction methodology for pipelines is developed by integrating crack size measurement and predictions from a fatigue crack evolution model. Specifically, Paris law as discussed in previous chapters is used to model the fatigue crack growth, utilizing SIF ranges and fatigue material properties, as reflected by fatigue model parameters. In this proposed methodology, fatigue model parameters and crack sizes will be jointly estimated using PF. Afterwards, the fatigue crack growth model with updated parameters and current estimate of crack sizes will be utilized to predict future trajectory of the fatigue crack growth in pipelines. In this section, model formulation for joint state-parameter estimation via PF using noisy observation data, and estimation of SIF using GPR model is presented briefly. In this study, the cracks are assumed to be longitudinal surface crack with semi-elliptical crack front. Unless otherwise specified, minor radius of the semi elliptical crack front is the crack depth 'a' and the major radius is the half crack length 'c'.

5.3.1 Particle Filter and State-space model formulation

In fracture mechanics-based assessment the crack growth rate with respect to the number of loading cycles is related to the crack driving parameters. For example, Paris law, introduced by Paris and Erdogan in 1963 [41], is one of such equations that quantifies the crack growth rate of the stable fatigue crack growth as a function of SIF, see Eq. (5–1) for the crack depth a (measured along wall thickness direction) and crack length c (measured along the longitudinal direction).

$$\frac{da}{dN} = C(\Delta K_a)^m$$
$$\frac{dc}{dN} = C(\Delta K_c)^m \tag{5–1}$$

where, da/dN and dc/dN are the rate of fatigue crack growth per loading cycle; C and m are the fatigue model parameters related to the properties of the material; ΔK_{α} and ΔK_{c} are the range of SIF at the depth and surface respectively when a structure is stressed from minimum to maximum load in a loading cycle. Eq. (5–1) can be discretized as Eq. (5–2):

$$a_k = f(a_{k-1}; C, m) = C(\Delta K_{a,k-1})^m \cdot \Delta N_{k-1} + a_{k-1}$$
$$c_k = f(c_{k-1}; C, m) = C(\Delta K_{c,k-1})^m \cdot \Delta N_{k-1} + c_{k-1} \quad (5–2)$$

where, a_k and c_k are the crack sizes at current time step k, $\Delta K_{a,k-1}$ and $\Delta K_{a,k-1}$ are the range of SIF at the previous time step *(k-1)*, ΔN_{k-1} is the number of load cycles, C and m are time-invariant model parameters.

This fatigue crack growth model can be incorporated into a state-space model, which also includes crack measurement model for its use in PF. The crack growth model is given by Eq. (5–3):

$$\mathbf{X}_k = \boldsymbol{f}(\mathbf{X}_{k-1}) + \boldsymbol{w} \quad (5–3)$$

where, $\mathbf{X} = [a, c]$ is the state vector, $\boldsymbol{f}(.)$ is the state transition model, k is the time step and $\boldsymbol{w}$ is the process noise, which is used to facilitate the Bayesian estimation of state variables. In joint state-parameter estimation, the model parameters (C, m) are assumed to be time-invariant and added to the state vector to form the augmented state vector $\mathbf{X} = [a, c, C, m]$. This is a common approach when unknown model parameters are to be estimated together with the states [97]. Thus, the state transition equation for the augmented state vector can be written as Eq. (5–4):

$$\begin{bmatrix} a_k \\ c_k \\ C_k \\ m_k \end{bmatrix} = \begin{bmatrix} C_{k-1}.(\Delta K_{a,k-1})^{m_{k-1}}.\Delta N_{k-1} + a_{k-1} \\ C_{k-1}.(\Delta K_{c,k-1})^{m_{k-1}}.\Delta N_{k-1} + c_{k-1} \\ C_{k-1} \\ m_{k-1} \end{bmatrix} + \begin{bmatrix} w_a \\ w_c \\ w_C \\ w_m \end{bmatrix} \quad (5–4)$$

where, (C, m) are time-invariant fatigue model parameters but their estimations at the previous and current time steps are denoted by $\left(C_{k-1}, m_{k-1}\right)$ and $\left(C_k, m_k\right)$, respectively; w_a, w_c, w_C, w_m are process noise for states and parameters.

The measurement model for the crack size observation available from ILI is shown in Eq. (5–5):

$$\mathbf{Y}_k = \boldsymbol{h}(\mathbf{X}_k) + \boldsymbol{v} \tag{5–5}$$

where, $\mathbf{Y}_k$ is the observation vector at time step k for the state vector $\mathbf{X}_k$ and $\boldsymbol{v}$ is the observation noise. Since the crack size in the augmented state variable is assumed to be measurable with measurement error while the model parameters are not observable, $\boldsymbol{h}(.)$ is simply as shown in Eq. (5–6):

$$\mathbf{Y}_k = \begin{bmatrix} a_k \\ c_k \end{bmatrix} + \begin{bmatrix} v_a \\ v_c \end{bmatrix} \tag{5–6}$$

where, v_a and v_c are the measurement noise from ILI tool for crack sizes a and c respectively.

Given observation data $\mathbf{Y}_k$ till time step k corresponding to the number of load cycles N_k, i.e., $\left\{\left(0, a_0\right), \left(N_1, a_1\right), ..., \left(N_k, a_k\right)\right\}$, Bayesian inference can be performed to estimate the probability distribution of state vector $\mathbf{X}_k$ iteratively at time step k making use of the state-space model defined in Eq. (5–4) and Eq. (5–6). However, exact solution is not possible in general since complex high-dimensional integrations are required. Particle Filter (PF) method is a set of Monte Carlo algorithms that rely on repeated random sampling to obtain numerical results of such filtering problems. It has become a very popular numerical method for optimal estimation in non-

linear non-Gaussian scenarios [123], and is thus suitable for the joint state-parameter estimation problem considered in this study.

5.3.2 Surrogate model for Stress Intensity Factor Estimation

The surrogate model developed using Gaussian Process Regression (GPR) from the data points provided in Table 9B.13 of API 579 [10] is used for stress intensity factor estimation. The details about the GPR model development and deployment can be found in chapter 4.

The developed GPR model takes the pipe and crack geometrical properties t/R_i, a/c, and a/t to estimate the values of coefficients G_0 and G_1. t/R_i is the ratio of pipe wall thickness, a/c is the ratio of crack depth to the half crack length, and a/t is the ratio of crack depth to the pipe wall thickness. The coefficients are further used with the Eq. (5–7) to estimate the value of SIF.

$$K = \frac{pR_i^2}{R_o^2 - R_i^2}\left[2G_0 + 2G_1\left(\frac{a}{R_0}\right) + 3G_2\left(\frac{a}{R_0}\right)^2 + 4G_3\left(\frac{a}{R_0}\right)^3 + 5G_4\left(\frac{a}{R_0}\right)^4\right]\sqrt{\frac{\pi a}{Q}} \qquad (5\text{–}7)$$

where, p is the internal pressure, R_i is the internal radius, R_o is the outer radius, a is the crack depth, Q is a parameter based on crack geometry, G_0 and G_1 are estimated using the developed GPR model, G_2, G_3 and G_4 are functions of G_0 and G_1. The equations of Q, G_2, G_3 and G_4 can be found in ANNEX-C.

5.3.3 Python-based Tool Implementation

The methodology proposed for joint estimation of Paris law parameters and crack size in pipelines using noisy crack size measurements is implemented as a tool using Python programming language, as it provides a free environment [124] and thus facilitates its further development and future use. Python is an object-oriented programming language, which is popular in both scientific research and engineering communities since it helps programmers even with less experience to write clear and logical code [126]. Furthermore, it also has large number of open-source libraries that help to develop practical tools by taking advantage of existing libraries like *NumPy*, *Pandas*, *SciPy* and others, as used in this study.

The tool implemented here mainly consists of five modules: (1) cracked pipe specification module, (2) fatigue driving parameter calculation module (e.g., *GPR Model*), (3) fatigue crack evolution module (e.g., *Paris Law*), (4) stochastic estimation module (e.g., *Particle Filter*), and (5) fatigue crack prediction. These modules, as shown in Figure 5-1, are integrated to first update fatigue model parameters and estimate the current crack size from its noisy measurement, and then to predict future crack growth using the fatigue crack growth model with updated model parameters and crack size. Each module is briefly described next.

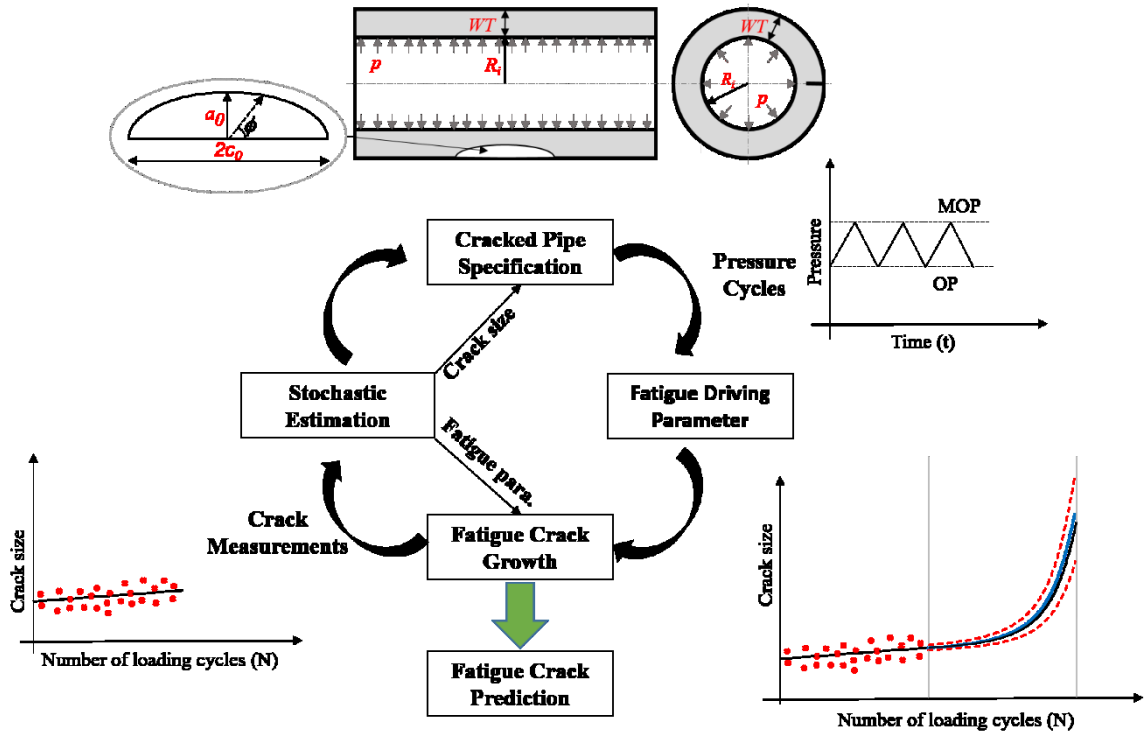

Figure 5-1: Schematic illustration of the Python modules implemented for joint state-parameter estimation and Bayesian fatigue crack prediction

The cracked pipe specification module contains the information related to a cracked pipeline. Specifically, they include pipe wall thickness ($WT = t$), pipe outside diameter (R_o) or inside radius (R_i), as well as the longitudinal crack depth (a_0) and half crack length (c_0) that can be initial guesses or rough estimate based on experience or preliminary detection devices. The crack geometry (a, c) will be updated once a measurement at a future time is available.

The fatigue driving parameter calculation module contains models to calculate the SIF, or other fatigue driving parameters. For example, *GPR Model* is implemented in the current tool to estimate the values of SIF, along the semi-elliptical crack front on the external surface of pipeline subjected to internal pressure. For a given input of pipe geometry (t, R_i), crack geometry (a, c), location (ϕ) and load pressure range $(p = p_{\max} - p_{\min})$, a SIF value is calculated based on GPR model developed and deployed as discussed in Chapter 4.

The fatigue crack evolution module contains established fatigue crack growth models, such as *Paris Law*, which is used to estimate the future crack size a_k and c_k for additional load cycles (ΔN_{k-1}) based on the previous crack size a_{k-1}, c_{k-1} and fatigue model parameters $(e.g., C, m)$ according to Eq. (5–4), ΔK_{k-1} is the range of SIF when a pipe is stressed from minimum ($p_{\min}$) to maximum pressure ($p_{\max}$). The value of SIF is estimated by calling the *GPR Model*.

The stochastic estimation module contains stochastic filters such as *Particle Filter*, which performs joint state-parameter estimation. It will take in measurements iteratively, i.e., one measurement data at a time, to estimate the crack size and model parameters along with their corresponding weights, which provide a probabilistic measure of the estimates. The final output of the function is the mean values of the cracks and model parameters, and their corresponding standard deviation or confidence interval. The mean values will provide updated values of the current crack size and more accurate estimate of the model parameters. In order to overcome the filter degeneracy problem this module uses systematic and stratified resampling methods from a python library *FilterPy* [125]. The stratified and systematic resampling function implemented in the *FilterPy* library returns the indexes of the particles to be resampled. These indexes are then used to perform resampling, where particles with relatively high probabilities are retained and those with low probabilities are discarded and every particle is assigned with the same weight.

The last module is for fatigue crack prediction, which uses the fatigue growth module but with the updated values of the current crack size and more accurate estimate of the model parameters. This module can be called each time to predict the crack growth curve in the future after a measurement is integrated in the stochastic estimation process.

5.4 Case Studies

As discussed in previous sections, for reliable prediction of fatigue crack growth, the current crack size, i.e. a, and c, and fatigue model parameters, i.e. C and m, are required within reasonable accuracy. In order to demonstrate the application of the proposed methodology and the developed tool, pseudo-data set is generated using simulation data from the fatigue crack evolution model, i.e., Paris law and GPR model for SIF estimation for a pipeline, and polluting the simulation data with additive Gaussian white noise to mimic measurement error from an ILI tool. Note this method is not limited to the pipe steel grade. However, for different pipe steel grades, the prior information about the fatigue properties can be different. Thus, better information about the pipe properties (e.g., Paris' law parameters) will allow the estimate of the model parameters to converge faster with less data required.

5.4.1 Pseudo Data Generation

A pipeline section reported to have an incident related to fatigue crack in pipe body in the Pipeline and Hazardous Materials Safety Administration (PHMSA) database is selected. The geometric details and operating condition and pipe material are summarized in Table 5-1. In this study it is assumed that a fatigue crack has been correctly identified assuming no other co-existing defects. If other defects exist, the accuracy of the model used for fatigue crack growth prediction in this study will be affected. As such, more accurate models for crack growth prediction considering the effect of other defects can be used in this method.

Table 5-1 A pipeline reported to have an incident related to fatigue crack in pipe body in PHMSA database

#	**Operator Name**	**WT, t** (mm)	R_i (mm)	t/R_i	**OP** (MPa)	**MOP** (MPa)	**SMYS** (MPa)	**Pipe Specification**
1	Colonial Pipeline Co	7.137	450.063	0.016	2.179	4.000	358.527	API 5L-X42

Two case studies are presented in the following sections. In the first case study, the data set generated includes the number of loading cycles (N) and the corresponding crack sizes along

thickness direction i.e. crack depth a only. The data set starts from loading cycle number zero which corresponds to the first detected crack. The initial crack geometry is taken such that the initial crack depth (a) is 20% of wall thickness, i.e. 1.427 mm. Furthermore, the half crack length (c) is 4 times the crack depth and assumed unchanged in the first case, assuming that fatigue crack does not grow much along the longitudinal direction [70]. The initial crack geometry is selected in such a manner that it represents a short shallow crack and eventually grows out to become a short deep crack i.e. $0.25 \le a/c \le 1.0$, which in turn allows use of value of Q for $a/c \le 1.0$ as shown in Eq. (C-3). While simulating the fatigue crack growth (FCG) data for first case, SIF is calculated based on constant t/R_i (constant for a given pipe) and varying a/c and a/t as they vary with crack depth. For the pipeline section considered in this study the value of SIF at depth is about 1.81 times (at $a/t = 0.2$ and $a/c = 0.25$) higher than that at the surface, causing the fatigue crack growth along the thickness direction 6 times higher than along the longitudinal direction.

Whereas, in the second case the data set generated includes the number of loading cycles (***N***) and the corresponding crack sizes along both thickness direction i.e. crack depth a and axial direction i.e. half crack length c. The initial crack geometry is taken such that the initial crack depth (a) is 20% of wall thickness, i.e. 1.427 mm. and the half crack length (c) is 4 times the crack depth (a) i.e. 5.708 mm.

Gaussian white noise, i.e. $N(0, {\sigma_{ILI}}^2)$, with two different noise level (σ_{ILI}) are added to the generated data set to mimic ILI tool measurement data. In this study $\sigma_{ILI} = 0.15\ mm,$ and $0.30\ mm$ are added to the generated data in both cases. These are assumed to be ILI tool error and adopted from Xie et al. (2019) [24].

The values of C and m mentioned in API 579 (Clause 9F.5.3.2), for ferritic and austenitic steels in air or other non-aggressive service environment at temperatures up to $100\,°C$ and yield strengths less than or equal to 600 MPa, are 5.218×10^{-13} $(mm/Cycle, MPa\sqrt{mm})$ and 3.00 respectively is used for the data generation purpose. The range of internal pressure loading for calculation of the range of SIF (ΔK) is assumed as the difference between the operating pressure (OP) and maximum allowable operating pressure (MOP) of the pipeline, and it is assumed crack size data is available every 1000 cycles (ΔN_k =1000).

5.4.2 Simultaneous Estimation of Crack Depth (*a*) and Paris' Law Model Parameters (*C* and *m*) and Future Trajectory Prediction

Figure 5-2 shows a typical simulated true and noisy crack measurement data, i.e. crack depth (*a*), with noise level of 0.15 mm. Crack length is assumed to be known and kept constant in this case. PF algorithm requires sampling points from assumed distribution as discussed in previous sections. Greater the number of sample better the representation of the posterior estimates. However, use of very large number of data points can be computationally expensive. In this study, only 2000 sample points are drawn from the probability distribution for the state and model parameter variables and it is found reasonable accuracy can be achieved here. Note that Latin hypercube sampling (LHS) technique is used in this study as it ensures samples are picked from the entire distribution especially when the sample size is relatively small.

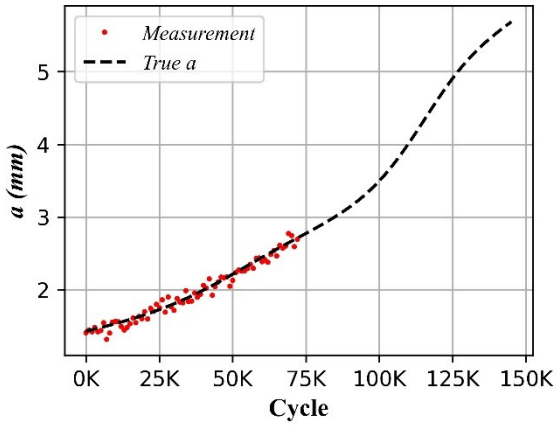

Figure 5-2: Simulated crack depth '*a*' data keeping crack length constant for $\sigma_{ILI} = 0.15\ mm$

5.4.2.1 Case I: Noise level= 0.15 mm

Selection of appropriate set of parameters is very crucial in stochastic filtering techniques. A good approach would be to perform a grid search within range of reasonable values. A priori for state and parameters are drawn from the distribution summarized in Table 5-2. The table also summarizes the probabilistic information for other parameters required for the tool, i.e. the assumed distributions for the measurement and process noise.

Table 5-2 Input data for Particle Filter for noise level=0.15 mm

a_0	$Normal\ (a_{\text{meas},0}, (12.5\% \times a_{\text{meas},0})^2)$ $= Normal(1.165, 0.145^2)$
C_0	$Uniform(125\% \times \log(C_{True}), 95\% \times \log(C_{True}))$ $= Uniform(-35.352, -26.874)$
m_0	$Uniform(0.65 \times m_{True}, 1.05 \times m_{True})$ $= Uniform(1.95, 3.15)$
v_a	$Normal(0, (167\% \times \sigma_{ILI})^2)$ $= Normal(0, 0.25^2)$
w_a, w_C, w_m	$Normal(0, (6.25\% \times \sigma_{ILI})^2), Normal(0, (10^{-2})^2), Normal(0, (10^{-2})^2)$ $= Normal(0, 0.009^2), Normal(0, (10^{-2})^2), Normal(0, (10^{-2})^2)$

Results and Discussion

The joint state-parameter estimation results are shown in Figure 5-3 for noise level of 0.15 mm. Figure 5-3 (a) presents the estimation results of the state variable, i.e., crack depth, with the available data up to 72000 cycles (corresponding to 73 observations, or 50% of the total data generated about 50% of the total generated data). Figure 5-3 (b) and (c) presents the updating histories of the two fatigue model parameters. It can be seen that, with the increase of crack size observations, better mean estimates of the two model parameters can be found and the associated variance is much lower in the model parameters. Figure 5-4 (a) -(c) shows histogram plot for state, and parameters for initial guesses or priors. Figure 5-4 (d) - (f) shows histogram plot for state, and parameters for posterior distribution, i.e. posterior is built incorporating measurement data available up to 72000 cycles. The execution time is approximately 183 seconds.

The future prediction of crack depth *a* based upon the estimated state and updated model parameters at different time steps (related to load cycles here) is shown in Figure 5-5. Figure 5-5 (a) shows the fatigue crack growth prediction made based on initial values of the state and model parameters with no observation. Figure 5-5 (b) - (f) shows the fatigue crack growth predictions when observations are made up to 15000 cycles (with 16 observations), 29000 cycles (with 30 observations), 44000 cycles (with 45 observations), 58000 cycles (with 59 observations), and 72000 cycles (with 73 observations) respectively. It can be observed that the fatigue crack growth curve predicted purely based on the model without using measurement data is way off from the truth, while when more measurement data is used, the prediction of the fatigue crack growth curve

is closer and closer to the truth. At the same time, the uncertainty (or confidence interval) is much less when measurements are used. This trend can be seen in Figure 5-6, which contains a summary plot of these predicted trajectories at different time steps. The shaded areas in Figure 5-5 and Figure 5-6 represents region 95% confidence interval of each state and parameters, also the vertical axis of plots are limited to the wall thickness. 95% Confidence interval of the weighed mean of the state and parameters are calculated from the population of particles using 97.5 and 2.5 percentile. Table 5-3 summarizes the state-parameter estimation results at the end of available data i.e. 72000 cycles.

Table 5-3 State-Parameter estimation summary at the end of 72000 cycles with noise level=0.15 mm

State-Parameter	Mean	95 % Confidence Interval	
		Upper Limit	Lower Limit
a	2.628	2.843	2.451
Log(C)	-27.844	-27.503	-28.494
m	2.914	3.058	2.797

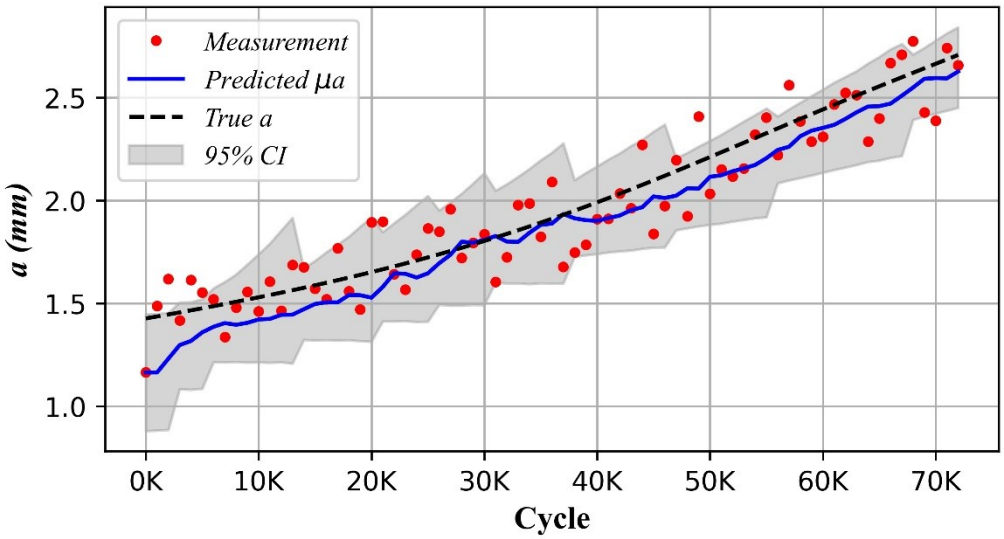

(a)

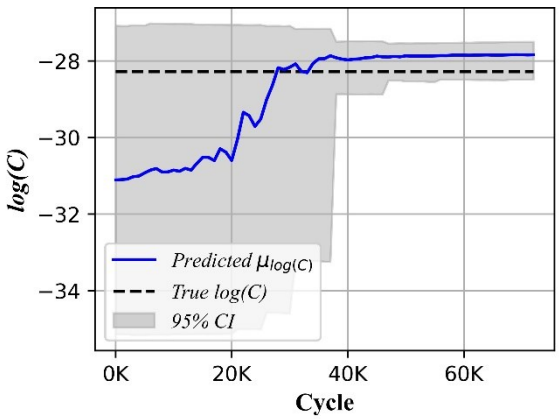

(b)

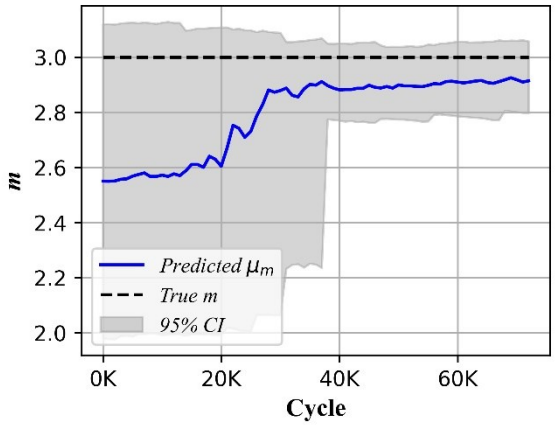

(c)

Figure 5-3: State-parameter estimation results with 95% confidence interval for noise level=0.15 mm (a) State (crack depth) '*a*' estimation, (b) Parameter '*C*' estimation, and (c) Parameter '*m*' estimation

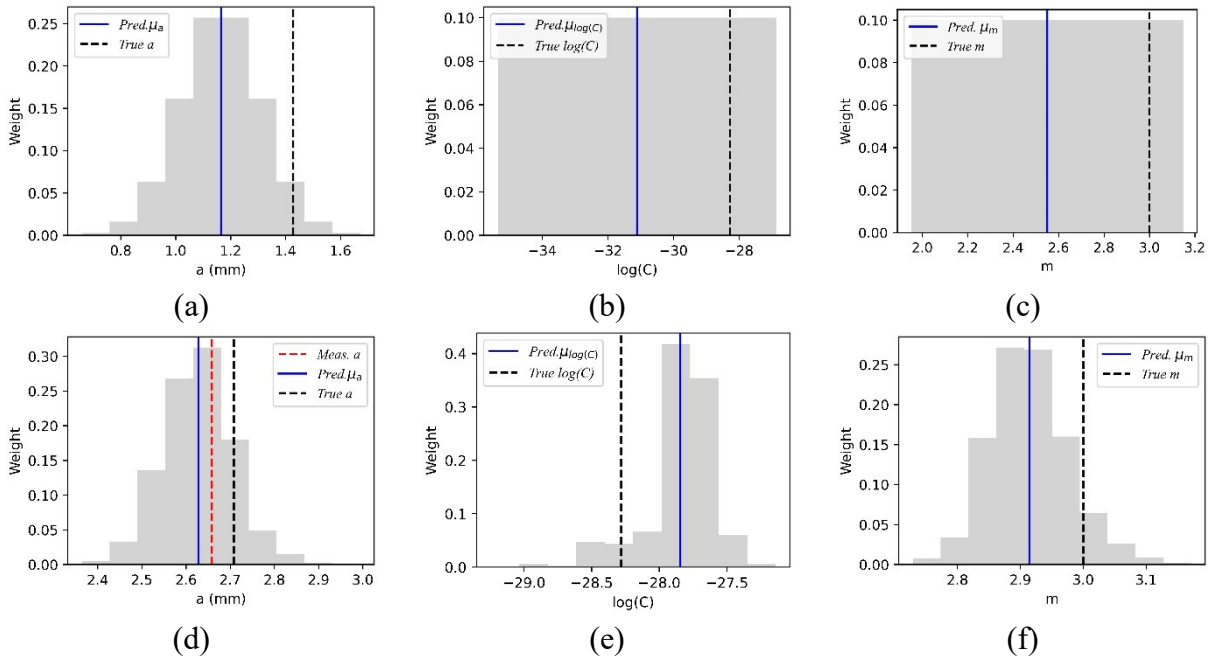

Figure 5-4: Histogram plots for state and parameters for noise level=0.15 mm (a) prior for state '*a*', (b) prior for parameter '*C*', (c) prior for parameter '*m*', (d) posterior for state '*a*' at the end of 72000 cycles, (e) posterior for parameter '*C*' at the end of 72000 cycles, and (f) posterior for parameter '*m*' at the end of 72000 cycles

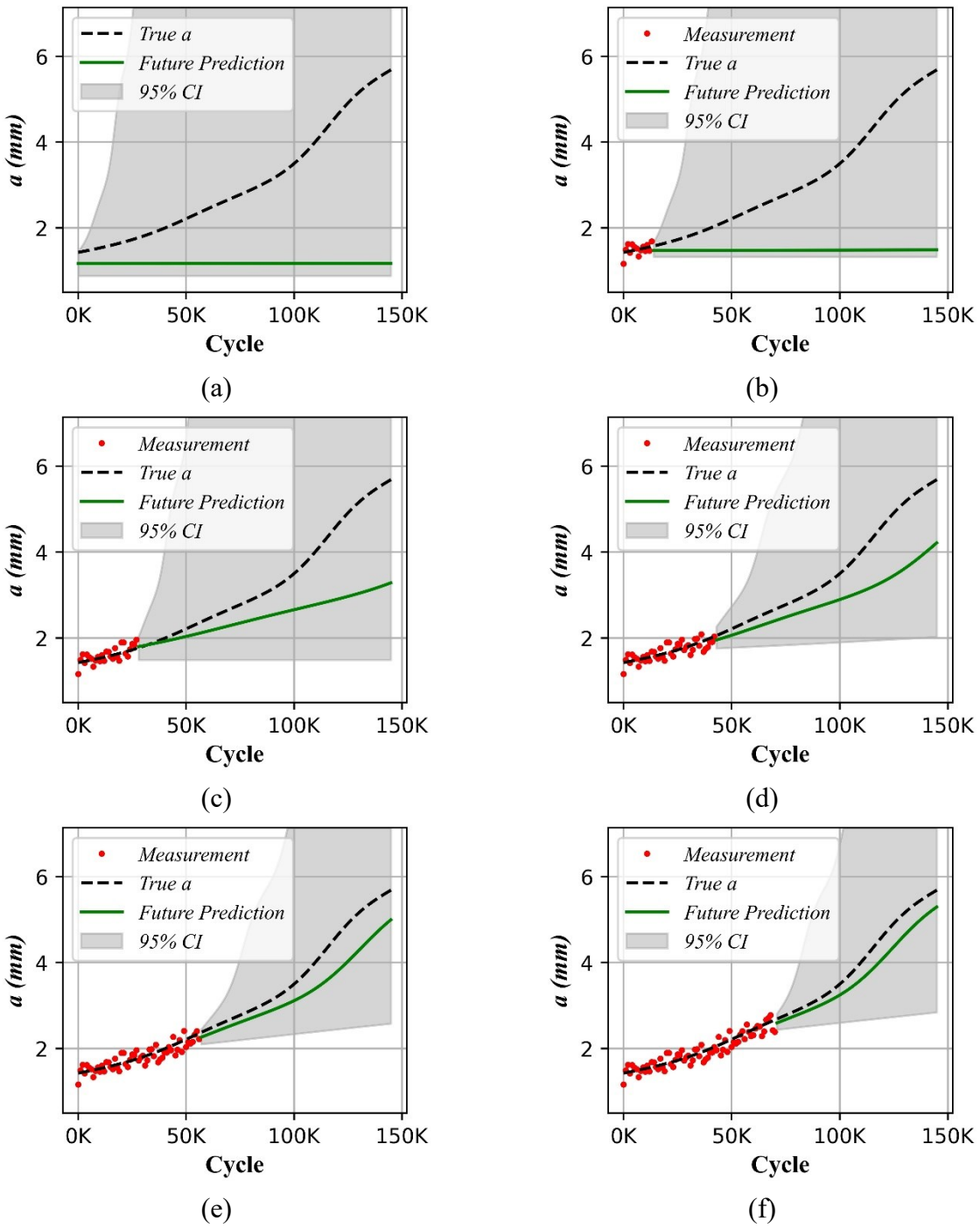

Figure 5-5: Future crack depth '*a*' prediction for noise level=0.15 mm when (a) No measurement data (with no observations), (b) Measurement data up to 15,000 cycles (with 16 observations), (c) Measurement data up to 29,000 cycles (with 30 observations), (d) Measurement data up to 44,000 cycles (with 45 observations), (e) Measurement data up to 58,000 cycles (with 59 observations), and (f) Measurement data up to 72, 000 cycles (with 73 observations)

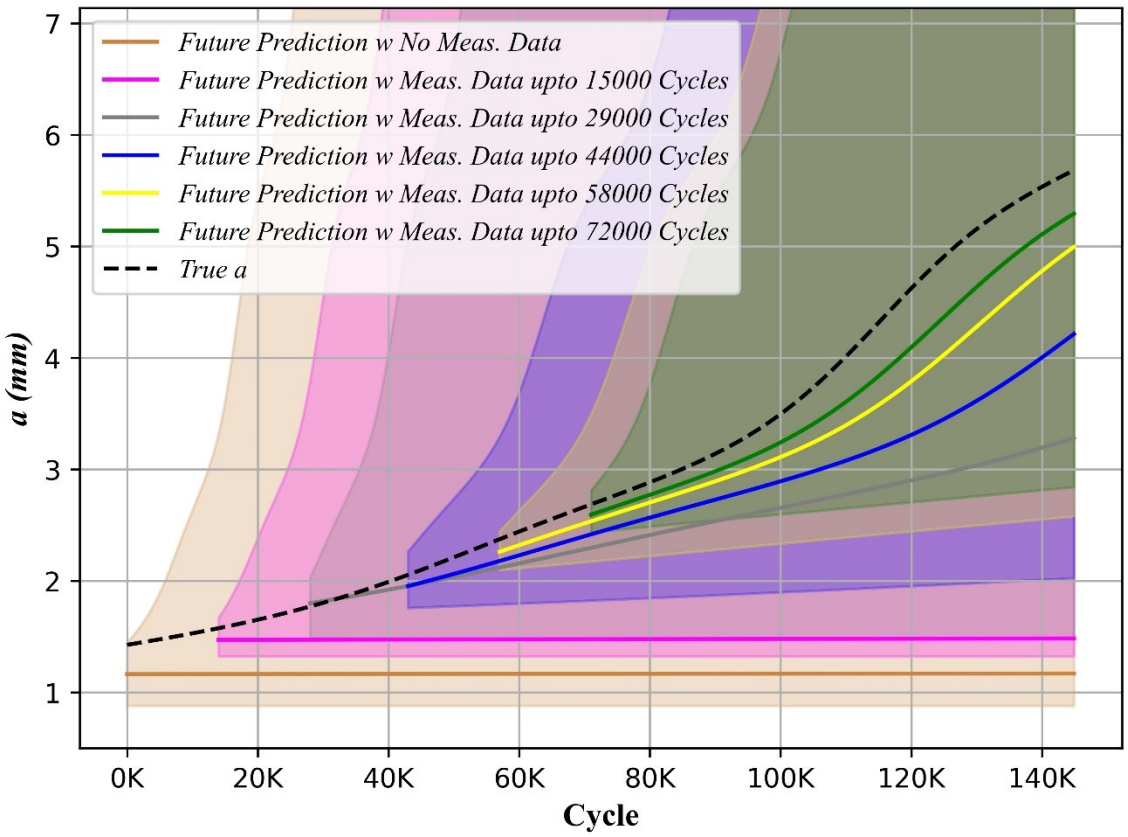

Figure 5-6: Future prediction of crack depth '*a*' at different time steps when different number of observations are available for noise level=0.15 mm

5.4.2.2 Case II: Noise level=0.30 mm

A priori for state and parameters are drawn from the distribution summarized in Table 5-4. The table also summarizes the probabilistic information for other parameters required for the tool, i.e. the assumed distributions for the measurement and process noise.

Table 5-4 Input data for Particle Filter for noise level=0.3 mm

a_0	$Normal\,(a_{\text{meas},0}, (12.5\% \times a_{\text{meas},0})^2)$ $= Normal(0.902, 0.112^2)$
C_0	$Uniform(125\% \times \log(C_{True}), 95\% \times \log(C_{True}))$ $= Uniform(-35.352, -26.874)$
m_0	$Uniform(0.65 \times m_{True}, 1.05 \times m_{True})$ $= Uniform(1.95, 3.15)$
v_a	$Normal(0, (167\% \times \sigma_{ILI})^2)$ $= Normal(0, 0.5^2)$
w_a, w_C, w_m	$Normal(0, (6.25\% \times \sigma_{ILI})^2), Normal(0, (10^{-2})^2), Normal(0, (10^{-2})^2)$ $= Normal(0, 0.018^2), Normal(0, (10^{-2})^2), Normal(0, (10^{-2})^2)$

Result and Discussion

The joint state-parameter estimation results are shown in Figure 5-7 for noise level of 0.30 mm. Figure 5-7 (a) presents the estimation results of the state variable, i.e., crack depth, with the available data up to 72000 cycles (corresponding to 73 observations, or 50% of the total data generated about 50% of the total generated data). Figure 5-7 (b) and (c) presents the updating histories of the two fatigue model parameters. It can be seen that, with the increase of crack size observations, better mean estimates of the two model parameters can be found and the associated variance is much lower in the model parameters. Figure 5-8 (a) - (c) shows histogram plot for state, and parameters for initial guesses or priors. Figure 5-8 (d) - (f) shows histogram plot for state, and parameters for posterior distribution, i.e. posterior is built incorporating measurement data available up to 72000 cycles. The execution time is approximately 185 seconds including the pseudo-data generation step.

The future prediction of crack depth *a* based upon the estimated state and updated model parameters at different time steps (related to load cycles here) is shown in Figure 5-9. Figure 5-9 (a) shows the fatigue crack growth prediction made based on initial values of the state and model parameters with no observation. Figure 5-9 (b) - (f) shows the fatigue crack growth predictions when observations are made up to 15000 cycles (with 16 observations), 29000 cycles (with 30 observations), 44000 cycles (with 45 observations), 58000 cycles (with 59 observations), and 72000 cycles (with 73 observations) respectively. It can be observed that the fatigue crack growth curve predicted purely based on the model without using measurement data is way off from the

truth, while when more measurement data is used, the prediction of the fatigue crack growth curve is closer and closer to the truth. At the same time, the uncertainty (or confidence interval) is much less when measurements are used. This trend can be seen in Figure 5-10, which contains a summary plot of these predicted trajectories at different time steps. The shaded areas in Figure 5-5 and Figure 5-10 represents region 95% confidence interval of each state and parameters, also the vertical axis of plots are limited to the wall thickness. 95% Confidence interval of the weighed mean of the state and parameters are calculated from the population of particles using 97.5 and 2.5 percentile. Table 5-5 summarizes the state-parameter estimation results at the end of available data i.e. 72000 cycles.

Table 5-5 State-Parameter estimation summary at the end of 72000 cycles with noise level=0.3 mm

State-Parameter	Mean	95 % Confidence Interval	
		Upper Limit	Lower Limit
a	2.640	2.923	2.361
Log(C)	-28.048	-27.237	-28.317
m	2.973	3.090	2.828

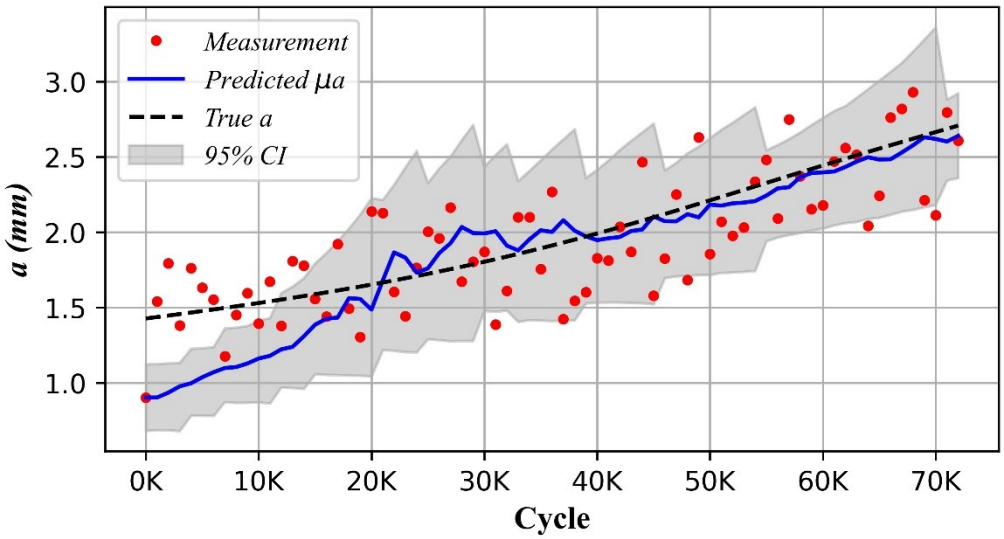

(a)

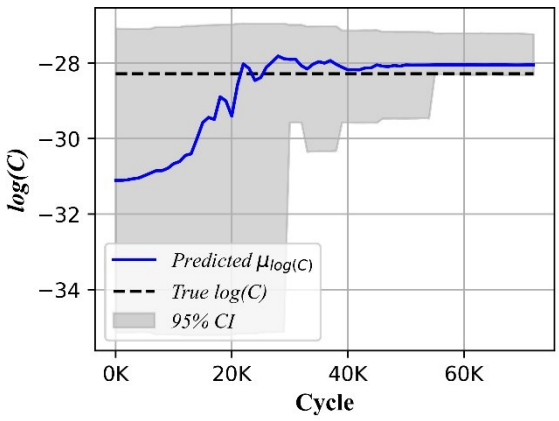

(b)

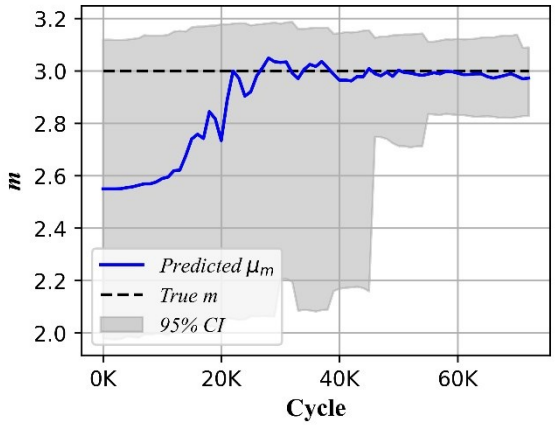

(c)

Figure 5-7: State-parameter estimation results with 95% confidence interval for noise level=0.3 mm (a) State (crack depth) '*a*' estimation, (b) Parameter '*C*' estimation, and (c) Parameter '*m*' estimation

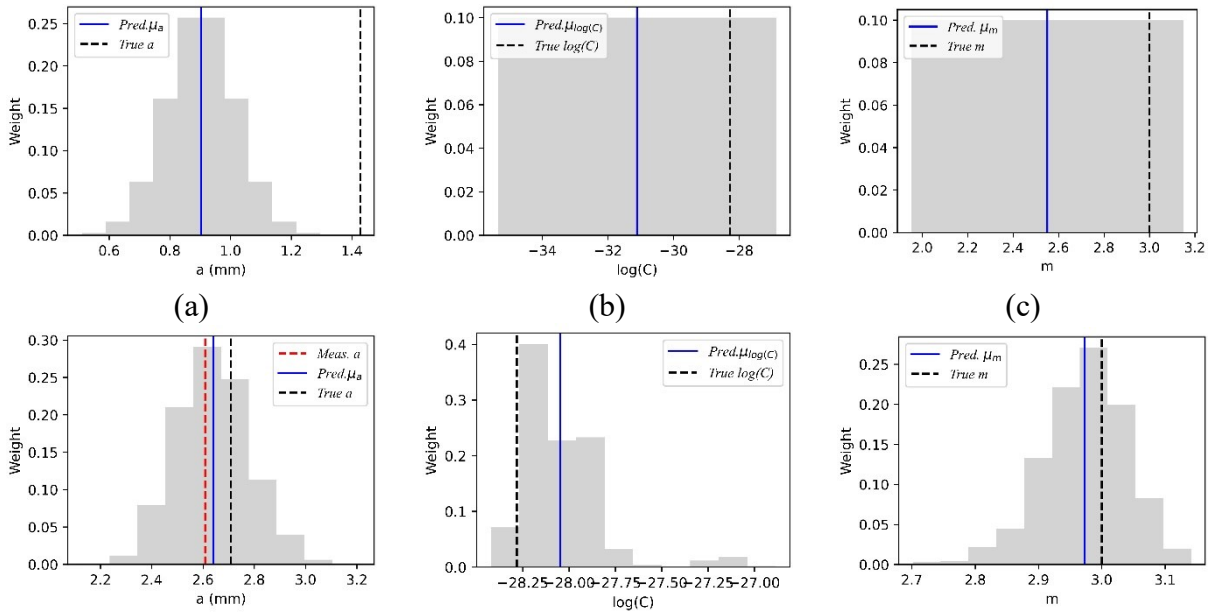

Figure 5-8: Histogram plots for state and parameters for noise level=0.3 mm (a) prior for state '*a*', (b) prior for parameter '*C*', (c) prior for parameter '*m*', (d) posterior for state '*a*' at the end of 72000 cycles, (e) posterior for parameter 'C' at the end of 72000 cycles, and (f) posterior for parameter 'm' at the end of 72000 cycles

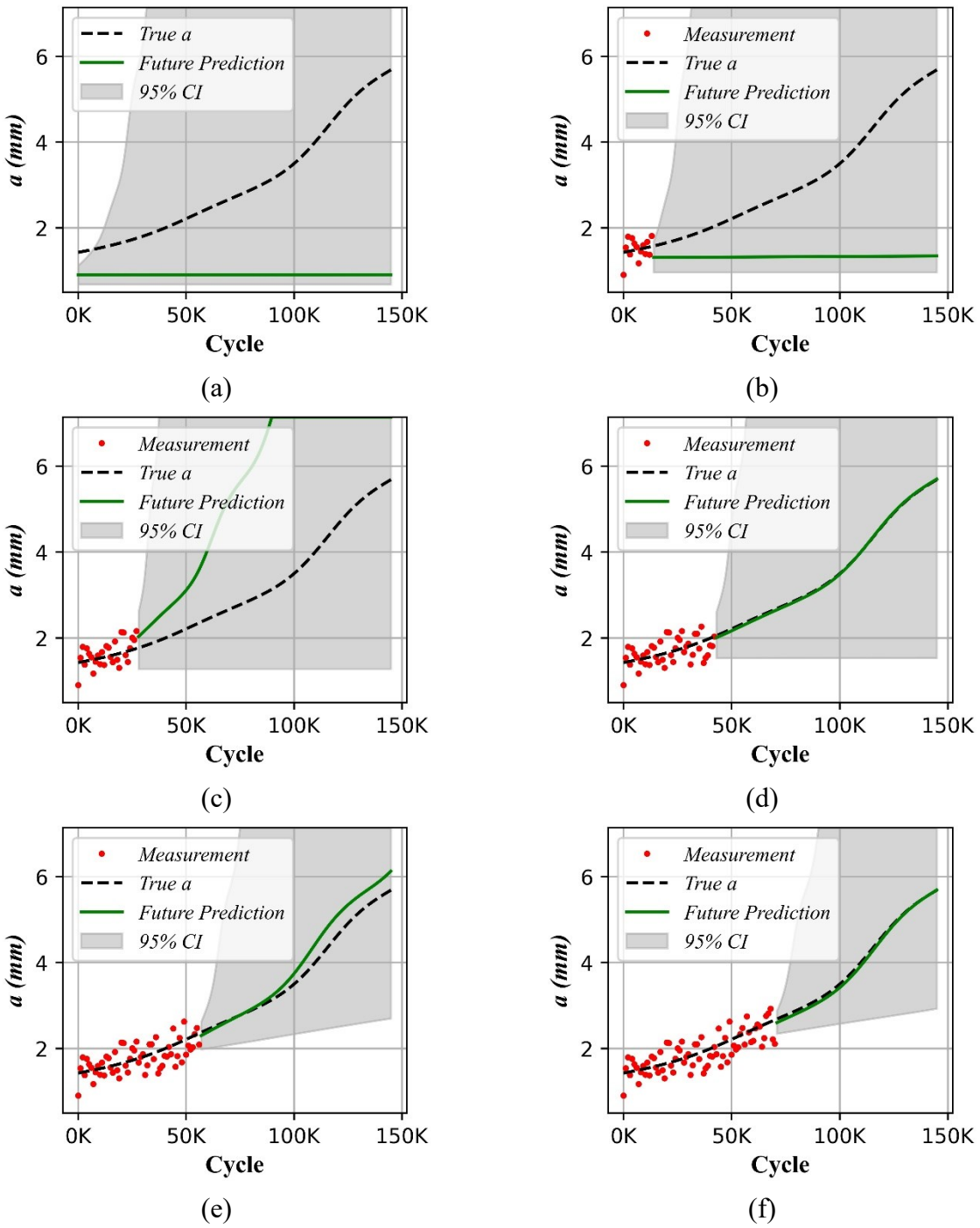

Figure 5-9: Future crack depth '*a*' prediction for noise level=0.15 mm when (a) No measurement data (with no observations), (b) Measurement data up to 15,000 cycles (with 16 observations), (c) Measurement data up to 29,000 cycles (with 30 observations), (d) Measurement data up to 44,000 cycles (with 45 observations), (e) Measurement data up to 58,000 cycles (with 59 observations), and (f) Measurement data up to 72, 000 cycles (with 73 observations)

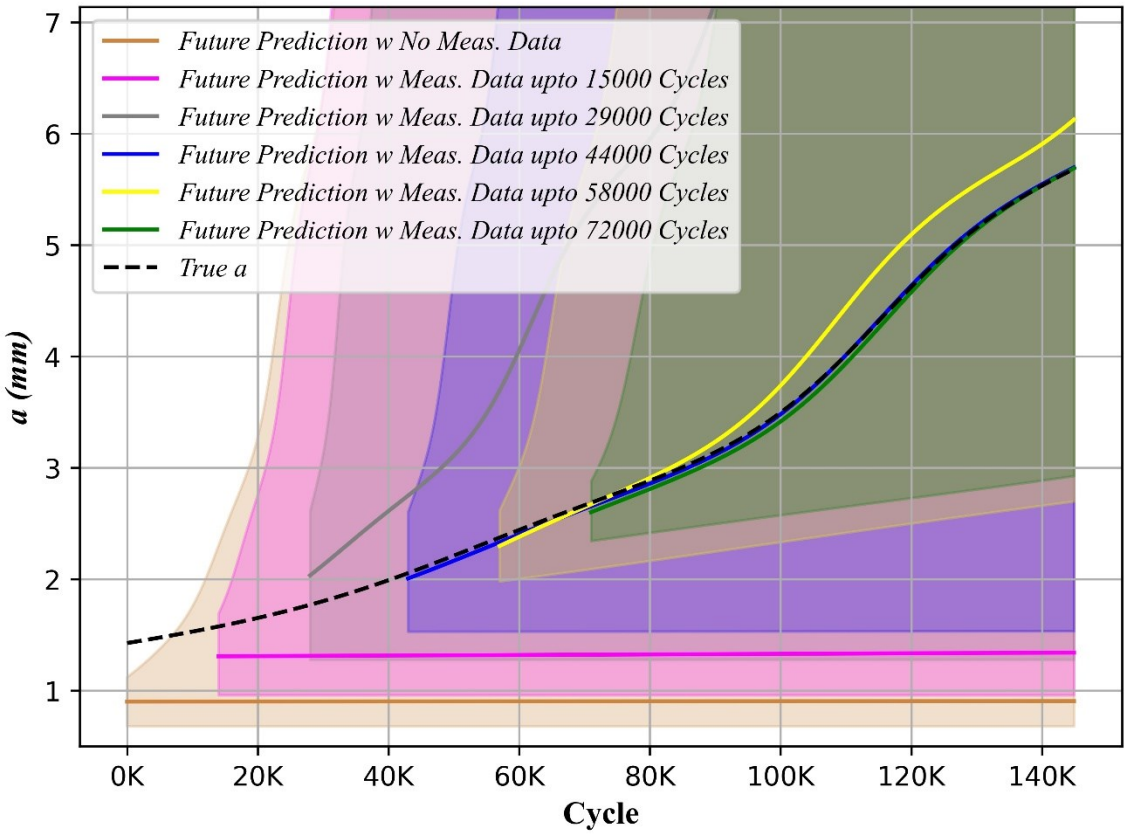

Figure 5-10: Future prediction of crack depth '*a*' at different time steps when different number of observations are available for noise level=0.3 mm

5.4.3 Simultaneous Estimation of Crack Depth (*a*), Half Crack Length (*c*) and Paris' Law Model Parameters (*C* and *m*) and Future Trajectory Prediction

Figure 5-11 shows a typical simulated true and noisy crack measurement data i.e. crack depth (*a*) and half crack length (*c*), with noise level=0.15 mm in both crack sizes. In the following cases too, 2000 sample points are drawn from the probability distribution for the state and model parameter variables and it is found reasonable accuracy can be achieved here. Latin hypercube sampling (LHS) technique is used in the following cases.

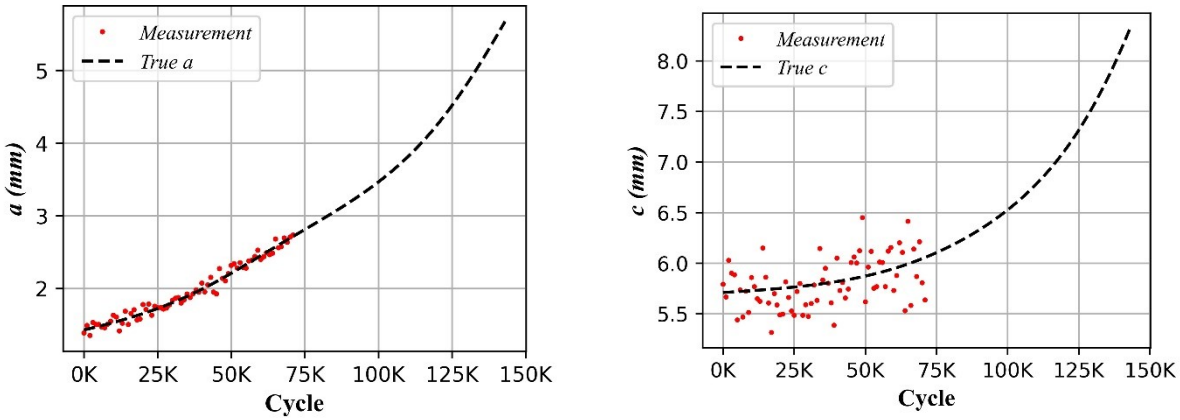

(a) (b)

Figure 5-11: Simulated data with noise (a) crack depth '*a*', and (b) half crack length '*c*'

5.4.3.1 Case I: Noise level=0.15

A priori for state and parameters are drawn from the distribution summarized in Table 5-6. The table also summarizes the probabilistic information for other parameters required for the tool, i.e. the assumed distributions for the measurement and process noise.

Table 5-6 Input data for Particle Filter for noise level=0.15 mm

a_0	$Normal\,(a_{\text{meas},0}, (12.5\% \times a_{\text{meas},0})^2)$ $= Normal(1.165, 0.145^2)$
c_0	$Normal\,(c_{\text{meas},0}, (12.5\% \times c_{\text{meas},0})^2)$ $= Normal(6.021, 0.752^2)$
C_0	$Uniform(125\% \times \log(C_{True}), 95\% \times \log(C_{True}))$ $= Uniform(-35.352, -26.867)$
m_0	$Uniform(65\% \times m_{True}, 105\% \times m_{True})$ $= Uniform(1.95, 3.15)$
v_a, v_c	$Normal(0, (167\% \times \sigma_{ILI})^2), Normal(0, (167\% \times \sigma_{ILI})^2$ $= Normal(0, 0.25^2), Normal(0, 0.25^2)$
w_a, w_c, w_C, w_m	$Normal(0, (6.25\% \times \sigma_{ILI})^2), Normal(0, (6.25\% \times \sigma_{ILI})^2), Normal(0, (10^{-2})^2), Normal(0, (10^{-2})^2)$ $= Normal(0, 0.009^2), Normal(0, 0.009^2), Normal(0, (10^{-2})^2), Normal(0, (10^{-2})^2)$

Results and Discussion

The joint state-parameter estimation results are shown in Figure 5-12 for noise level of 0.15 mm. Figure 5-12 (a) and (b) presents the estimation results of the states, i.e., crack depth '*a*' and half crack length '*c*', with the available data up to 71000 cycles (corresponding to 72 observations, or 50% of the total data generated about 50% of the total generated data). Figure 5-12 (c) and (d) presents the updating histories of the two fatigue model parameters. It can be seen that, with the increase of crack size observations, better mean estimates of the two model parameters can be found and the associated variance is much lower in the model parameters. Figure 5-13 (a) - (d) shows histogram plot for state, and parameters for initial guesses or priors. Figure 5-13 (e) - (h) shows histogram plot for state, and parameters for posterior distribution, i.e. posterior is built incorporating measurement data available up to 71000 cycles. The execution time is approximately 379 seconds including the pseudo-data generation step.

The future prediction of crack depth *a* based upon the estimated states and updated model parameters at different time steps (related to load cycles here) is shown in Figure 5-14. Figure 5-14 (a) shows the fatigue crack growth prediction made based on initial values of the state and model parameters with no observation. Figure 5-14 (b) - (f) shows the fatigue crack growth predictions when observations are made up to 14000 cycles (with 15 observations), 29000 cycles (with 30 observations), 43000 cycles (with 44 observations), 58000 cycles (with 59 observations), and 71000 cycles (with 72 observations) respectively. It can be observed that the fatigue crack growth curve predicted purely based on the model without using measurement data is way off from the truth, while when more measurement data is used, the prediction of the fatigue crack growth curve is closer and closer to the truth. At the same time, the uncertainty (or confidence interval) is much less when measurements are used. A similar kind of trend can be observed for crack length, the figures can be found in ANNEX-C. This trend can be seen in Figure 5-15 and Figure 5-16, which contains a summary plot of the predicted trajectories at different time steps for crack depth and half crack length respectively. The shaded areas in Figure 5-14, Figure 5-15, and Figure 5-16 represents region 95% confidence interval of each state and parameters, also the vertical axis of plots are limited to the wall thickness. Table 5-7 summarizes the state-parameter estimation results at the end of available data i.e. 71000 cycles.

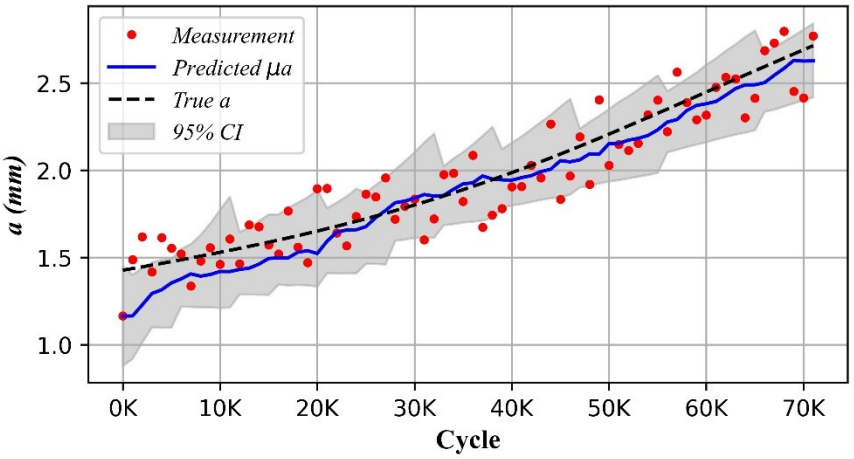

(a)

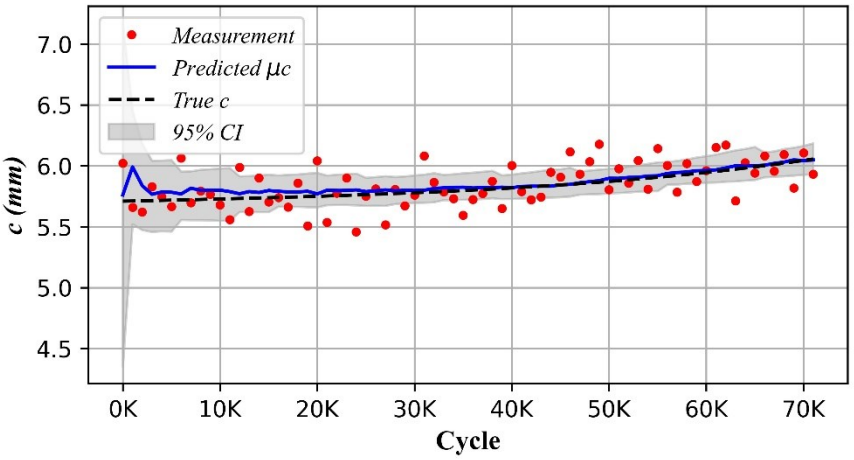

(b)

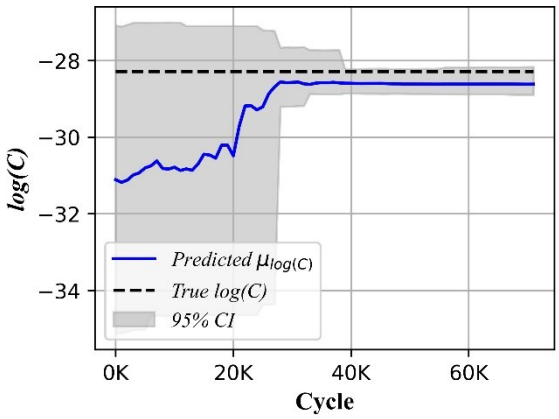

(c)

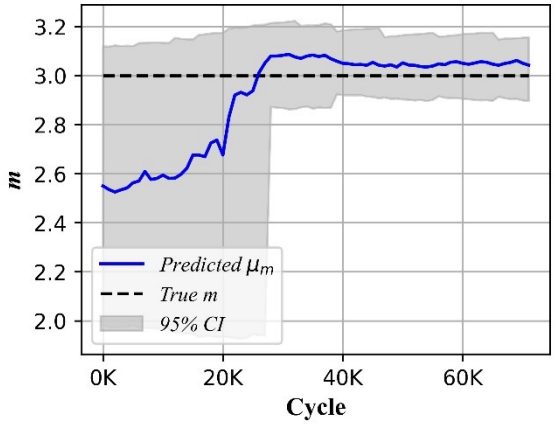

(d)

Figure 5-12: State-parameter estimation results with 95% confidence interval (a) State (crack depth) '*a*' estimation, (b) State (half crack length) '*c*', (c) Parameter '*C*' estimation, and (d) Parameter '*m*' estimation

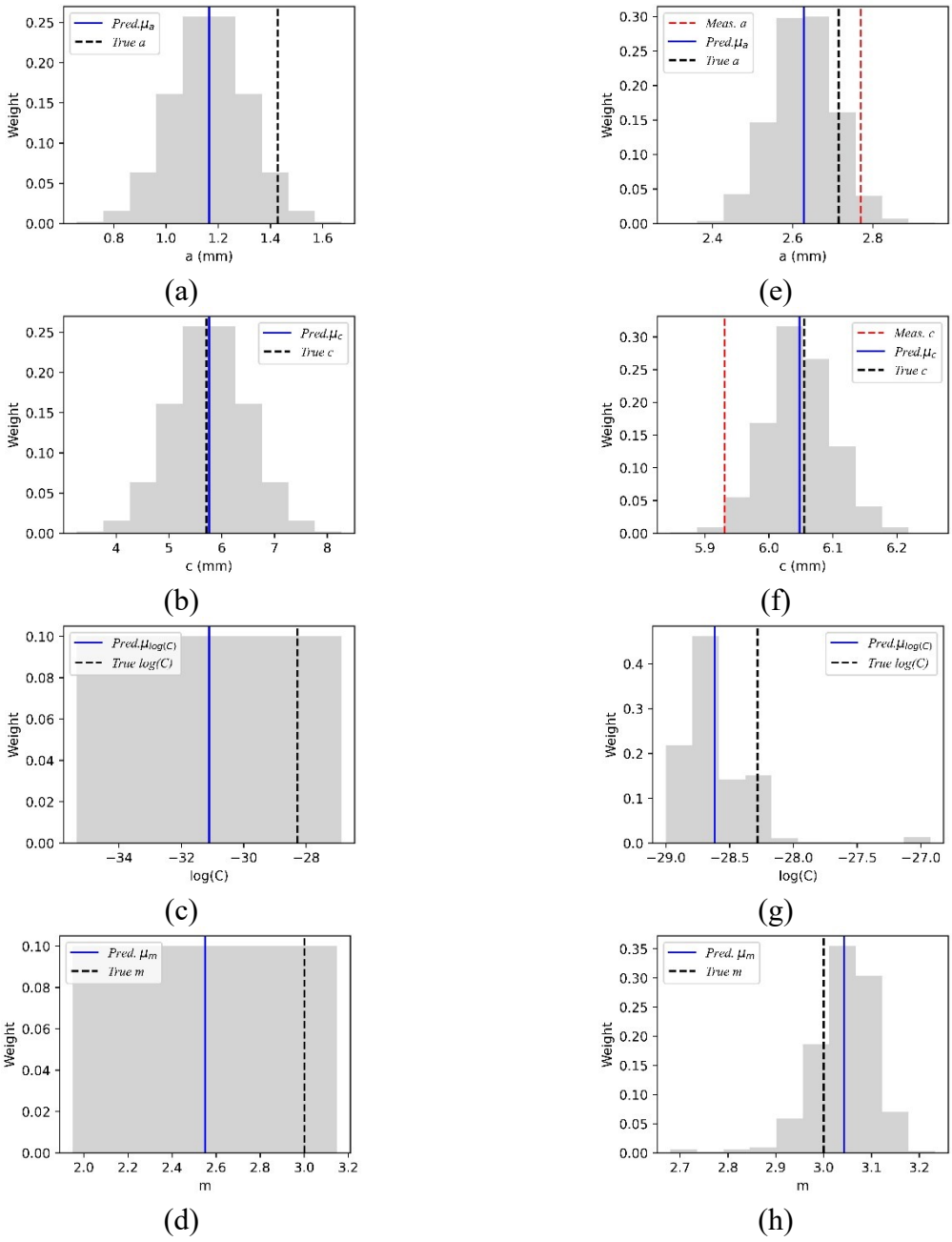

Figure 5-13: Histogram plots for state and parameters with noise level=0.15 mm (a) prior for state '*a*', (b) prior for state '*c*', (c) prior for parameter '*C*', (d) prior for parameter '*m*', (e) posterior for state 'a' at the end of 71000 cycles, (f) posterior for state 'c' at the end of 71000 cycles, (g) posterior for parameter '*C*' at the end of 71000 cycles, and (h) posterior for parameter '*m*' at the end of 71000 cycles

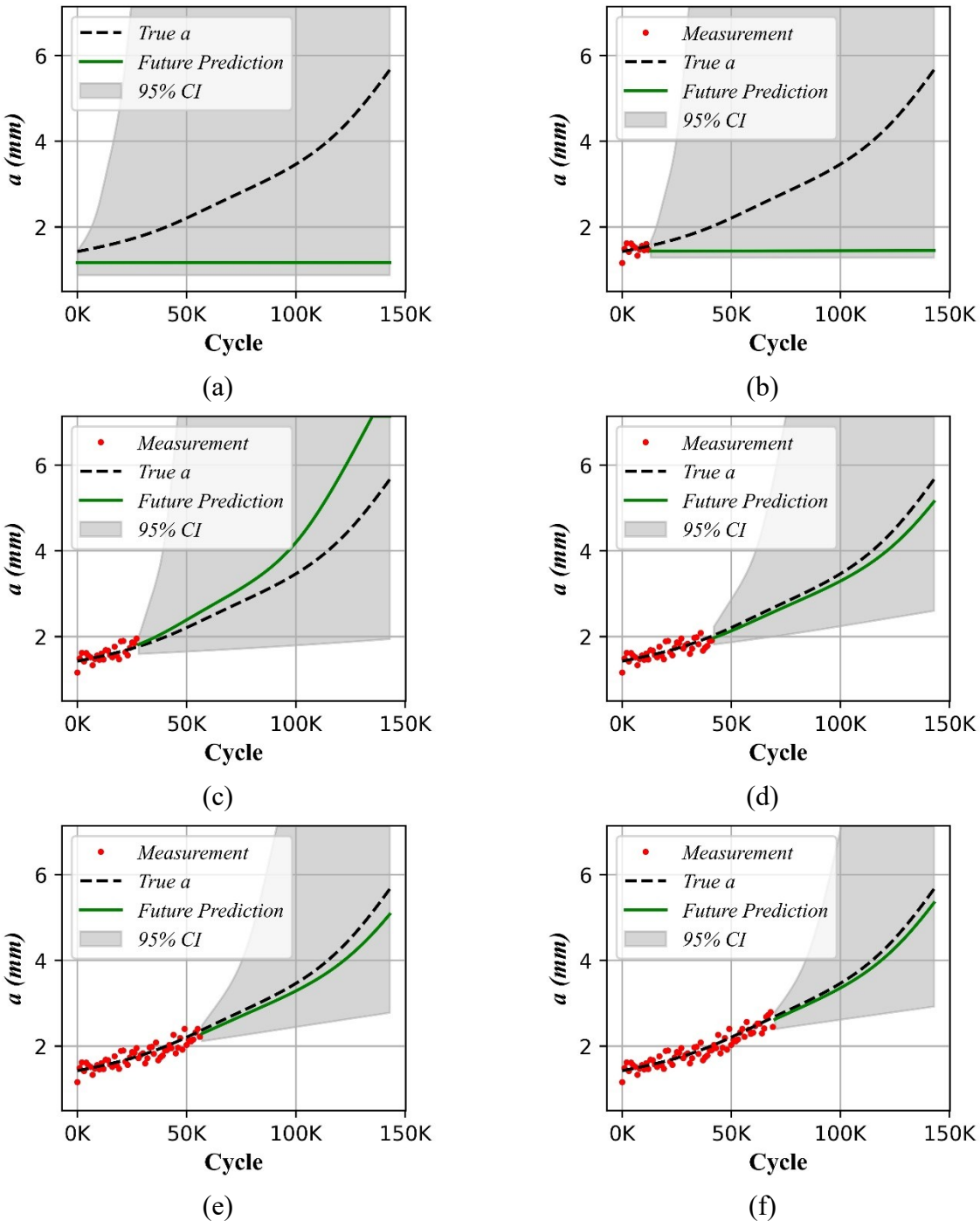

Figure 5-14: Future crack depth '*a*' prediction for noise level=0.15 mm when (a) No measurement data (with no observations), (b) Measurement data up to 14000 cycles (with 15 observations), (c) Measurement data up to 29000 cycles (with 30 observations), (d) Measurement data up to 43000 cycles (with 44 observations), (e) Measurement data up to 58000 cycles (with 59 observations), and (f) Measurement data up to 71000 cycles (with 72 observations)

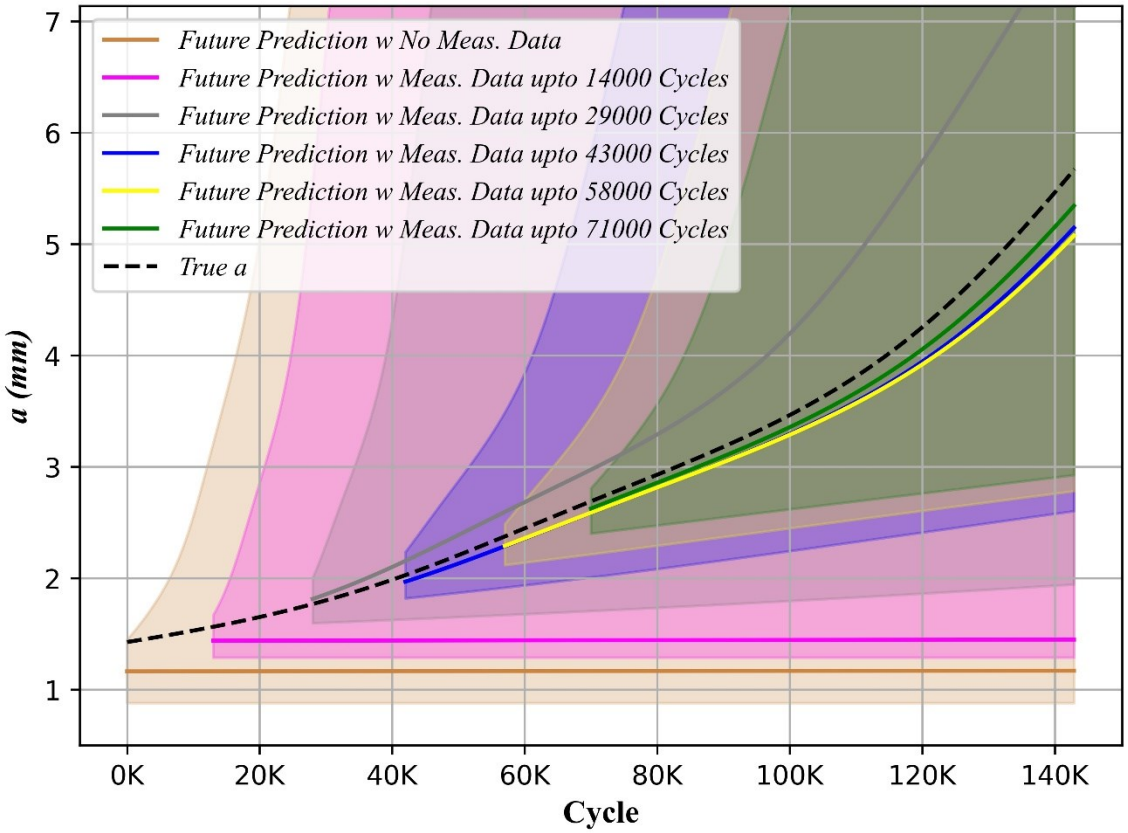

Figure 5-15: Future prediction of crack depth '*a*' at different time steps when different number of observations are available for noise level=0.15 mm

Table 5-7 State-Parameter estimation summary at the end of 71000 cycles with noise level=0.15 mm

State-Parameter	Mean	95 % Confidence Interval	
		Upper Limit	Lower Limit
a	2.627	2.843	2.419
c	6.048	6.185	5.932
Log(C)	-28.616	-28.164	-28.894
m	3.043	3.157	2.897

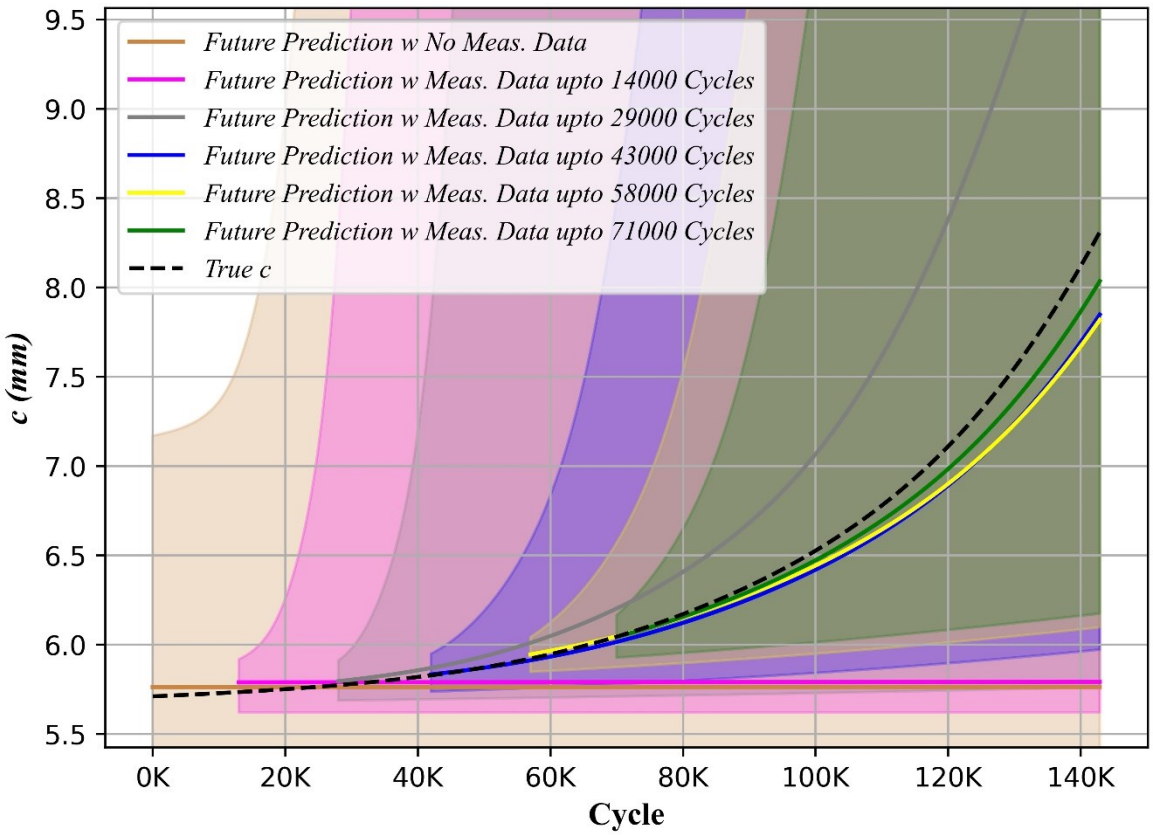

Figure 5-16: Future prediction of half crack length '*c*' at different time steps when different number of observations are available for noise level=0.15 mm

5.4.3.2 Case II: Noise level=0.3 mm

A priori for state and parameters are drawn from the distribution summarized in Table 5-8. The table also summarizes the probabilistic information for other parameters required for the tool, i.e. the assumed distributions for the measurement and process noise.

Table 5-8 Input data for Particle Filter for noise level=0.30 mm

a_0	$Normal\,(a_{\text{meas},0}, (12.5\% \times a_{\text{meas},0})^2)$ $= Normal(1.165, 0.145^2)$
c_0	$Normal\,(c_{\text{meas},0}, (12.5\% \times c_{\text{meas},0})^2)$ $= Normal(6.021, 0.752^2)$
C_0	$Uniform(125\% \times \log(C_{True}), 95\% \times \log(C_{True}))$ $= Uniform(-35.352, -26.867)$
m_0	$Uniform(65\% \times m_{True}, 105\% \times m_{True})$ $= Uniform(1.95, 3.15)$
v_a, v_c	$Normal(0, (167\% \times \sigma_{ILI})^2), Normal(0, (167\% \times \sigma_{ILI})^2$ $= Normal(0, 0.5^2), Normal(0, 0.5^2)$
w_a, w_c, w_C, w_m	$Normal(0, (8.33\% \times \sigma_{ILI})^2), Normal(0, (8.33\% \times \sigma_{ILI})^2), Normal(0, (10^{-2})^2), Normal(0, (10^{-2})^2)$ $= Normal(0, 0.025^2), Normal(0, 0.025^2), Normal(0, (10^{-2})^2), Normal(0, (10^{-2})^2)$

Results and Discussion

The joint state-parameter estimation results are shown in Figure 5-17 for noise level of 0.30 mm. Figure 5-17 (a) and (b) presents the estimation results of the states, i.e., crack depth '*a*' and half crack length '*c*', with the available data up to 71000 cycles (corresponding to 72 observations, or 50% of the total data generated about 50% of the total generated data). Figure 5-17 (c) and (d) presents the updating histories of the two fatigue model parameters. It can be seen that, with the increase of crack size observations, better mean estimates of the two model parameters can be found and the associated variance is much lower in the model parameters. Figure 5-18 (a) - (d) shows histogram plot for state, and parameters for initial guesses or priors. Figure 5-18 (e) - (h) shows histogram plot for state, and parameters for posterior distribution, i.e. posterior is built incorporating measurement data available up to 71000 cycles. The execution time is approximately 385 seconds including the pseudo-data generation step.

The future prediction of crack depth *a* based upon the estimated states and updated model parameters at different time steps (related to load cycles here) is shown in Figure 5-19. Figure 5-19 (a) shows the fatigue crack growth prediction made based on initial values of the state and model parameters with no observation. Figure 5-19 (b) - (f) shows the fatigue crack growth predictions when observations are made up to 14000 cycles (with 15 observations), 29000 cycles (with 30

observations), 43000 cycles (with 44 observations), 58000 cycles (with 59 observations), and 71000 cycles (with 72 observations) respectively. It can be observed that the fatigue crack growth curve predicted purely based on the model without using measurement data is way off from the truth, while when more measurement data is used, the prediction of the fatigue crack growth curve is closer and closer to the truth. At the same time, the uncertainty (or confidence interval) is much less when measurements are used. A similar kind of trend can be observed for crack length, the figures can be found in ANNEX-C. This trend can be seen in Figure 5-20 and Figure 5-21, which contains a summary plot of the predicted trajectories at different time steps for crack depth and half crack length respectively. The shaded areas in Figure 5-19 , Figure 5-20, and Figure 5-21 represents region 95% confidence interval of each state and parameters, also the vertical axis of plots are limited to the wall thickness. Table 5-9 summarizes the state-parameter estimation results at the end of available data i.e. 71000 cycles.

Table 5-9 State-Parameter estimation summary at the end of 71000 cycles with noise level=0.3 mm

State-Parameter	Mean	95 % Confidence Interval	
		Upper Limit	Lower Limit
a	2.584	2.991	2.203
c	6.080	6.371	5.835
Log(C)	-28.292	-26.928	-28.890
m	2.997	3.181	2.713

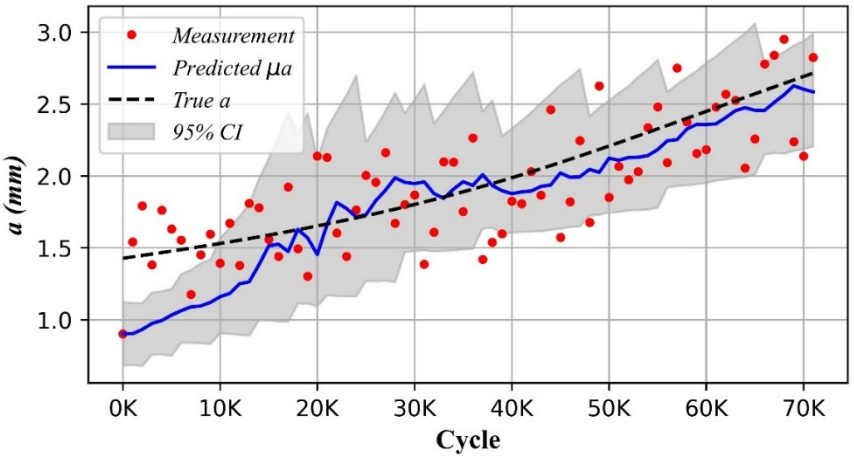

(a)

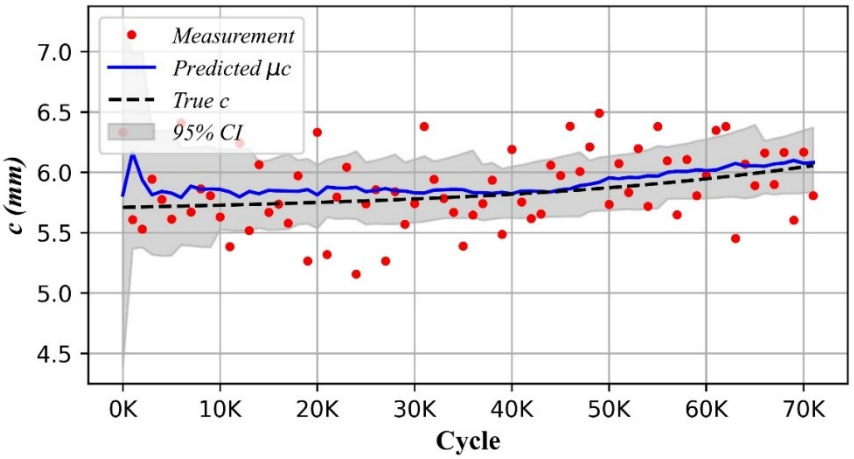

(b)

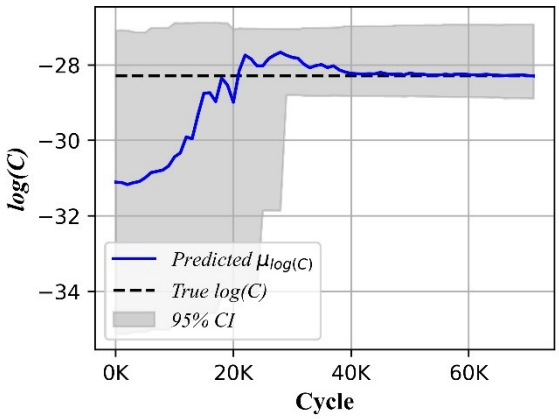

(c)

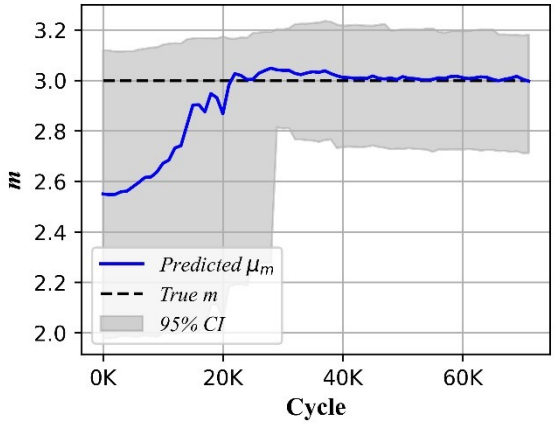

(d)

Figure 5-17: State-parameter estimation results with 95% confidence interval (a) State (crack depth) '*a*' estimation, (b) State (half crack length) '*c*', (c) Parameter '*C*' estimation, and (d) Parameter '*m*' estimation

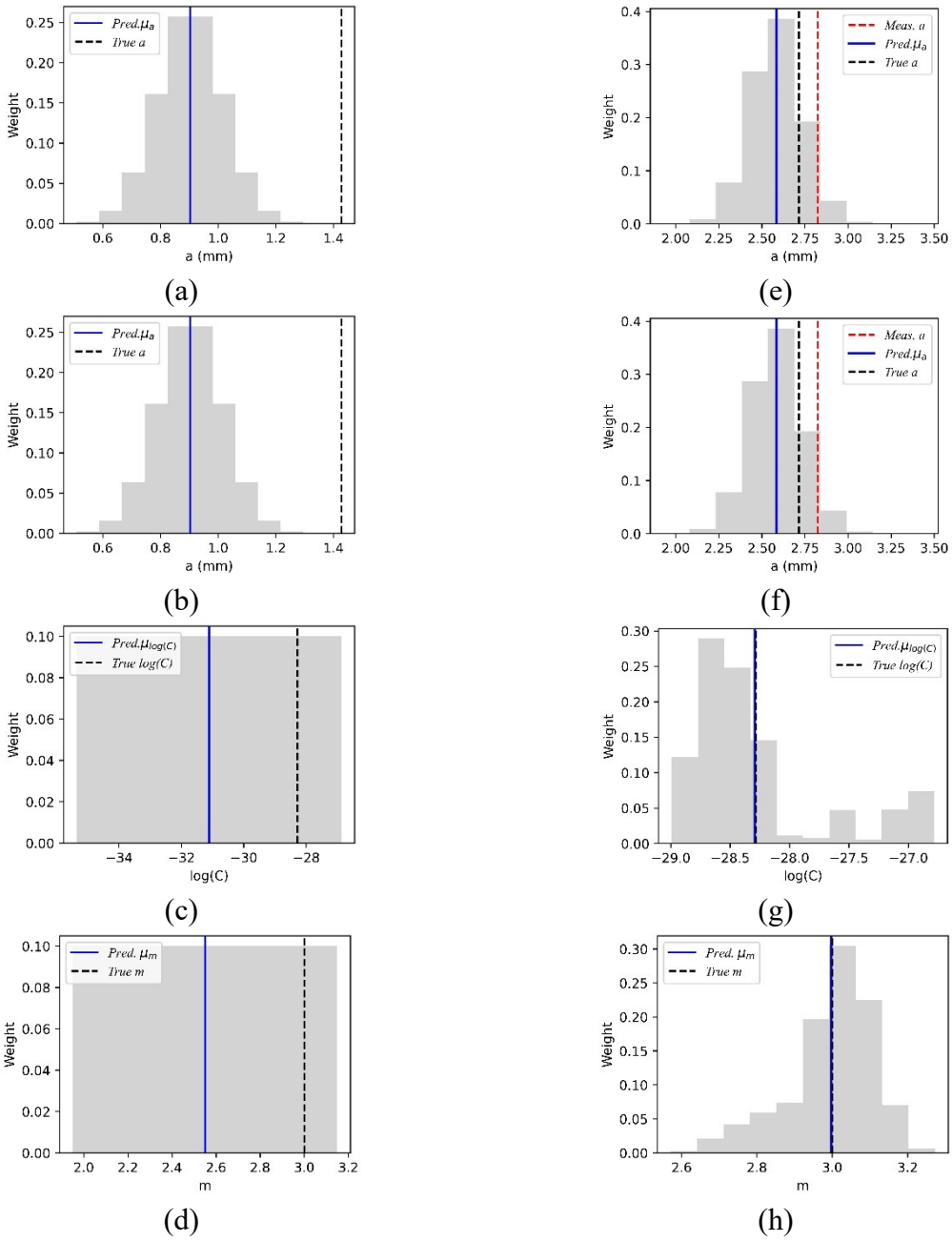

Figure 5-18: Histogram plots for state and parameters with noise level=0.30 mm (a) prior for state '*a*', (b) prior for state '*c*', (c) prior for parameter '*C*', (d) prior for parameter '*m*', (e) posterior for state '*a*' at the end of 71000 cycles, (f) posterior for state 'c' at the end of 71000 cycles, (g) posterior for parameter '*C*' at the end of 71000 cycles, and (h) posterior for parameter '*m*' at the end of 71000 cycles

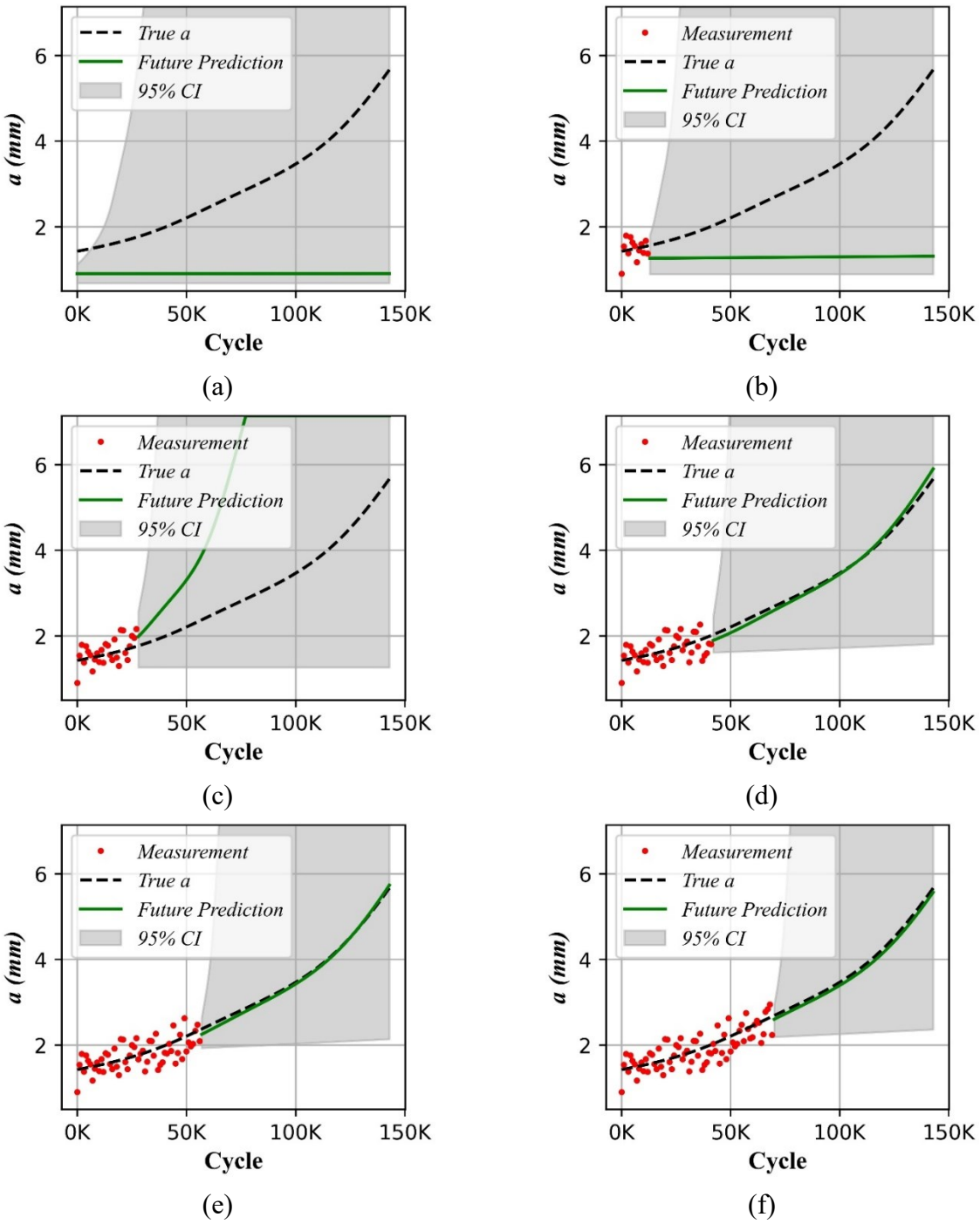

Figure 5-19: Future crack depth '*a*' prediction for noise level=0.3 mm when (a) No measurement data (with no observations), (b) Measurement data up to 14000 cycles (with 15 observations), (c) Measurement data up to 29000 cycles (with 30 observations), (d) Measurement data up to 43000 cycles (with 44 observations), (e) Measurement data up to 58000 cycles (with 59 observations), and (f) Measurement data up to 71000 cycles (with 72 observations)

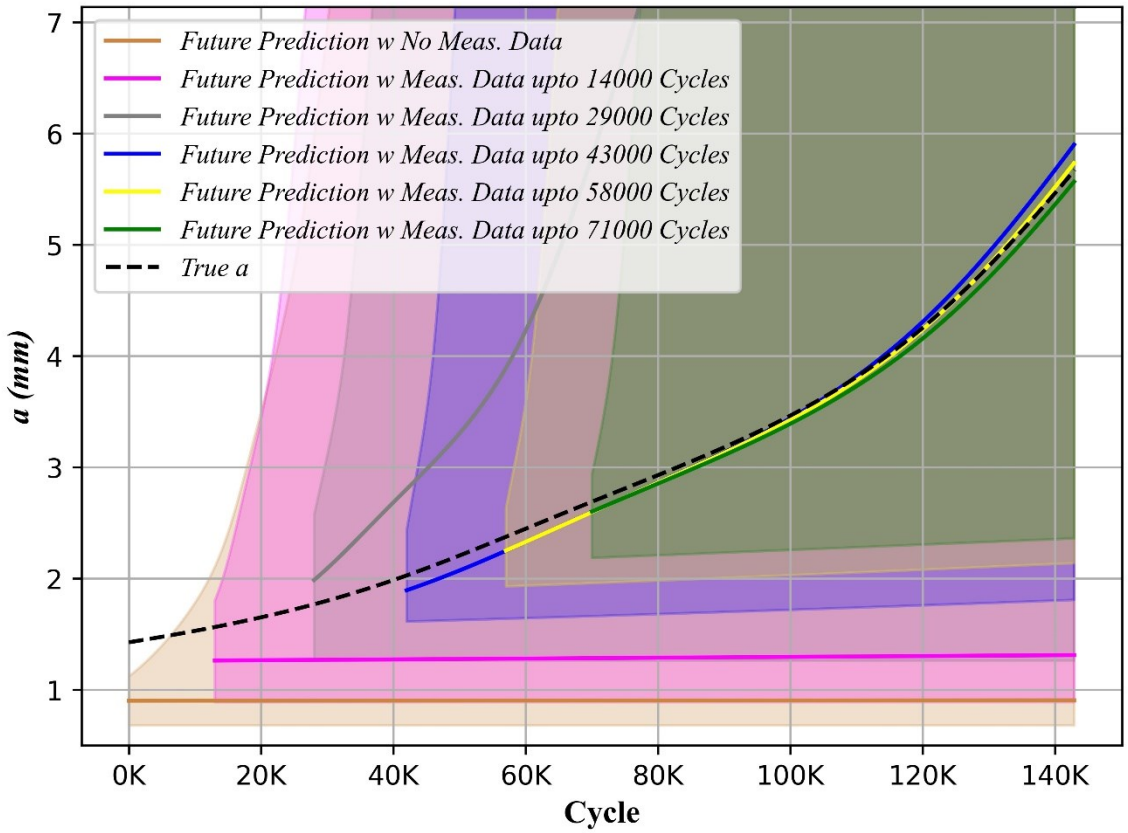

Figure 5-20: Future prediction of crack depth '*a*' at different time steps when different number of observations are available for noise level=0.3 mm

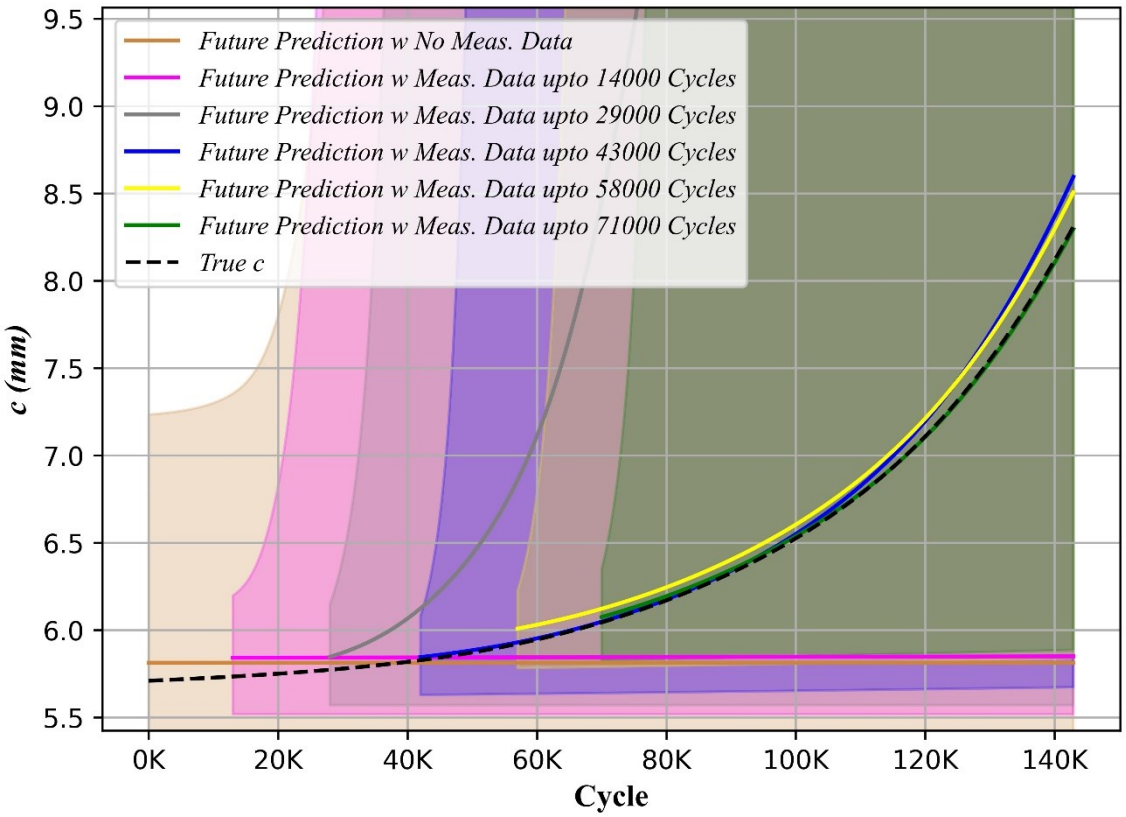

Figure 5-21: Future prediction of half crack length '*c*' at different time steps when different number of observations are available for noise level=0.3 mm

For the case studies presented with different noise levels, the overall performance of the developed tool was found to be good with optimum set of tool parameters: (a) system model uncertainty, and (b) measurement model uncertainty. Table 5-10 summarizes the optimum set of values of system and measurement model uncertainty relative to the ILI tool measurement uncertainty along with the number of particles generated.

Table 5-10 Optimum tool parameters for generated pseudo dataset

ILI-tool Noise level	System model uncertainty (w)				Measurement model uncertainty (v)		# of particles
σ_{ILI}	σ_a	σ_c	$\sigma_{log(C)}$	σ_m	σ_a	σ_c	
0.15 mm	6.25% σ_{ILI}	-	10^{-2}	10^{-2}	167% σ_{ILI}	-	2000
0.3 mm	6.25% σ_{ILI}	-	10^{-2}	10^{-2}	167% σ_{ILI}	-	2000
0.15 mm	6.25% σ_{ILI}	6.25% σ_{ILI}	10^{-2}	10^{-2}	167% σ_{ILI}	167% σ_{ILI}	2000
0.3 mm	8.33% σ_{ILI}	8.33% σ_{ILI}	10^{-2}	10^{-2}	167% σ_{ILI}	167% σ_{ILI}	2000

5.5 Summary

In this chapter stochastic filtering technique specifically Particle Filter is introduced. Particle Filter is a Monte Carlo based algorithms that relies on repeated random sampling to obtain numerical results to solve filtering problems. The fundamental concept of PF is based on Bayesian approach, where posterior distribution is obtained by multiplying likelihood function with the prior distribution. Using the recursive estimation technique proposed in this method, the prior knowledge about the crack growth is leveraged with the measurement data. Compared to the purely model-based prediction of crack growth, this method provides a way to calibrate the model parameters using measurements when data become available. More importantly, the noisy measurement data can be filtered with the use of model for more reliable estimate of the crack size. Note in this study, the analytical model API 579 model is used for SIF prediction. However, with the increase in computational capabilities, more accurate fatigue crack growth prediction models (e.g., XFEM-based) covering wider range of crack and pipe geometry than that in API 579 can be potentially used in this method for joint state-parameter estimation.

A python based tool is developed to couple Particle Filter, fatigue crack growth model Paris' law and GPR model in order to provide a probabilistic estimate of current crack sizes or states and model parameters. The tool incorporates the noisy measurement data from ILI tools and updates the belief of the current crack sizes along with the model parameters. Noisy measurement data and physics-based model were coupled to extract the best possible estimate. As more data becomes

available the estimate gets more reliable even for increasing noise levels. Performance of the Particle Filter depends greatly on the various parameters like noise level in tool, and confidence in the model. Measurement noise from tool are specified by the vendors which is fixed. However, the confidence in the model depends on how closely it relates to the physical phenomenon like fatigue crack growth. An optimum set of these parameters leads to a good performing Particle Filter. For the pseudo dataset generated using different noise levels the developed FCG tool performed reasonably good when system model uncertainty was around 6.25% of the ILI tool uncertainty. The measurement model uncertainty was tuned to make the tool flexible and value of 1.67 times the ILI tool uncertainty was found to be good enough.

The current crack size estimated and model parameters updated were used in the fatigue growth model (i.e., Paris law) to predict the future trajectory of the fatigue crack growth. The tool developed has shown to be promising for fatigue crack growth prediction when a fracture mechanics-based model and measurement data are both utilized, though when noise level is high, more measurements are expected.

CHAPTER 6: CONCLUSIONS AND RECOMMENDATIONS

6.1 Summary

Fatigue crack growth is one of the main pipeline integrity threats. Once a crack is detected in a pipeline by the operator while performing ILI or any other non-destructive testing, taking timely proactive or predictive maintenance can be beneficial. In addition to fatigue crack measurements, fracture mechanics-based approach can be used to simulate the crack size with time and thus be used to predict the potential fatigue crack growth.

In order to monitor and manage fatigue crack growth, Paris' law is widely used in pipeline industry. Paris' law requires reliable values of stress intensity factor and fatigue model parameters. In this study, numerical method XFEM was explored for reliable estimation of SIF. The XFEM model was compared with conventional FEM and very good agreement between both numerical methods was found. Furthermore, industry practiced API 579 model, which provides an analytical solution in a tabular format with the need of interpolation for estimating SIF. API 579 model was also compared against the numerical method to check it's accuracy. Good agreement was achieved between API 579 model and the numerical results from FEM or XFEM.

A surrogate model developed based on Gaussian Process Regression was used as an alternate method to estimate SIF over high-fidelity FE models. The training and testing data set was obtained from API 579 model, as it provides good accuracy when compared with FEM and XFEM models as shown in this study. The computation time and accuracy of the GPR model makes it a very good alternative to API 579 model for SIF calculation, i.e., performing interpolation based Gaussian Process Regression.

A python based tool to couple the surrogate model for estimation of SIF, PF and Paris' law was developed. PF provides a probabilistic estimate of current crack size and model parameters based on the noisy ILI measurement data and Paris' law model. Once the crack size and model parameters were estimated, they were used in Paris' law to provide a probabilistic estimate of the future fatigue crack growth trajectory. The performance of the tool was found to be reliable with the optimum set of parameters.

6.2 Conclusions

The main conclusions that can be drawn from this study are listed below:

i. XFEM has proven to be a reliable method for different type of crack propagation analysis with appropriate set of parameters. Furthermore, XFEM was used for estimation of stress intensity factor and very good agreement was found between results from conventional FEM and API 579 model.
    a. FEM requires a crack confirming mesh and wedge type of elements for better accuracy. Mesh size of 0.125 mm – 0.25 mm along the crack front and around the crack tip was found to produce reliable values of SIF.
    b. In XFEM crack can be modeled independent of the crack geometry with a general meshing strategy, but a mesh structure confirming to the shape of crack geometry provides better accuracy. Mesh size of 0.125 mm – 0.25 mm produces good results when focused type mesh was used.
    c. General meshing strategy in XFEM required mesh size of 0.02 mm around the crack tip, which is about one fifth of that required when using focused type meshing strategy. Mesh size 0.125 mm – 0.25 mm along crack front was sufficient. Selection of using either focused type or general type of meshing strategy depends on the user. Evaluating time and effort for mesh design versus the actual computational power required in solving the problem is recommended.
    d. The adequate number of contours around the crack tip was found to be five for computational efficiency. After ignoring first two contours, the average of requested contours could be used for reliable SIF calculation. Enrichment radius of at least one element size ahead of the crack tip, which was 0.125 mm, could provide stable SIF values.

ii. Gaussian process regression-based surrogate model is developed for SIF calculation. The model is based on the training data set from validated API 579 model and provides a reliable and quick estimate which is used further in stochastic filter.
    a. Matern 3/2 was found to be the best kernel function based on the grid search performed using five-fold cross-validation with five repetitions.

iii. Leveraging the physical model and available data from ILI tools can lead to more confident estimate of the crack size from the noisy measurement and better estimate of the fatigue parameters. This is proved to be achievable by using stochastic filtering technique, i.e., Particle Filter, which can provide a probabilistic estimate of the model parameters and current crack size. The updated information about the current crack size and fatigue model parameters can be further utilized to make probabilistic estimate of the future fatigue crack growth trajectory. As more data becomes available, the estimate gets better. If tool error is large, more data can be used to filter out the measurement noise to a certain degree, thus more accurate information about the crack size.

   a. Pseudo datasets were generated in this study using Paris' law for a pipeline section with semi-elliptical crack on the outer surface and adding Gaussian white noise with standard deviation of 0.15 mm and 0.3 mm for performance validation of the FCG tool. System model uncertainty of about one-sixteenth of the ILI tool and measurement model uncertainty of 1.67 times the ILI tool were found to be optimum set of FCG tool parameters.

6.3 Recommendations for Future Work

The work carried out in this research project contributed mainly towards (1) the verification of existing standard code of practice for fatigue crack driving parameter in a pipeline, (2) SIF estimation using relatively new numerical method XFEM, (3) a surrogate model to provide a robust and computationally efficient tool for SIF calculation, and to the end, (4) a stochastic filtering tool using Particle Filter to estimate the fatigue crack growth model parameters and current crack size, along with the uncertainty related to the estimation to provide a probabilistic estimate of the future fatigue crack growth trajectory. However, due to limitations in this study, there still remains room for further development in the following aspects, to name a few,

i. The fatigue crack growth parameter based on LEFM was used in this study and material were assumed to be linear elastic. There remains a direction of investigation towards use of elastic-plastic material properties and hence EPFM based fatigue crack growth. Capabilities of XFEM for fatigue crack growth modeling for elastic-plastic materials also needs to be considered.

ii. The surrogate model developed were based on GPR models. There are many other surrogate modeling technique that cam be further explored like Artificial Neural Network (ANN), Support Vector Machine (SVM). The training points generated were based on verified models from standard practise. As mentioned previously the further capabilities of XFEM for elastic-plastic materials can be utilized to generate data-points and expand to the elastic-plastic material properties domain.

iii. The Particle Filter was used for estimating model parameters and crack size from a mimicked pseudo-data with Gaussian white noise. Further investigation is required using actual ILI data.

RFERENCES

[1] CEPA. *About pipelines*. 2020 [cited 2020 August 12]; Available from: https://www.aboutpipelines.com/en/pipeline-101/pipeline-facts/.

[2] Government of Canada. *Pipelines Across Canada*. 2020 [cited 2021 2021-12-01]; Available from:https://www.nrcan.gc.ca/our-natural-resources/energy-sources-distribution/clean-fossil-fuels/pipelines/pipelines-across-canada/18856.

[3] Candian Energy Pipeline Association (CEPA). *Hisotry of Pipelines*. 2021 [cited 2021 2021-12-01]; Available from: https://www.aboutpipelines.com/pipeline-101/pipeline-history/.

[4] Song, P., D. Lawrence, S. Keane, S. Ironside, and A. Sutton. *Pressure cycling monitoring helps ensure the integrity of energy pipelines*. in *International Pipeline Conference*. 2010.

[5] Board, N.T.S., *Pipeline Accident Brief, TransCanada Corporation Pipeline (Keystone Pipeline) Rupture Amherst, South Dakota*. 2018, National Transportation Safety Board.

[6] Mohammed Al-Rabeeah, N.A.A.-O., and Nauman Tehsin. *Stress Corrosion Cracking (SCC) Susceptibility Screening Enhancement*. 2020 2020-11-30 [cited 2021 2021-12-01]; Available from: https://www.pipeline-journal.net/articles/stress-corrosion-cracking-scc-susceptibility-screening-enhancement.

[7] Price, R., *Pipeline Inspection and Repair – Dents.* COPEX 2014, 2014.

[8] Engineer. *7 Types of Pipeline Mechanical Damage*. 2021 [cited 2021 2021-12-01]; Available from: https://engineer-m.com/mechanical-damages/.

[9] Semiga, V., C. Bonneau, S. Tiku, A. Eshraghi, and A. Dinovitzer, *Fatigue Considerations for Natural Gas Transmission Pipelines.* BMT Fleet Technology Limited, The Interstate Natural Gas Association of America (INGAA), 2016.

[10] API, R., *579: Recommended Practice for Fitness for Service.* American Petroleum Institute, 2016.

[11] ASME, *Managing System Integrity of Gas Pipelines*, in *Managing System Integrity of Gas Pipelines*. 2018.

[12] Khan, F., R. Yarveisy, and R. Abbassi, *Risk-based pipeline integrity management: a road map for the resilient pipelines.* Journal of Pipeline Science and Engineering, 2021.

[13] Rosen Group. *Pipeline Cracks*. 2021 [cited 2021 2021-12-08]; Available from: https://www.rosen-group.com/global/solutions/services/pipeline-cracks.

[14] Kiefner, J.F., C.E. Kolovich, P.A. Zelenak, and T. Wahjudi. *Estimating Fatigue Life for Pipeline Integrity Management*. in *International Pipeline Conference*. 2004.

[15] National Energy Board, *Fatigue Crack Failure Associated With Shallow Dents on Pipelines* N.E. Board, Editor. 2010. p. 3.

[16] Zhang, Y., M. Fan, Z. Xiao, and W. Zhang, *Fatigue analysis on offshore pipelines with embedded cracks.* Ocean Engineering, 2016. **117**: p. 45-56.

[17] Tiku, S., A. Dinovitzer, V. Semiga, M. Piazza, and T. Jones. *Improvement of Pipeline Fatigue Life Estimation*. in *International Pipeline Conference*. 2016. American Society of Mechanical Engineers.

[18] Semiga, V., S. Tiku, A. Dinovitzer, and W. Wagster. *Evaluation of Fatigue in Gas Pipelines*. in *International Pipeline Conference*. 2016. American Society of Mechanical Engineers.

[19] Singh, N., S. Das, P. Song, and N. Yoosef-Ghodsi, *Numerical Investigation of Pressure-Cycling-Induced Fatigue Failure of Wrinkled Energy Pipelines.* Journal of Offshore Mechanics and Arctic Engineering, 2022. **144**(1).

[20] Cheng, Y.F., *Stress corrosion cracking of pipelines*. 2013: John Wiley & Sons.

[21] Leis, B. and R. Eiber. *Stress-corrosion cracking on gas-transmission pipelines: history, causes, and mitigation*. in *Proceedings of First International Business Conference on Onshore Pipelines, Berlin*. 1997.

[22] Jaske, C.E. and J.A. Beavers. *Review and proposed improvement of a failure model for SCC of pipelines*. in *International Pipeline Conference*. 1998. American Society of Mechanical Engineers.

[23] Association, C.E.P., *Stress Corrosion Cracking: Recommended Practices.* SCC Working Group, Canada. 2nd Edition, December, 2007.

[24] Xie, M., *Pipeline Defect Growth Prediction and Risk-based Integrity Management.* 2019.

[25] Ossai, C.I., *Advances in asset management techniques: An overview of corrosion mechanisms and mitigation strategies for oil and gas pipelines.* International Scholarly Research Notices, 2012. **2012**.

[26] Owston, R. and D. McKeon. *Formulation and Experimental Validation of a New Erosion Flow Model*. in *International Pipeline Conference*. 2016. American Society of Mechanical Engineers.

[27] Tang, X., L. Xu, and Y.F. Cheng. *A Fundamental Understanding of Erosion-Corrosion of Hydrotransport Pipes in Oil Sands Slurry*. in *International Pipeline Conference*. 2008.

[28] Michael Baker Jr., *Mechanical Damage*. 2009.

[29] Zarea, M., R. Batisse, B. Leis, P. Cardin, and G. Vignal. *Full scale experimental database of dent and gouge defects to improve burst and fatigue strength models of pipelines*. in *International Pipeline Conference*. 2012. American Society of Mechanical Engineers.

[30] Seevam, P., C. Lyons, P. Hopkins, and M. Toft. *Modelling of dent and gouges, and the effect on the failure probability of pipelines*. in *International Pipeline Conference*. 2008.

[31] Jager, E., R. Kuik, G. Stallenberg, and J. Zanting. *The influence of land use and depth of cover on the failure rate of gas transmission pipelines*. in *International Pipeline Conference*. 2002.

[32] Gholami, H., S. Shahrooi, and M. Shishehsaz, *Strain-based fatigue life analysis of pipelines with external defects under cyclic internal pressure.* The Journal of Strain Analysis for Engineering Design, 2020: p. 0309324720957569.

[33] Giunta, G., F. Dionigi, A. Bassan, M. Veneziani, G. Bernasconi, S. Del Giudice, D. Rovetta, R. Schiavon, and F. Zanon. *Third party interference and leak detection on buried pipelines for reliable transportation of fluids*. in *Offshore Mediterranean Conference and Exhibition*. 2011. OnePetro.

[34] El-Hussein, S., J.J. Harrigan, and A. Starkey. *Finite element simulation of guided waves in pipelines for long range monitoring against third party attacks*. in *Journal of Physics: Conference Series*. 2015. IOP Publishing.

[35] Azevedo, T.F., W.R.V. Sampaio, E.C.B. Câmara, G.D. Lima, W.F. dos Santos Silva, and S. da Silva Ramos, *Failure analysis of a sugarcane loader rear shaft.* Engineering Failure Analysis, 2020. **109**: p. 104326.

[36] Campbell, F.C., *Fatigue and fracture: understanding the basics*. 2012: ASM International.

[37] Veritas, D.N. and G. Lloyd, *Fatigue design of offshore steel structures.* DNV Recommended Practice DNV-RP-C203, 2010.

[38] Gerhard Knauf, M.E.-P., Ulrich Marewski, Oskar Reepmeyer, *Internal Pressure Fatigue of Pipes, Pipelines and Cylinders*, in *International Symposium of Microalloyed Steels for the Oil and Gas Industry*, P.B. W. J. Fazackerley, K. Hulka and F. Siciliano, Editor. 2007. p. 499-512.

[39] Coffin Jr, L. and R. Fritz, *Thermal stress and thermal stress fatigue.* Liquid Metal Handbook, US AEC TID-5277, 1955: p. 204.

[40] Smith, R., P. Watson, and T. Topper, *A stress-strain parameter for the fatigue of metals.* Journal of Materials, 1970. **5**(4): p. 767-778.

[41] Paris, P. and F. Erdogan, *A critical analysis of crack propagation laws.* Journal of Basic Engineering, 1963. **85**: p. 528-533.

[42] BS, B.S., *Guidance on methods for assessing the acceptability of flaws in metallic structures.* British Standards Institution, 2015.

[43] Jaske, C.E. *Assessment of pipeline fatigue crack-growth life*. in *International Pipeline Conference*. 2006.

[44] Silva, J., *Fatigue Crack Growth in Steel used in Oil and Gas Pipelines.* 2011.

[45] Tiku, S., M. Ghovanlou, A. Dinovitzer, M. Piazza, and T. Jones. *Full Scale Test Validation of Fatigue Crack Growth Rate of Flaws in ERW Pipe*. in *International Pipeline Conference*. 2020. American Society of Mechanical Engineers.

[46] Anderson, T.L., *Fracture mechanics: fundamentals and applications*. 2005: CRC press.

[47] McGinty, B. *Fracture Mechanics*. 2014 [cited 2021 4/23/2021]; Available from: https://www.fracturemechanics.org/modes123.html.

[48] Lin, M., S. Agbo, D.-M. Duan, J.R. Cheng, and S. Adeeb, *Simulation of crack propagation in API 5L X52 pressurized pipes using XFEM-based cohesive segment approach.* Journal of Pipeline Systems Engineering and Practice, 2020. **11**(2): p. 04020009.

[49] Blackman, B., H. Hadavinia, A.J. Kinloch, and J. Williams, *The use of a cohesive zone model to study the fracture of fibre composites and adhesively-bonded joints.* International journal of fracture, 2003. **119**(1): p. 25-46.

[50] Haddad, M. and K. Sepehrnoori. *Integration of XFEM and CZM to model 3D multiple-stage hydraulic fracturing in quasi-brittle shale formations: solution-dependent propagation direction*. in *Proceedings of the AADE National Technical Conference and Exhibition, AADE2015, San Antonio, Texas*. 2015.

[51] Hillerborg, A., M. Modéer, and P.-E. Petersson, *Analysis of crack formation and crack growth in concrete by means of fracture mechanics and finite elements.* Cement and concrete research, 1976. **6**(6): p. 773-781.

[52] Wells, G.N. and L. Sluys, *A new method for modelling cohesive cracks using finite elements.* International Journal for numerical methods in engineering, 2001. **50**(12): p. 2667-2682.

[53] Shim, D.-J., M. Uddin, F. Brust, and G. Wilkowski. *Cohesive zone modeling of ductile crack growth in circumferential through-wall-cracked pipe tests*. in *Pressure Vessels and Piping Conference*. 2011.

[54] Chanda, S. and C. Ru. *Cohesive zone model for temperature dependent fracture analysis of pipeline steel*. in *Proceedings of 25th Canadian congress on applied mechanics*. 2015.

[55] Wang, Y. and C. Ru, *Determination of two key parameters of a cohesive zone model for pipeline steels based on uniaxial stress-strain curve.* Engineering Fracture Mechanics, 2016. **163**: p. 55-65.

[56] Belytschko, T. and T. Black, *Elastic crack growth in finite elements with minimal remeshing.* International journal for numerical methods in engineering, 1999. **45**(5): p. 601-620.

[57] Agbo, S., M. Lin, I. Ameli, A. Imanpour, D.-M. Duan, J.R. Cheng, and S. Adeeb. *Evaluation of the Effect of Internal Pressure and Flaw Size on the Tensile Strain Capacity of X42 Vintage Pipeline Using Damage Plasticity Model in Extended Finite Element Method (XFEM)*. in *Pressure Vessels and Piping Conference*. 2019. American Society of Mechanical Engineers.

[58] Lin, M., S. Agbo, J.R. Cheng, N. Yoosef-Ghodsi, and S. Adeeb. *Application of the extended finite element method (XFEM) to simulate crack propagation in pressurized steel pipes*. in *Pressure Vessels and Piping Conference*. 2017. American Society of Mechanical Engineers.

[59] Okodi, A., M. Lin, N. Yoosef-Ghodsi, M. Kainat, S. Hassanien, and S. Adeeb, *Crack propagation and burst pressure of longitudinally cracked pipelines using extended finite*

element method. International Journal of Pressure Vessels and Piping, 2020. **184**: p. 104115.

[60] Abaqus, V., *6.14 Documentation.* Dassault Systemes Simulia Corporation, 2014. **651**: p. 6.2.

[61] Kim, Y. and W. Hwang, *High-cycle, low-cycle, extremely low-cycle fatigue and monotonic fracture behaviors of low-carbon steel and its welded joint.* Materials, 2019. **12**(24): p. 4111.

[62] Xiao, Z., W. Zhang, Y. Zhang, M. Fan, Z. Xiao, W. Zhang, Y. Zhang, and M. Fan, *Fatigue investigations on steel pipeline containing 3D coplanar and non-coplanar cracks.* CMC-COMPUTERS MATERIALS & CONTINUA, 2020. **62**(1): p. 267-280.

[63] El Fakkoussi, S., H. Moustabchir, A. Elkhalfi, and C. Pruncu, *Computation of the stress intensity factor KI for external longitudinal semi-elliptic cracks in the pipelines by FEM and XFEM methods.* International Journal on Interactive Design and Manufacturing (IJIDeM), 2019. **13**(2): p. 545-555.

[64] Coêlho, G.d.C., A.A. Silva, M.A. dos Santos, and N.C. dos Santos, *The use of XFEM for stress intensity factor estimation of surface cracks.* CEP, 2017. **58015**: p. 435.

[65] Mora, D.F. and M. Niffenegger, *A new simulation approach for crack initiation, propagation and arrest in hollow cylinders under thermal shock based on XFEM.* Nuclear Engineering and Design, 2021: p. 111582.

[66] Olamide, A., A. Bennecer, and S. Kaczmarczyk, *Finite Element Analysis of Fatigue in Offshore Pipelines with Internal and External Circumferential Cracks.* Applied Mechanics, 2020. **1**(4): p. 193-223.

[67] Sudret, B., *Meta-models for structural reliability and uncertainty quantification.* arXiv preprint arXiv:1203.2062, 2012.

[68] Yang, H. and A. Wang, *Dynamic stability analysis of pipeline based on reliability using surrogate model.* Journal of Marine Engineering & Technology, 2013. **12**(2): p. 75-84.

[69] Hassanien, S., M. Kainat, S. Adeeb, and D. Langer. *On the use of surrogate models in reliability-based analysis of dented pipes*. in *International Pipeline Conference*. 2016. American Society of Mechanical Engineers.

[70] Xie, M., S. Bott, A. Sutton, A. Nemeth, and Z. Tian, *An integrated prognostics approach for pipeline fatigue crack growth prediction utilizing inline inspection data.* Journal of Pressure Vessel Technology, 2018. **140**(3).

[71] Loghin, A. and S. Ismonov, *Application of Response Surface Method in Probabilistic Fatigue Crack Propagation Life Assessment using 3D FEA.* Procedia Structural Integrity, 2020. **28**: p. 2304-2311.

[72] Hombal, V. and S. Mahadevan, *Surrogate modeling of 3D crack growth.* International journal of fatigue, 2013. **47**: p. 90-99.

[73] Keprate, A., R.C. Ratnayake, and S. Sankararaman, *Adaptive Gaussian process regression as an alternative to FEM for prediction of stress intensity factor to assess fatigue degradation in offshore pipeline.* International Journal of Pressure Vessels and Piping, 2017. **153**: p. 45-58.

[74] Keprate, A., R.C. Ratnayake, and S. Sankararaman. *Comparing different metamodelling approaches to predict stress intensity factor of a semi-elliptic crack*. in *International Conference on Offshore Mechanics and Arctic Engineering*. 2017. American Society of Mechanical Engineers.

[75] Salemi, M. and H. Wang, *Fatigue life prediction of pipeline with equivalent initial flaw size using Bayesian inference method.* Journal of Infrastructure Preservation and Resilience, 2020. **1**(1): p. 1-15.

[76] Leser, P.E., J.D. Hochhalter, J.E. Warner, J.A. Newman, W.P. Leser, P.A. Wawrzynek, and F.-G. Yuan, *Probabilistic fatigue damage prognosis using surrogate models trained via*

three-dimensional finite element analysis. Structural Health Monitoring, 2017. **16**(3): p. 291-308.

[77] Jang, Y.-Y., N.-S. Huh, I.-J. Kim, C.-M. Kim, and Y.-P. Kim. *Application of Artificial Neural Network to Multi-Variables Regression for Estimations of J-Integral for Surface Cracked Pipes*. in *Pressure Vessels and Piping Conference*. 2020. American Society of Mechanical Engineers.

[78] Keprate, A. and R.C. Ratnayake. *Using gradient boosting regressor to predict stress intensity factor of a crack propagating in small bore piping*. in *2017 IEEE International Conference on Industrial Engineering and Engineering Management (IEEM)*. 2017. IEEE.

[79] Hoffman, W.M., M.E. Riley, and B.W. Spencer. *Surrogate model development and validation for reliability analysis of reactor pressure vessels*. in *Pressure Vessels and Piping Conference*. 2016. American Society of Mechanical Engineers.

[80] Xie, M. and Z. Tian, *A review on pipeline integrity management utilizing in-line inspection data.* Engineering Failure Analysis, 2018. **92**: p. 222-239.

[81] Kim, N.-H., D. An, and J.-H. Choi, *Prognostics and health management of engineering systems*. Switzerland: Springer International Publishing. 2017.

[82] Feng, Q., R. Li, B. Nie, S. Liu, L. Zhao, and H. Zhang, *Literature review: Theory and application of in-line inspection technologies for oil and gas pipeline girth weld defection.* Sensors, 2017. **17**(1): p. 50.

[83] Phlipot, J., S. Rapp, D. Whaley, K. Spencer, and D. Williams. *Overcoming Challenges of EMAT Inline Inspection Validation for SCC Management in Natural Gas Pipelines: A Practical Approach*. in *International Pipeline Conference*. 2020. American Society of Mechanical Engineers.

[84] Katz, D., S. Potts, T. Beuker, J. Grillenberger, and R. Weber. *EMAT As a Basis for a Comprehensive System Wide Crack Management Program*. in *International Pipeline Conference*. 2018. American Society of Mechanical Engineers.

[85] Cadini, F., E. Zio, and D. Avram, *Monte Carlo-based filtering for fatigue crack growth estimation.* Probabilistic Engineering Mechanics, 2009. **24**(3): p. 367-373.

[86] Wang, H.-K., R. Haynes, H.-Z. Huang, L. Dong, and S.N. Atluri, *The use of high-performance fatigue mechanics and the extended Kalman/particle filters, for diagnostics and prognostics of aircraft structures.* CMES: Computer Modeling in Engineering & Sciences, 2015. **105**(1): p. 1-24.

[87] Robinson, E.I., J. Marzat, and T. Raïssi. *Model-based prognosis algorithms with uncertainty propagation: Application to fatigue crack growth*. in *2016 3rd Conference on Control and Fault-Tolerant Systems (SysTol)*. 2016. IEEE.

[88] Liu, X., Y. Jia, Z. He, and L. Sun, *Hybrid residual fatigue life prediction approach for gear based on Paris law and particle filter with prior crack growth information.* Journal of Vibroengineering, 2017. **19**(8): p. 5908-5919.

[89] Yang, W., S. Yuan, and J. Chen, *Application of deterministic resampling particle filter to fatigue prognosis.* Journal of Vibroengineering, 2017. **19**(8): p. 5978-5991.

[90] Liu, X., W. Zhang, X. Liu, W. Dai, and G. Fu, *A novel RLS-KS method for parameter estimation in particle filtering-based fatigue crack growth prognostics.* IEEE Access, 2019. **7**: p. 156764-156778.

[91] Doucet, A. and V.B. Tadić, *Parameter estimation in general state-space models using particle methods.* Annals of the institute of Statistical Mathematics, 2003. **55**(2): p. 409-422.

[92] Ray, A. and S. Tangirala, *Stochastic modeling of fatigue crack dynamics for on-line failure prognostics.* IEEE Transactions on Control Systems Technology, 1996. **4**(4): p. 443-451.

[93] Moussas, V. and S. Katsikas. *A multi-model approach to fatigue crack growth monitoring and prediction*. in *12th Int. Workshop on Systems, Signals & Image Processing, Chalkida, Greece*. 2005.

[94] Cobb, A.C., J.E. Michaels, and T.E. Michaels. *Experimental verification of a Kalman filter approach for estimating the size of fastener hole fatigue cracks*. in *Health Monitoring of Structural and Biological Systems 2008*. 2008. International Society for Optics and Photonics.

[95] Wang, Y., N. Binaud, C. Gogu, C. Bes, and J. Fu, *Determination of Paris' law constants and crack length evolution via Extended and Unscented Kalman filter: An application to aircraft fuselage panels.* Mechanical Systems and Signal Processing, 2016. **80**: p. 262-281.

[96] Yiwei, W., G. Christian, N. Binaud, B. Christian, and F. Jian, *A model-based prognostics method for fatigue crack growth in fuselage panels.* Chinese Journal of Aeronautics, 2019. **32**(2): p. 396-408.

[97] Chen, Y., J. Castiglione, R. Astroza, and Y. Li, *Parameter estimation of resistor-capacitor models for building thermal dynamics using the unscented Kalman filter.* Journal of Building Engineering, 2021. **34**: p. 101639.

[98] Astroza, R., N. Barrientos, Y. Li, E.I.S. Flores, and Z. Liu, *Bayesian updating of complex nonlinear FE models with high-dimensional parameter space using heterogeneous measurements and a batch-recursive approach.* Engineering Structures, 2019. **201**: p. 109724.

[99] Li, Z., X. Jiang, and H. Hopman, *Surface Crack Growth in Offshore Metallic Pipes under Cyclic Loads: A Literature Review.* Journal of Marine Science and Engineering, 2020. **8**(5): p. 339.

[100] Li, Z., X. Jiang, H. Hopman, L. Zhu, and Z. Liu, *An investigation on the circumferential surface crack growth in steel pipes subjected to fatigue bending.* Theoretical and Applied Fracture Mechanics, 2020. **105**: p. 102403.

[101] Li, C.-Q. and S. Yang, *Stress intensity factors for high aspect ratio semi-elliptical internal surface cracks in pipes.* International Journal of Pressure Vessels and Piping, 2012. **96**: p. 13-23.

[102] Oh, C., T. Song, Y.-J. Kim, J. Kim, and T. Jin, *Approximate J estimates for axial part‐through surface‐cracked pipes.* Fatigue & Fracture of Engineering Materials & Structures, 2007. **30**(12): p. 1127-1139.

[103] Ligoria, S., G.S. Knight, and D. Ramachandra Murthy, *Three-dimensional finite element analysis of a semi-elliptical circumferential surface crack in a carbon steel pipe subjected to a bending moment.* The Journal of Strain Analysis for Engineering Design, 2005. **40**(6): p. 525-533.

[104] Branco, R., F. Antunes, and J. Costa, *A review on 3D-FE adaptive remeshing techniques for crack growth modelling.* Engineering Fracture Mechanics, 2015. **141**: p. 170-195.

[105] Dotta, F. and C. Ruggieri, *Structural integrity assessments of high pressure pipelines with axial flaws using a micromechanics model.* International journal of pressure vessels and piping, 2004. **81**(9): p. 761-770.

[106] Branco, C., A. Fernandes, and P. de Castro, *Fadiga de estruturas soldadas. ed.* Manuais Universitários, 1999.

[107] Suresh, S., *Fatigue of materials*. 1998: Cambridge university press.

[108] Bartaula, D., Y. Li, S. Koduru, and S. Adeeb. *Simulation of Fatigue Crack Growth Using XFEM*. in *Pressure Vessels and Piping Conference*. 2020. American Society of Mechanical Engineers.

[109] Smith, M., *Fitness for Service, API 579-1/ASME FFS-1*. 2007: API Publishing.

[110] Anderson, T.L., G. Thorwald, D.J. Revelle, D.A. Osage, J.L. Janelle, and M.E. Fuhry, *Development of Stress Intensity Factor Solutions for Surface and Embedded Cracks in API 579.* WRC Bulletin 2002. **471**.

[111] Coêlho, G.d.C., A.A. Silva, M.A. Santos, A.G. Lima, and N.C. Santos, *Stress intensity factor of semielliptical surface crack in internally pressurized hollow cylinder—a*

comparison between BS 7910 and API 579/ASME FFS-1 solutions. Materials, 2019. **12**(7): p. 1042.

[112] Raju, I. and J. Newman Jr, *Stress-intensity factors for internal and external surface cracks in cylindrical vessels.* Journal of Pressure Vessel Technology, 1982. **104**: p. 293-298.

[113] Manual, A.S.U.s., *Abaqus 6.11*. http://130.149, 2012. **89**(2080): p. v6.

[114] ASTM, I., *E399-90(1997) Standard Test Method for Plane-Strain Fracture Toughness of Metallic Materials*. 1997: West Conshohocken, PA.

[115] Tipple, C. and G. Thorwald. *Using the failure assessment diagram method with fatigue crack growth to determine leak-before-rupture*. in *2012 SIMULIA Community Conference, Providence, Rhode Island*. 2012.

[116] Arumugam, U., M. Gao, R. Krishnamurthy, and M. Zarea. *Full-Scale Fatigue Testing of Crack-in-Dent and Framework Development for Life Prediction*. in *International Pipeline Conference*. 2020. American Society of Mechanical Engineers.

[117] Keprate, A., R. Chandima Ratnayake, and S. Sankararaman, *Comparison of various surrogate models to predict stress intensity factor of a crack propagating in offshore piping.* Journal of Offshore Mechanics and Arctic Engineering, 2017. **139**(6).

[118] Bartaula, D., B. Ngandu, S.D. Koduru, Y. Li, and S. Adeeb, *Surrogate Modelling for the Estimation of Stress Intensity Factors*, in *17th Pipeline Technology Conference*. 2022 (To be published).

[119] Rasmussen, C.E. *Gaussian processes in machine learning*. in *Summer school on machine learning*. 2003. Springer.

[120] Pedregosa, F., G. Varoquaux, A. Gramfort, V. Michel, B. Thirion, O. Grisel, M. Blondel, P. Prettenhofer, R. Weiss, and V. Dubourg, *Scikit-learn: Machine learning in Python.* the Journal of machine Learning research, 2011. **12**: p. 2825-2830.

[121] VanRossum, G. and F.L. Drake, *The python language reference*. 2010: Python Software Foundation Amsterdam, Netherlands.

[122] Brownlee, J., *Train-Test Split for Evaluating Machine Learning Algorithms*, in *Machine Learning Mastery*, J. Brownlee, Editor. 2020.

[123] Doucet, A. and A.M. Johansen, *A tutorial on particle filtering and smoothing: Fifteen years later.* Handbook of nonlinear filtering, 2009. **12**(656-704): p. 3.

[124] Nordh, J., *pyParticleEst: A Python framework for particle-based estimation methods.* Journal of Statistical Software, 2017. **78**(1): p. 1-25.

[125] Labbe, R., *Kalman and bayesian filters in python.* Chap, 2014. **7**(246): p. 4.

[126] Kuhlman, D., *A python book: Beginning python, advanced python, and python exercises*. 2009: Dave Kuhlman Lutz.

ANNEX-A

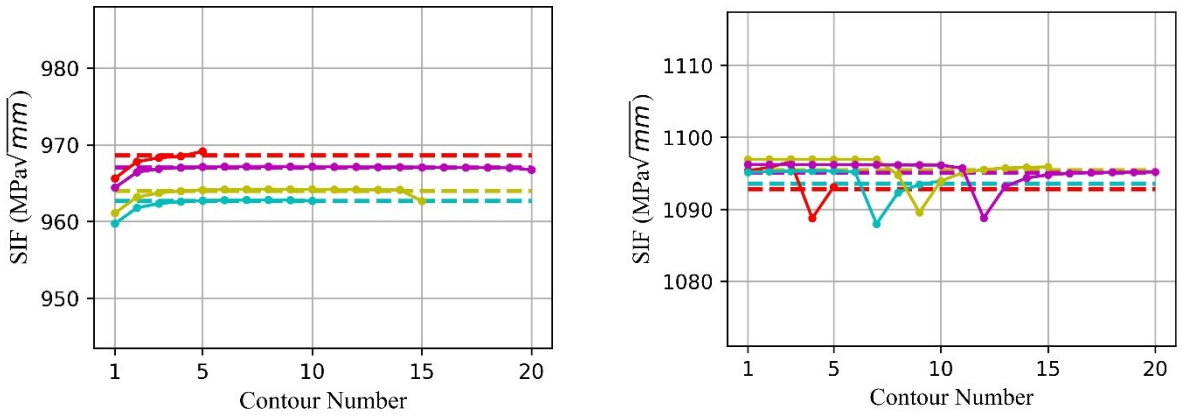

(a) (b)

Annex Figure A-1: Contour integral values around the crack tip in CT specimen (*a/W*= 0.229) (a) at the surface (b) at the mid thickness

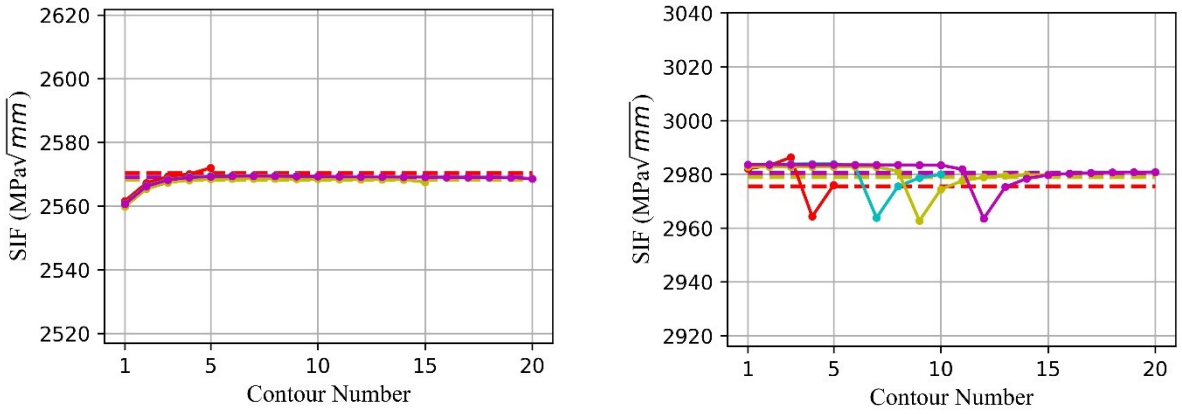

(a) (b)

Annex Figure A-2: Contour integral values around the crack tip in CT specimen (*a/W*= 0.6) (a) at the surface (b) at the mid thickness

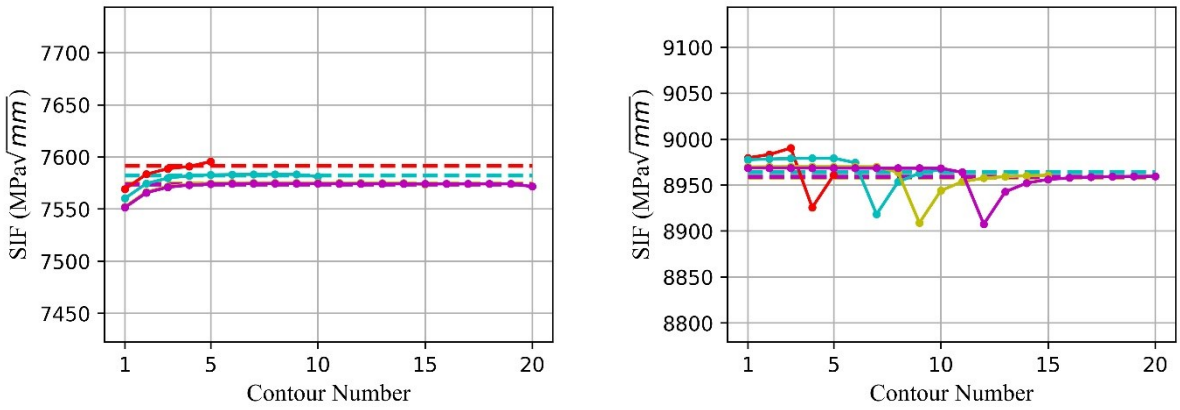

(a) (b)

Annex Figure A-3: Contour integral values around the crack tip in CT specimen (a/W= 0.8) (a) at the surface (b) at the mid thickness

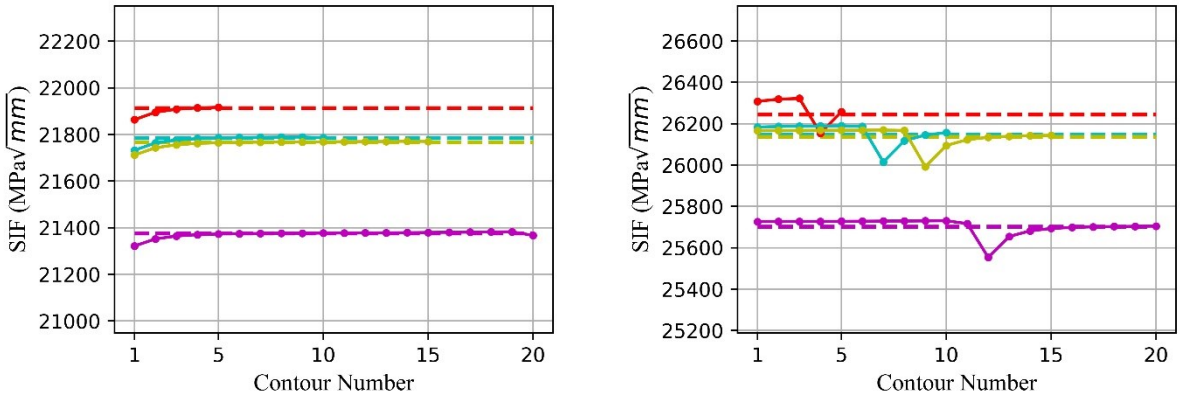

(a) (b)

Annex Figure A-4: Contour integral values around the crack tip in CT specimen (a/W= 0.9) (a) at the surface (b) at the mid thickness

Annex Table A-1 Coefficient of variation of SIF at surface and mid-thickness with number of contours

a/W	Coefficient of variation (CV) of SIF at surface (%)	Coefficient of variation (CV) of SIF at mid-thickness (%)
0.229	0.246	0.099
0.4	0.033	0.111
0.6	0.030	0.062
0.8	0.095	0.026
0.9	0.926	0.804
Average	**0.266**	**0.220**

Annex Table A-2 Coefficient of variation of SIF with mesh size

a/W	Coefficient of variation (CV) of SIF at surface (%)	Coefficient of variation (CV) of SIF at finite distance under the surface (%)	Coefficient of variation (CV) of SIF at mid-thickness (%)
0.229	4.434	2.063	0.241
0.400	4.607	2.165	0.240
0.600	4.761	2.261	0.234
0.800	5.296	2.582	0.304
0.900	5.874	2.776	0.367
Average	**4.994**	**2.369**	**0.277**

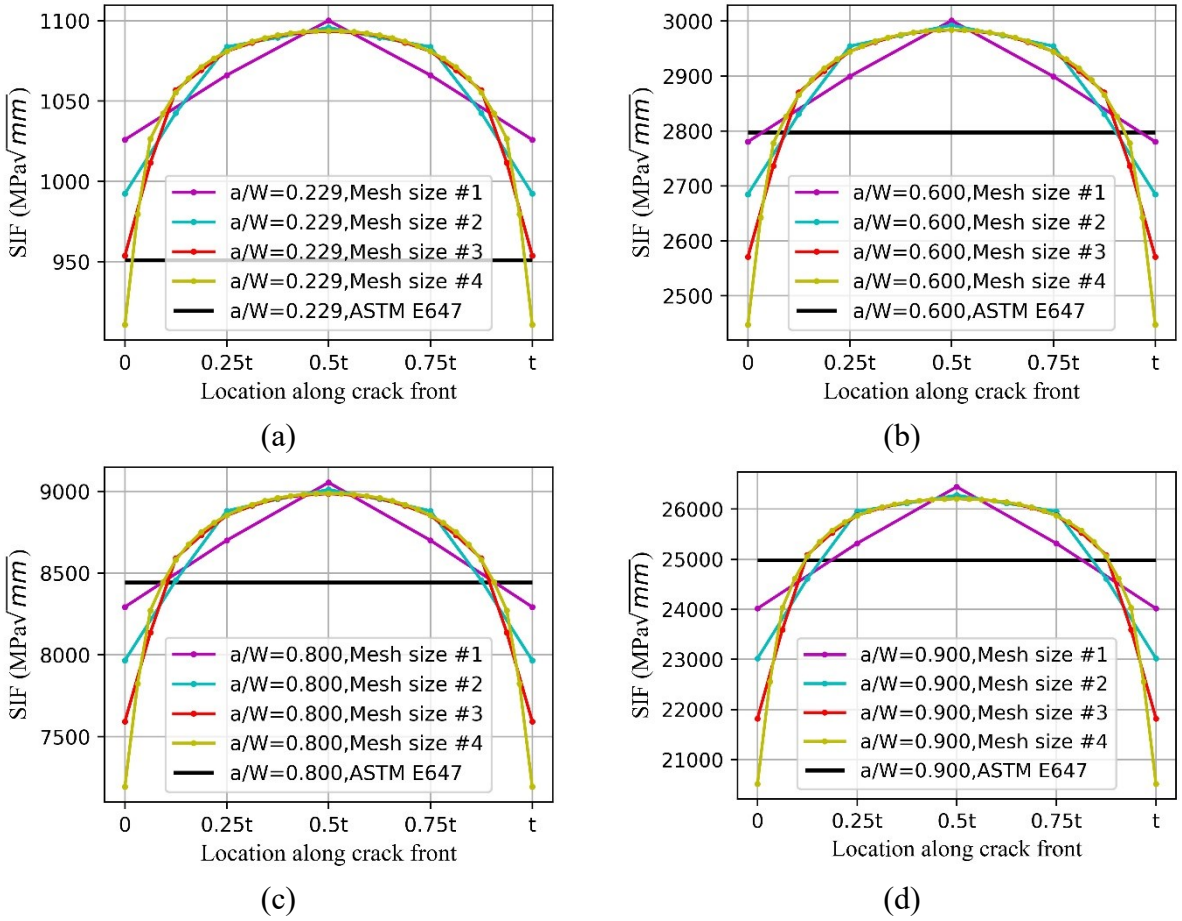

Annex Figure A-5: SIF values along thickness of the CT specimen for different values of a/W using conventional FEM with wedge elements (a) *a/W*=0.229, (b) *a/W*=0.6, (c) *a/W*=0.8, and (d) *a/W*=0.9

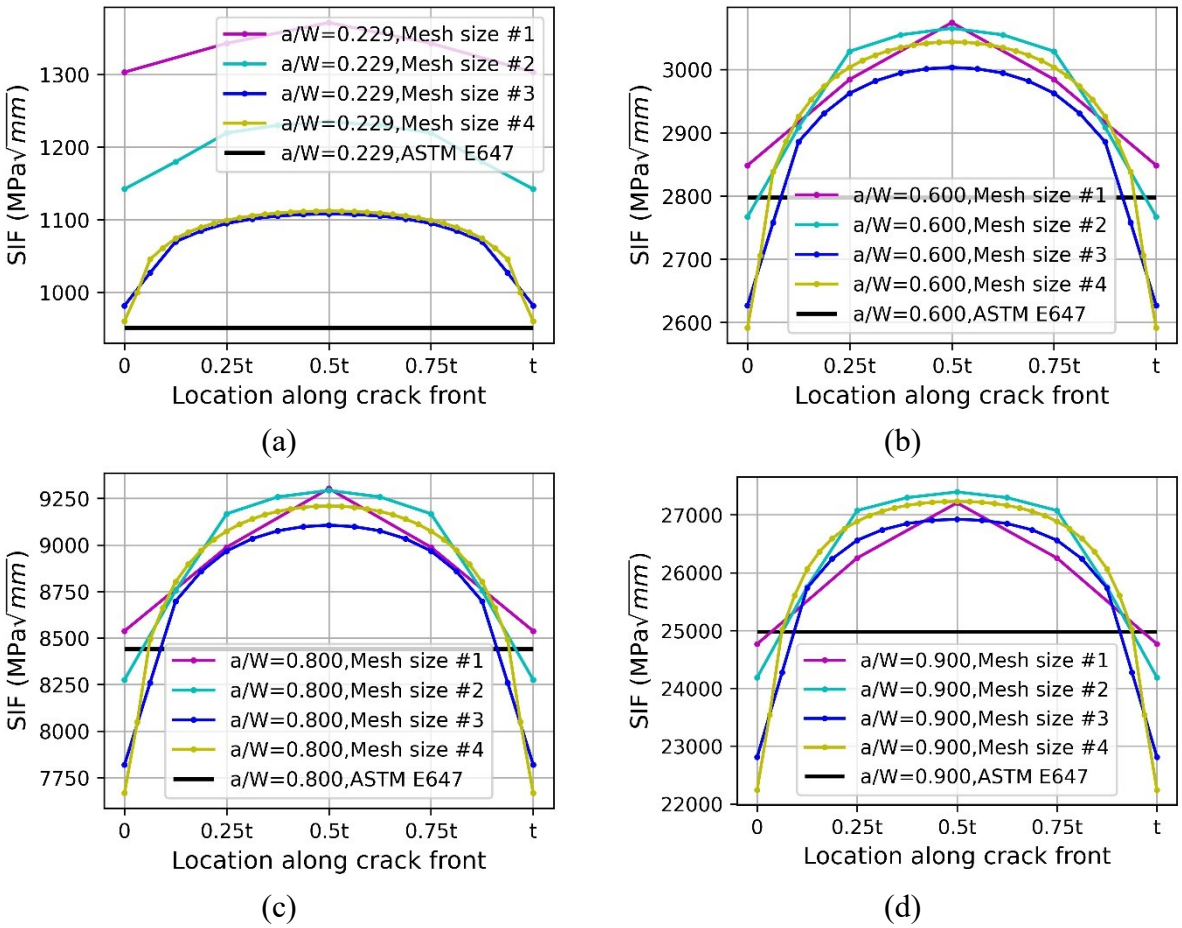

Annex Figure A-6: SIF values along thickness of the CT specimen for different values of *a/W* using XFEM for (a) *a/W*=0.229, (b) *a/W*=0.6, (c) *a/W*=0.8, and (d) *a/W*=0.9

Annex Table A-3 Comparison table against SIF values obtained using other meshing strategies to the focused mesh with wedge elements in CT specimen

a/W	XFEM- Hex			XFEM- Gen			FEM-Hex		
	Surface (%)	Finite element depth from surface (%)	Mid-thickness (%)	Surface (%)	Finite element depth from surface (%)	Mid-thickness (%)	Surface (%)	Finite element depth from surface (%)	Mid-thickness (%)
0.229	2.919	1.505	1.329	2.720	1.408	1.200	1.812	0.408	0.255
0.400	2.028	0.627	0.525	1.863	0.447	0.236	1.874	0.436	0.299
0.600	2.188	0.781	0.659	2.096	0.670	0.443	2.022	0.556	0.424
0.800	2.996	1.522	1.358	2.997	1.488	1.186	2.494	0.914	0.807
0.900	4.546	2.900	2.737	4.701	2.963	2.632	3.417	1.657	1.595
Average	**2.936**	**1.467**	**1.322**	**2.876**	**1.395**	**1.139**	**2.324**	**0.794**	**0.676**

Annex Table A-4 Coefficient of variation of SIF with mesh size for pipeline section

a/t	Coefficient of variation (CV) of SIF at surface (%)	Coefficient of variation (CV) of SIF at finite distance under the surface (%)	Coefficient of variation (CV) of SIF at depth (%)
0.263	0.413	1.235	0.561
0.579	1.015	0.616	0.315
0.832	1.910	0.710	0.288
0.868	2.054	0.831	0.191
0.904	2.041	0.892	0.350
0.911	1.961	0.956	0.331
Average	**1.566**	**0.873**	**0.339**

Annex Table A-5 Comparison table against SIF values obtained using other meshing strategies to the focused mesh with wedge elements in FEM models for pipeline section

a/t	XFEM			FEM-Hex		
	Surface (%)	Finite element depth from surface (%)	Depth (%)	Surface (%)	Finite element depth from surface (%)	Depth (%)
0.263	5.092	1.123	0.547	1.710	0.660	0.243
0.579	5.530	1.605	0.545	2.259	1.013	0.284
0.832	5.344	2.497	0.583	2.818	1.351	0.261
0.868	5.312	2.537	0.466	2.883	1.409	0.253
0.904	5.181	2.460	0.348	2.926	1.446	0.246
0.911	5.340	2.617	0.417	2.947	1.462	0.257
Average	**5.300**	**2.140**	**0.485**	**2.591**	**1.223**	**0.257**

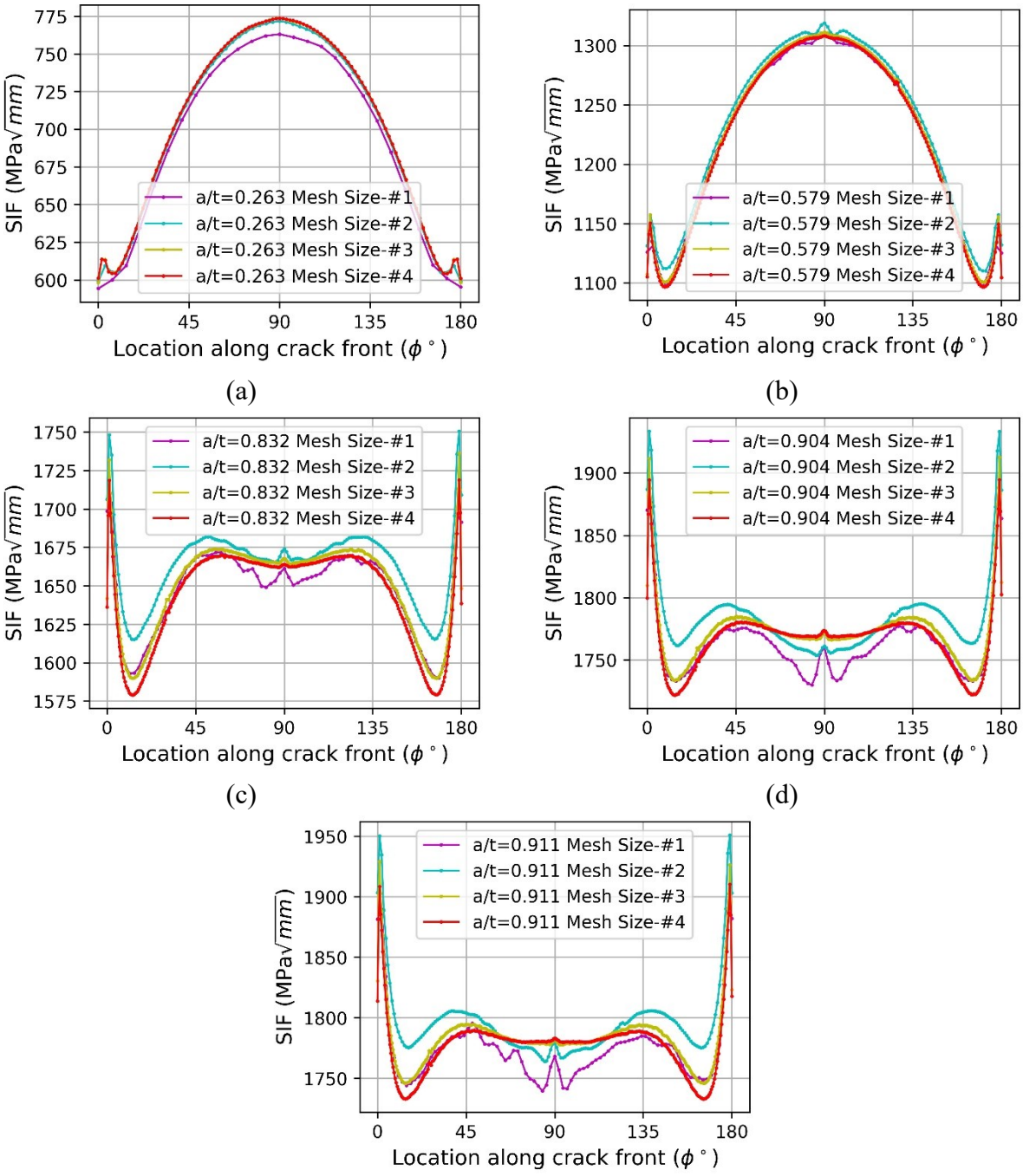

Annex Figure A-7: SIF values along crack front calculated using FEM with focused mesh having wedge elements for (a) *a/t*=0.263, (b) *a/t*= 0.579, (c) *a/t*=0.832, (d) *a/t*=0.904, and (e) *a/t*=0.911

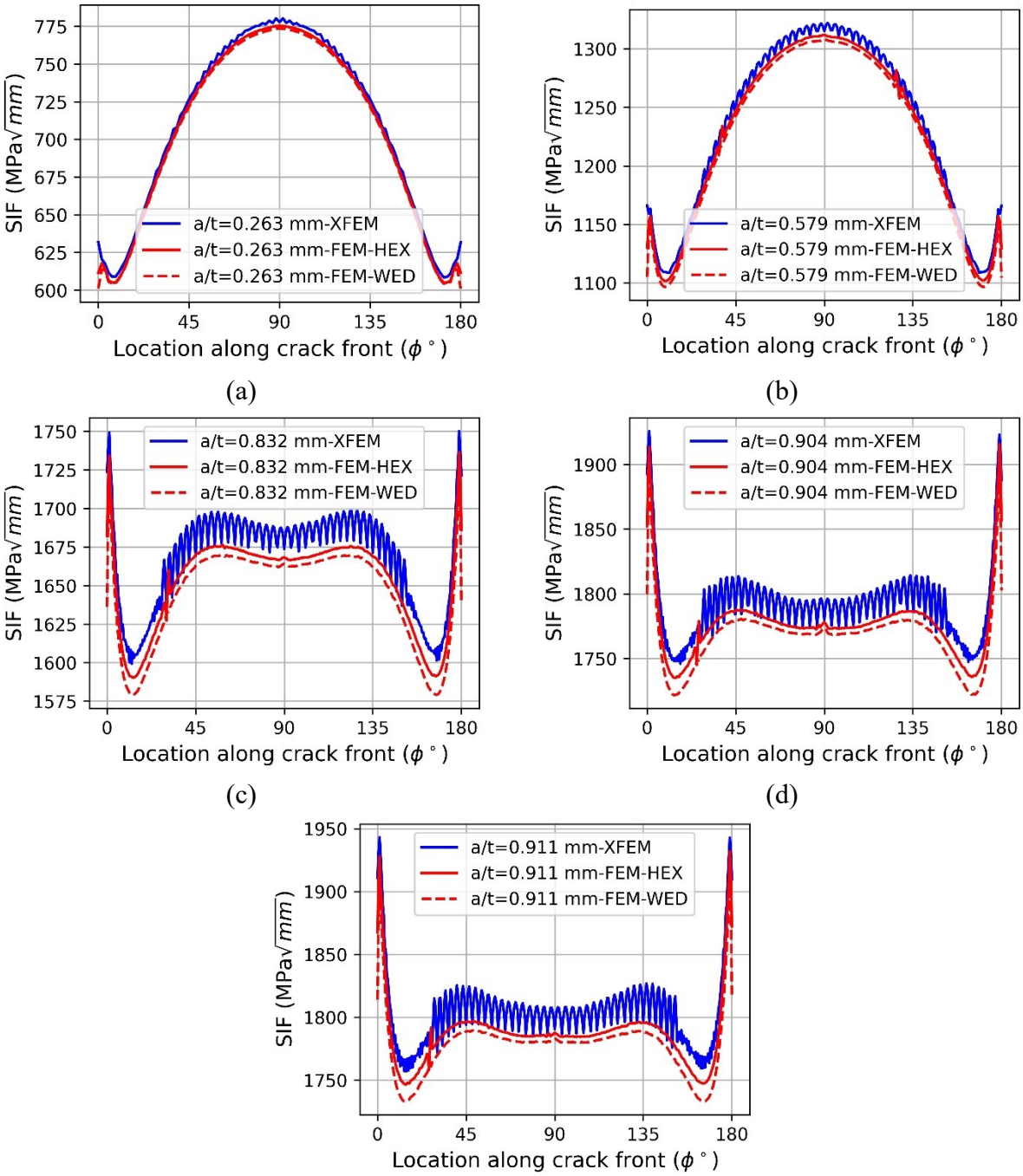

Annex Figure A-8: SIF values along crack front calculated using different meshing strategies in XFEM and FEM models for (a) *a/t*=0.263, (b) *a/t*= 0.579, (c) *a/t*=0.832, (d) *a/t*=0.904, and (e) *a/t*=0.911

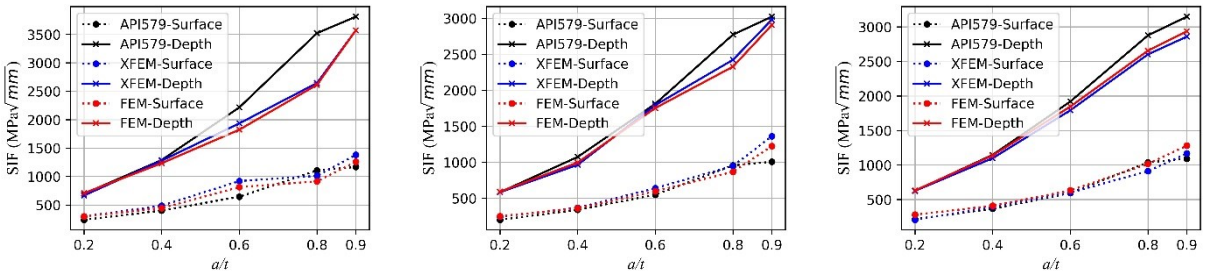

(a) (b) (c)

Annex Figure A-9: SIF values at finite depth from surface and depth ($\phi = 90^{\circ}$) for *a/c*=0.125 (a) Pipeline #1, (b) Pipeline #2, and (c) Pipeline #3

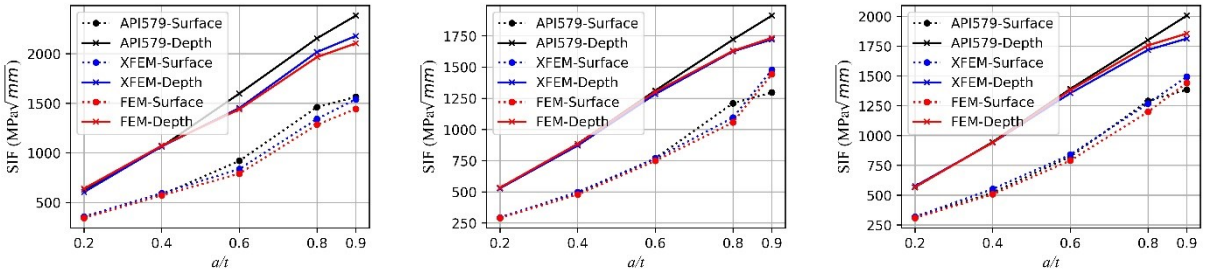

(a) (b) (c)

Annex Figure A-10: SIF values at finite depth from surface and depth ($\phi = 90^{\circ}$) for *a/c*=0.25 (a) Pipeline #1, (b) Pipeline #2, and (c) Pipeline #3

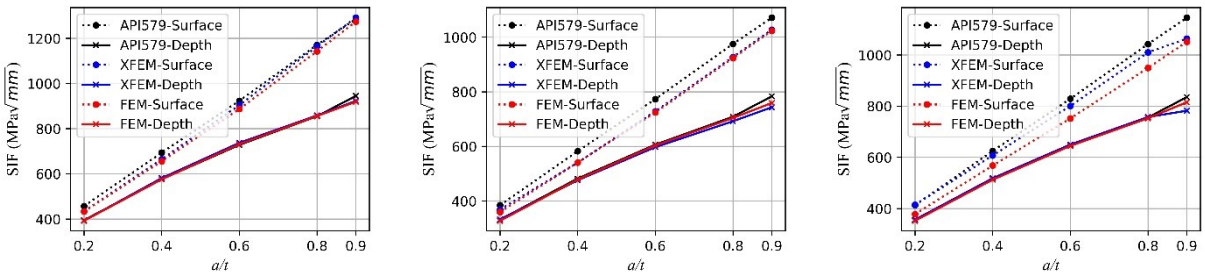

(a) (b) (c)

Annex Figure A-11: SIF values at finite depth from surface and depth ($\phi = 90^{\circ}$) for *a/c*=1 (a) Pipeline #1, (b) Pipeline #2, and (c) Pipeline #3

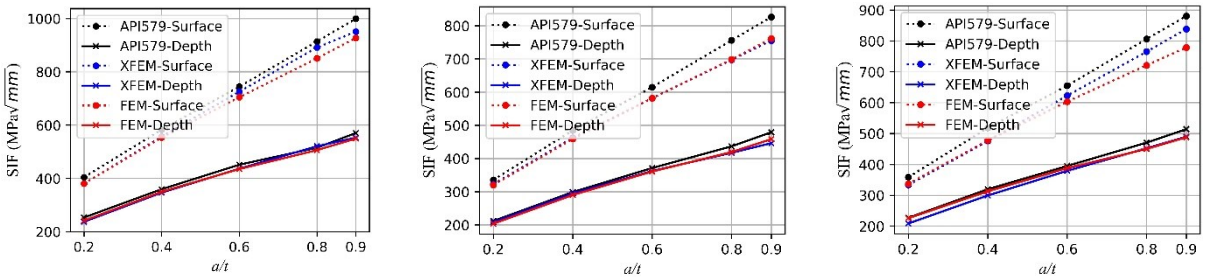

(a) (b) (c)

Annex Figure A-12: SIF values at finite depth from surface and depth ($\phi = 90^{\circ}$) for *a/c*=2 (a) Pipeline #1, (b) Pipeline #2, and (c) Pipeline #3

ANNEX-B

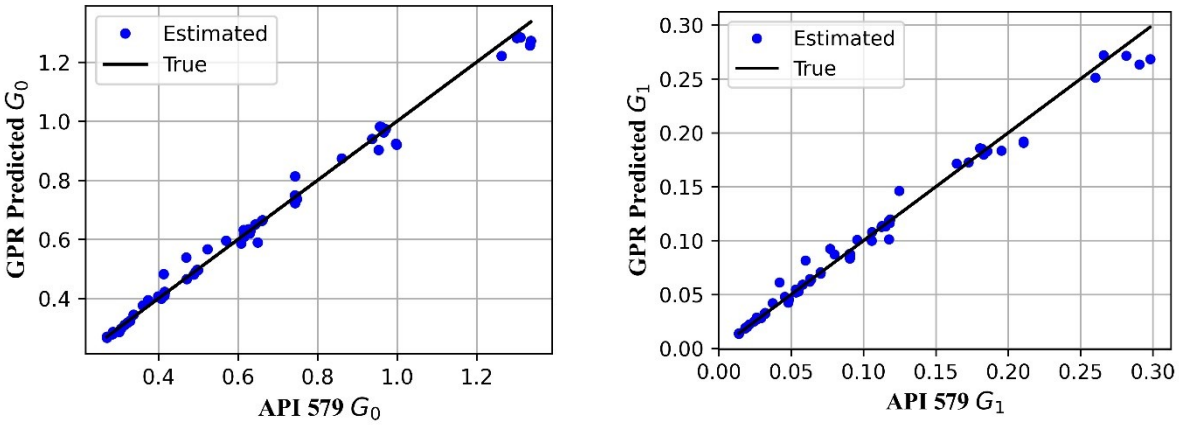

(a) (b)

Annex Figure B-1: Scatter plot for G_0 and G_1 estimated at tabulated points using API 579 model and developed GPR model at surface (a) G_0, and (b) G_1

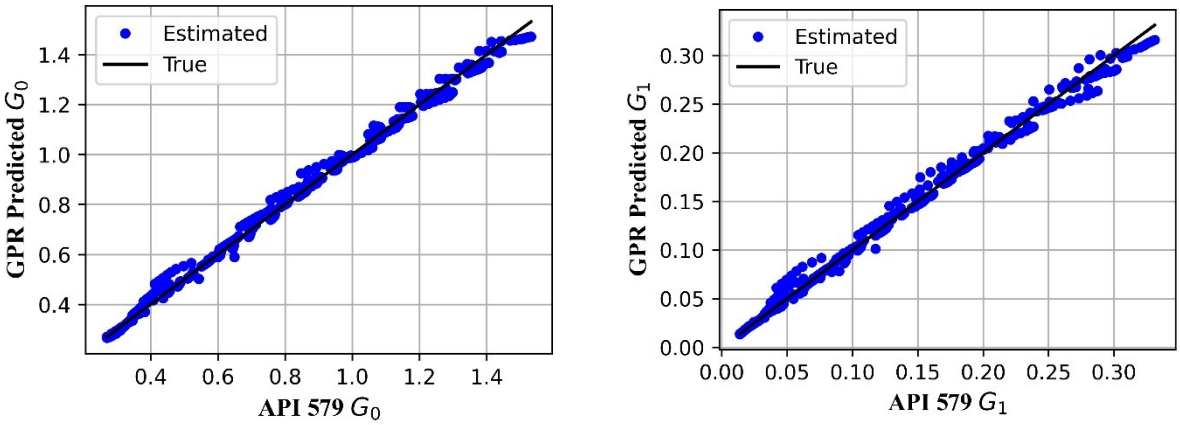

(a) (b)

Annex Figure B-2: Scatter plot for G_0 and G_1 estimated at intermediate points using API 579 model and developed GPR model at surface (a) G_0, and (b) G_1

ANNEX-C

The formulas used for calculation of influence coefficients and other parameters used in API 579 model are as follows:

$$G_0 = A_{0,0} + A_{1,0}\beta + A_{2,0}\beta^2 + A_{3,0}\beta^3 + A_{4,0}\beta^4 + A_{5,0}\beta^5 + A_{6,0}\beta^6$$

$$G_1 = A_{0,1} + A_{1,1}\beta + A_{2,1}\beta^2 + A_{3,1}\beta^3 + A_{4,1}\beta^4 + A_{5,1}\beta^5 + A_{6,1}\beta^6 \qquad \text{C-1}$$

$$\beta = \frac{2\phi}{\pi}$$

For points other than at the surface and deepest point i.e. $0 < \phi < \pi / 2$

$$G_{21} = 108 + 180z + 576z^2 - 864z^3 + (1056 + 128M_1)\delta z^{2.5}$$

$$G_{22} = M_3(45\eta + 54\eta z + 72\eta z^2 - 315\omega z^{2.5} + 144\eta z^3)$$

$$G_2 = \frac{\sqrt{Q}}{945\pi}(G_{21} + G_{22})$$

$$G_{31} = 880 + 1232z + 2112z^2 + 7040z^3 - 11264z^4 + (13056 + 1280M_1)\delta z^{3.5}$$

$$G_{32} = M_3(385\eta + 440\eta z + 528\eta z^2 + 704\eta z^3 - 3465\omega z^{3.5} + 1408\eta z^4) \qquad \text{C-2}$$

$$G_3 = \frac{\sqrt{Q}}{13860\pi}\left(G_{31} + G_{32}\right)$$

$$G_{41} = 1820 + 2340z + 3328z^2 + 5824z^3 + 19968z^4 - 33280z^5 + (37376 + 3072M_1)\delta z^{4.5}$$

$$G_{42} = M_3(819\eta + 909\eta z + 1040\eta z^2 + 1248\eta z^3 + 1664\eta z^4 - 9009\omega z^{4.5} + 3328\eta z^5)$$

$$G_4 = \frac{\sqrt{Q}}{45045\pi}\left(G_{41} + G_{42}\right)$$

$$Q = 1.0 + 1.464\left(\frac{a}{c}\right)^{1.65} \quad \text{for } a/c \le 1.0$$

$$Q = 1.0 + 1.464\left(\frac{c}{a}\right)^{1.65} \quad \text{for } a/c \ge 1.0 \qquad \text{C-3}$$

$$M_1 = \frac{-1050\pi G_1 + 105\pi G_0(3+7z) - 4\sqrt{Q}(35 - 70z + 35z^2 + 189\delta z^{0.5} + 61\delta z^{1.5})}{\sqrt{Q}(168+152z)z^{0.5}\delta}$$

$$M_2 = \frac{1}{3}(M_1 - 3)$$

$$M_3 = \frac{2(-105\pi G_1 + 45\pi G_0 z + \sqrt{Q}(28 + 24z - 52z^2 + 44\delta z^{1.5}))}{\sqrt{Q}(-21 + 2z + 19z^2)\eta}$$

$$M_4 = \frac{(1+M_3\eta)z}{z-1} \qquad \text{C-4}$$

$$z = \sin\phi$$

$$\delta = \sqrt{1+z}$$

$$\omega = \sqrt{1-z}$$

$$\eta = \sqrt{\frac{1}{z} - 1}$$

For deepest point $(\phi = \pi/2)$

$$G_2 = \frac{\sqrt{2Q}}{\pi}\left(\frac{16}{15} + \frac{1}{3}M_1 + \frac{16}{105}M_2 + \frac{1}{12}M_3\right)$$

$$G_3 = \frac{\sqrt{2Q}}{\pi}\left(\frac{32}{35} + \frac{1}{4}M_1 + \frac{32}{315}M_2 + \frac{1}{20}M_3\right)$$

$$G_4 = \frac{\sqrt{2Q}}{\pi}\left(\frac{256}{315} + \frac{1}{5}M_1 + \frac{256}{3465}M_2 + \frac{1}{30}M_3\right)$$

C-5

$$M_1 = \frac{2\pi}{\sqrt{2Q}}\left(3G_1 - G_0\right) - \frac{24}{5}$$

$$M_2 = 3$$

$$M_3 = \frac{6\pi}{\sqrt{2Q}}\left(G_0 - 2G_1\right) + \frac{8}{5}$$

For surface point $(\phi = 0)$

$$G_2 = \frac{\sqrt{Q}}{\pi}\left(\frac{4}{5} + \frac{2}{3}N_1 + \frac{4}{7}N_2 + \frac{1}{2}N_3\right)$$

$$G_3 = \frac{\sqrt{Q}}{\pi}\left(\frac{4}{7} + \frac{1}{2}N_1 + \frac{4}{9}N_2 + \frac{2}{5}N_3\right)$$

$$G_4 = \frac{\sqrt{Q}}{\pi}\left(\frac{4}{9} + \frac{2}{5}N_1 + \frac{4}{11}N_2 + \frac{1}{3}N_3\right)$$

C-6

$$N_1 = \frac{3\pi}{\sqrt{Q}}\left(2G_0 - 5G_1\right) - 8$$

$$N_2 = \frac{15\pi}{\sqrt{Q}}\left(3G_1 - G_0\right) + 15$$

$$N_3 = \frac{3\pi}{\sqrt{Q}}\left(3G_0 - 10G_1\right) - 8$$

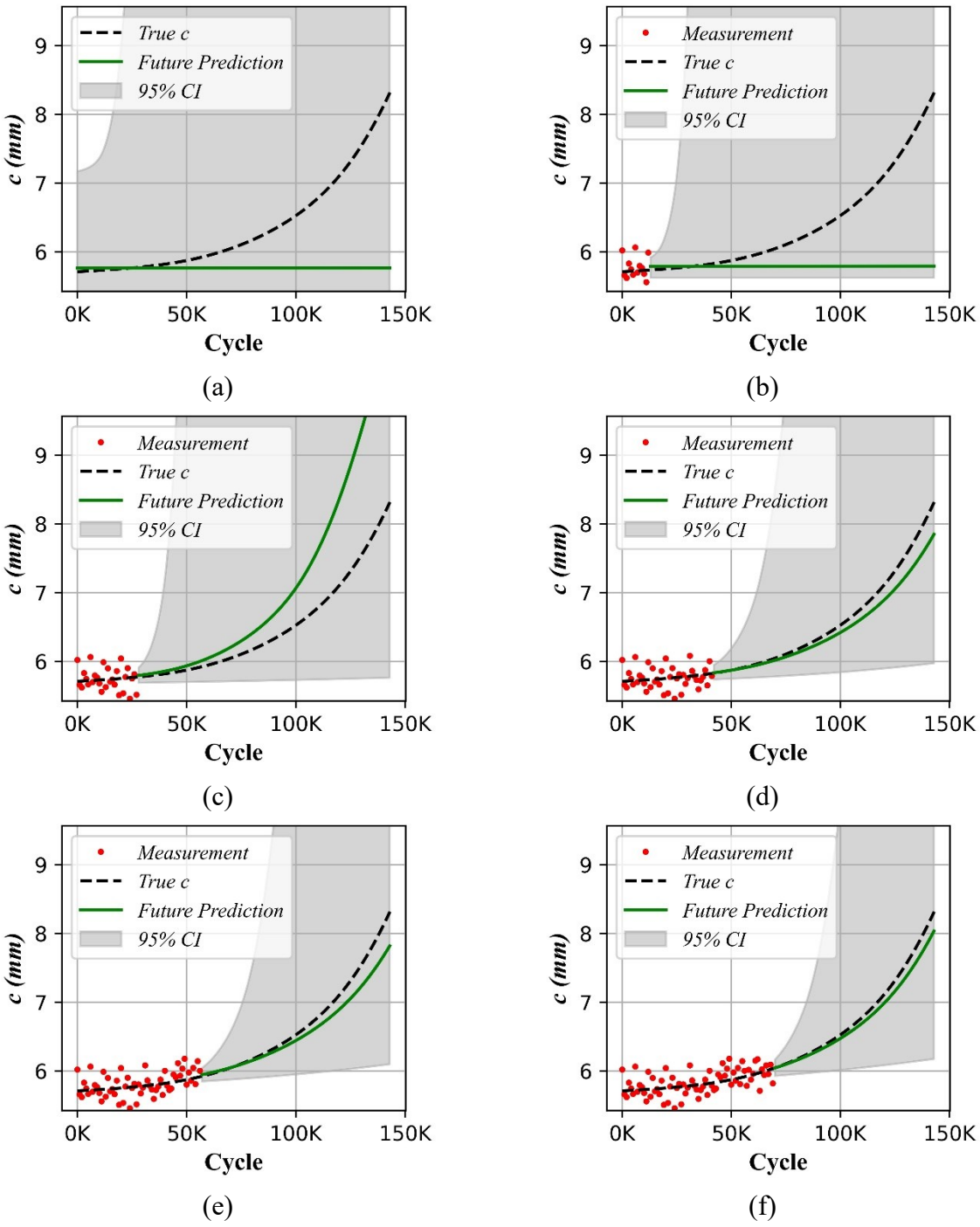

Annex Figure C-1: Future half crack length '*c*' prediction for noise level=0.15 mm when (a) No measurement data (with no observations), (b) Measurement data up to 14000 cycles (with 15 observations), (c) Measurement data up to 29000 cycles (with 30 observations), (d) Measurement data up to 43000 cycles (with 44 observations), (e) Measurement data up to 58000 cycles (with 59 observations), and (f) Measurement data up to 71000 cycles (with 72 observations)

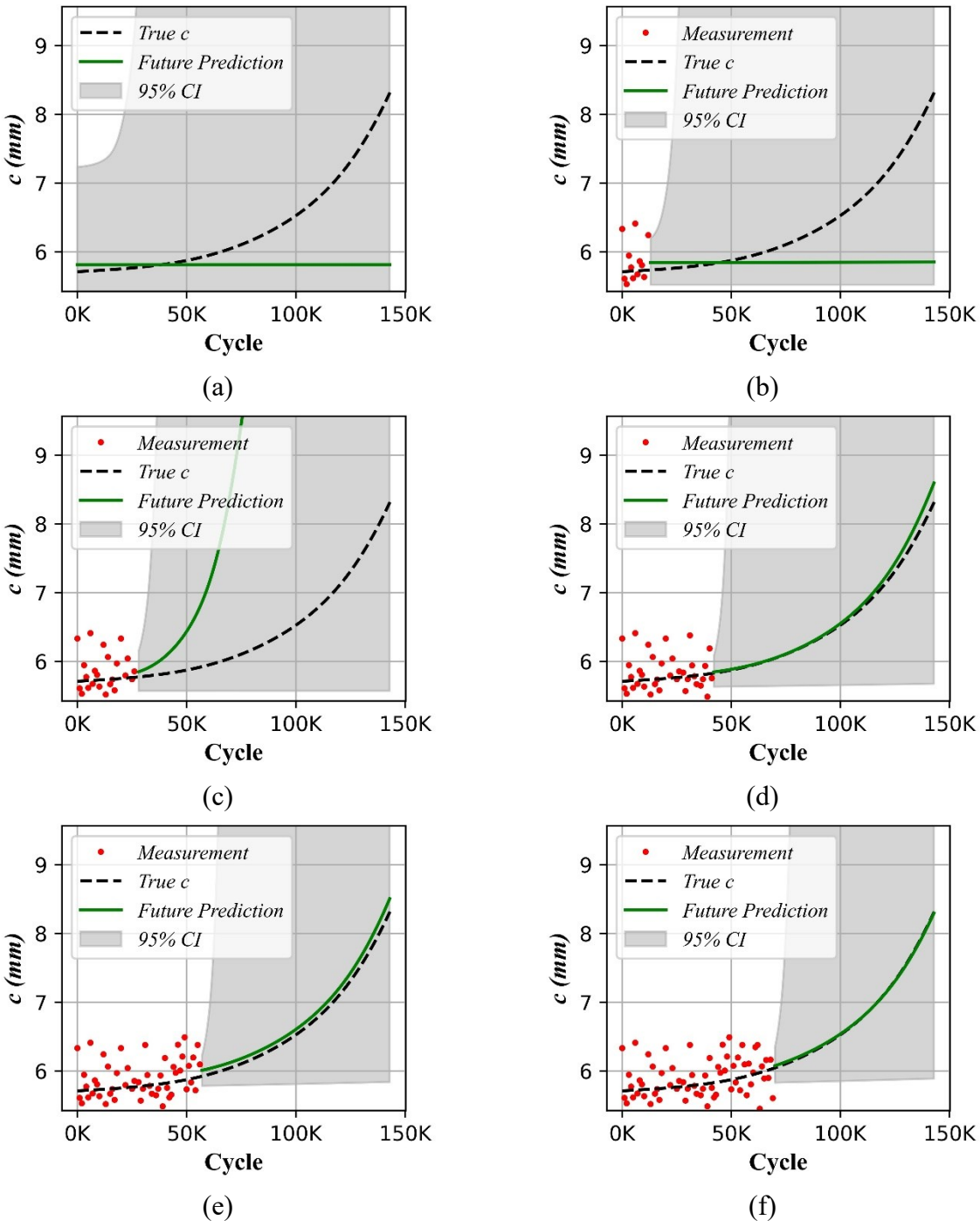

Annex Figure C-2: Future half crack length '*c*' prediction for noise level=0.3 mm when (a) No measurement data (with no observations), (b) Measurement data up to 14000 cycles (with 15 observations), (c) Measurement data up to 29000 cycles (with 30 observations), (d) Measurement data up to 43000 cycles (with 44 observations), (e) Measurement data up to 58000 cycles (with 59 observations), and (f) Measurement data up to 71000 cycles (with 72 observations)